Computational Characterization of Radiation-induced Defect Dynamics and Material Response

by

Miaomiao Jin

B.S., Nuclear Engineering
University of Science and Technology of China, 2013

SUBMITTED TO THE
DEPARTMENT OF NUCLEAR SCIENCE AND ENGINEERING

IN PARTIAL FULFILLMENT OF THE REQUIREMENTS FOR THE DEGREE OF
DOCTOR OF PHILOSOPHY IN NUCLEAR SCIENCE AND ENGINEERING

AT THE
MASSACHUSETTS INSTITUTE OF TECHNOLOGY
JUNE 2019

Signature of Author: _____

Miaomiao Jin
Department of Nuclear Science and Engineering
May 20, 2019

Certified by: _____

Michael Short, Ph.D.
Class '42 Career Development Assistant Professor of Nuclear Science and Engineering
Thesis Supervisor

Certified by: _____

Ju Li, Ph.D.
Battelle Energy Alliance Professor of Nuclear Science and Engineering
Professor of Materials Science and Engineering
Thesis Reader

Accepted by: _____

Ju Li, Ph.D.
Battelle Energy Alliance Professor of Nuclear Science and Engineering
Professor of Materials Science and Engineering
Chair, Department Committee on Graduate Theses

Computational characterization of radiation-induced defect dynamics and material response

by

Miaomiao Jin

Abstract

Material degradation due to radiation damage poses serious concern on the reliability and durability of any reactor design. To understand material performance under the extreme environments combining high temperature and intense irradiation, the response of radiation damage must be meticulously analyzed, both experimentally and computationally. These efforts will not only bridge the knowledge gap in the fundamental understanding of physical processes, but also allow for prediction of material behavior under a variety of conditions and development of novel materials with superior radiation tolerance.

This thesis investigates multiple aspects of radiation damage in materials using various computational methods over a wide range of time and length scale, including atomistic description of defect dynamics, multiscale simulations of radiation processes, and artificial intelligence prediction of material responses based on experimental studies. Firstly, to resolve the fundamental mechanisms of radiation-induced behavior, the traditional molecular dynamics simulations on single-atom damage cascade is extended by developing an algorithm to appropriately introduce numerous consecutive cascades; hence, an experimental dose level on the order of dpa (displacement per atom) can be achieved to enable realistic understanding of observed material responses. It has been utilized to examine the radiation behaviors in solid-solution alloys and nanocrystalline metals such as defect dynamics and grain boundary migration. Secondly, to break the intrinsic limitation of scale in atomistic simulations, a multiscale microstructural evolution framework that links binary-collision approximation, molecular dynamics and cluster dynamics is built to describe mesoscale experimental observations. It is used to successfully explain the non-power-law defect distribution in irradiated tungsten. This tool can be generalized to study the spatial dependent defect evolution in materials under ion irradiation. Finally, to bypass the physics-based complexity of describing materials evolution in real applications, a holistic view enabled by machine learning techniques is utlized, and applied to predict the onset of void swelling in metals with a manually collection of data from experimental studies. The model has generated satisfying results for prediction of unseen data based on

material properties and experimental parameters.

Thesis Supervisor: Michael P. Short
Title: Associate Professor

Acknowledgments

I would like to express my earnest thanks to a number of people throughout the thesis process.

I hold deep and sincere thanks to my advisor, Prof. Michael Short, for his very generous guidance, strong support and tremendous patience during the research. Not only have I been genuinely influenced by the enthusiam, perseverance, and optimism, I have also learnt the philosophy of a better research life in the future. This thesis would not have been greatly improved without his comments, but surely any errors that remain are my own.

I want to acknolwledge all the individuals in the MIT MNM group for their indispensible roles in both my research and life, especially Dr. Penghui Cao, a keen mentor whom I will never thank more than enough. My gratitude extends to Prof. Ju Li and Prof. Sidney Yip, whom I always look up to and who inspire me to embark on a fulfilling research journey.

I would also like to thank my friends including Weiyue Zhou, Yang Yang, Yifeng Che, and my fellow classmates, with whom I have had so many wonderful experiences, and whose friendship I will value for life.

Finally, my family, especially Jilang Miao, have embraced me with endless support through my emotional ups and downs. I owe them more than I would be able to experess.

Contents

List of Figures

15

22

List of Tables

Chapter 1

Introduction

Material problems in nuclear systems must be successfully resolved for nuclear energy to make further improvement on safety and economics. The current and proposed concepts on future fission and fusion reactors (Figure 1-1) present an exceptionally harsh operating environment for structural materials due to a combination of high temperature, high stress, chemically aggressively coolant and intense irradiation [1]. Structural materials are expected to maintain mechanical, dimensional and microstructural integrity during the long service time under these extreme conditions. Therefore, many alloys that are currently used in nuclear energy systems will not satisfy the requirements, calling for the development of mechanically reliable and highly radiation-tolerant materials.

Multiple promising material designs have been proposed to improve radiation resistance and also bear superior mechanical properties, including nanoscale oxide dispersed steels [3], high entropy alloys [4], nano-layered materials [5], and interfacial engineering [6]. A good description of radiation response of materials is the prerequisite to both qualify the novel options and optimize existing designs.

Although tens of years of radiation study have provided numerous experimental results on different materials, ranging from simple metals to complicated alloys, these results can be hard to explain and generalize and sometimes contradictory. Even with the availability of more advanced techniques facilitating clearer observations on multi-angles of material behavior, information regarding the fundamental processes

Generation IV: Nuclear Energy Systems Deployable no later than 2030 and offering significant advances in sustainability, safety and reliability, and economics
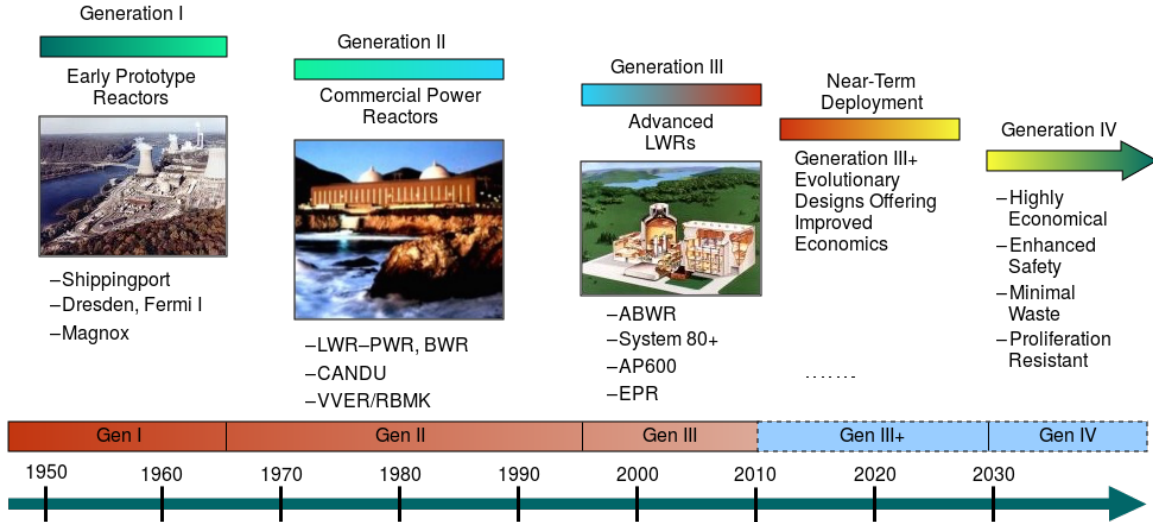
Figure 1-1: Generations of reactor design [2].

and the underlying mechanisms is still hardly obtainable. For a variable-rich system including radiation environment and complexity of materials such as various constituent elements, internal structures and manufacturing specifications, it is hard to identify active factors for any unexplained behavior, given limited time-consuming experiments.

However, computational study of the physical processes backed by a appropriate theoretical framework and the exponential growth of computation capability can effectively provide an avenue to describe and predict material behavior. Simulation techniques like Monte Carlo, molecular dynamics, and continuum equations are especially useful to characterize physical processes and reveal new interpretations, such as high temporal and spatial resolution of microstructural evolution which experiments are hard to deliver. Therefore, this thesis work is characterizing radiation-induced material response with the appropriate computation tools, focusing on various aspects such as long-term microstructure evolution, defects structures, and defect-grain boundary interaction, phenomenological prediction of radiation effects. Radiation damage is inherently multiscale process, and the capability to describe it on a wide range of length and time scales is key to understanding material behavior; hence, these

studies are organized into three themes, from atomistic mechanisms with molecular dynamics, to integrated response in a multiscale computation framework, to physics-agnostic data prediction using machine learning:

- Atomistic understanding: mechanisms of damage resistance in single-phase concentrated solid solution alloys (Ni-Fe) and nanocrystalline metals (Cu); mechanistic understanding of radiation-enhanced grain growth; assessment of grain stabilization via amorphous intergranular film.

- Multiscale description: multiscale study of radiation-induced defect evolution with spatial dependence in pure tungsten and iron.

- Data-driven prediction: predicting the onset of void welling in metals via machine learning.

The goal is not only to provide mechanistic understanding, but also facilitate the prediction of material behavior, which will ultimately contribute to efficient screening and qualification of candidate materials for nuclear energy to make further improvement on safety and economics.

1.1 Thesis layout

Chapter 1 serves as an introduction of the whole structure, where motivations and highlights of current work are emphasized.

Chapter 2 starts with an overview of radiation damage and effects, analyzed via both experiments and simulations. On the experimental side, previous experiments in studying material degradation under neutron irradiation and the strong argument in using ion irradiation as surrogate to expedite experiment time span are concisely reviewed. Computationally, the inherent multiscale property necessitates multiple simulation techniques over different ranges of time and spatial regimes. In the end, some trending radiation-tolerant material designs are introduced.

Building on top of current computation techniques, the following chapters focus on resolving various issues arising from the material-dependent characteristics.

27

Firstly, material behavior is examined with atomistic simulations. Chapter 3.1 and 3.2 focus on the understanding of radiation resistance shown in high entropy alloys and nanocrystalline materials, respectively. Following the study of nanocrystal, the inevitable problem is irradiation-enhanced grain growth. Chapter 3.3 elaborates the grain boundary migration and grain growth due to irradiation in nanocrystalline Cu. Then Chapter 3.4 characterize the technique and the effect of grain stabilization via grain boundary complexion in Zr doped nanocrystalline Cu. Secondly, scaling up to multiscale framework is necessary considering the limitation of both time and length scales in atomistic simulations. To tackle this problem, the cluster dynamics model has been built using a finite element solver in conjunction with atomistic methods to describe the long-term defect evolution. As an application, Chapter 4.1 demonstrates this methodology and tries to understand the deviation from power law of defect size distribution in irradiated pure tungsten at cryogenic temperature. Finally, as the complexity of real materials systems can become intractable with physics-based models, a shortcut via modern machine learning methods may be possible to circumvent the conundrum. Chapter 5 as proof-of-concept is a demonstration of promising results using this technique to predict the onset of void swelling based on manually collected experimental data.

Chapter 6 provides an overview of the studies encompassed in this thesis, the major contributions, and current trending problems. Although different materials are considered, the findings and methodology can be generalized in understanding radiation damage in other materials. The atomistic details of microstructural evolution, along with coarse-grained continuum modeling compose a relatively complete big picture, making possible both macro-scale blueprint and high-resolution touches. However, more work still needs to done considering the emergence of new radiation-resistant designs and the incentive to understand radiation effect in other applications such as semi-conductors.

Chapter 2

Background

This chapter briefly reviews radiation damage process, the effects on materials, and the study techniques including experimental tools and simulation methods. It ends with an overview of current understanding of radiation resistance in new materials.

2.1 Radiation damage

Structural materials in reactors are subject to harsh environments involving a combination of high temperature, high stress, chemically aggressive coolant, and intense radiation fluxes. In contrast to other energy industries, this additional radiation field accelerates microstructure evolution and material degradation, such as embrittlement and dimension instability. The problem becomes more pronounced with increasing irradiation dose, hence limits the economy and safety of long-serviced reactors. Therefore, to accommodate the imminent need of reactor lifetime extension and implementation of advanced reactor systems, the performance of materials in extreme environment must be improved. Significant progress has been made to better understand radiation effects. Figure 2-1 demonstrates some examples: (a) segregation, (b) increase in yield strength, (c) swelling and (d) irradiation-assisted stress corrosion cracking. To describe these long term behaviors, it is necessary to characterize the microstructural evolution with experiments and modeling. Such evolution is a result of collective dynamics of defects and internal structures (interfaces, dislocations,

and precipitates). Correspondingly, the capability to effectively remove defects and control structural integrity is crucial to improve radiation resistance.
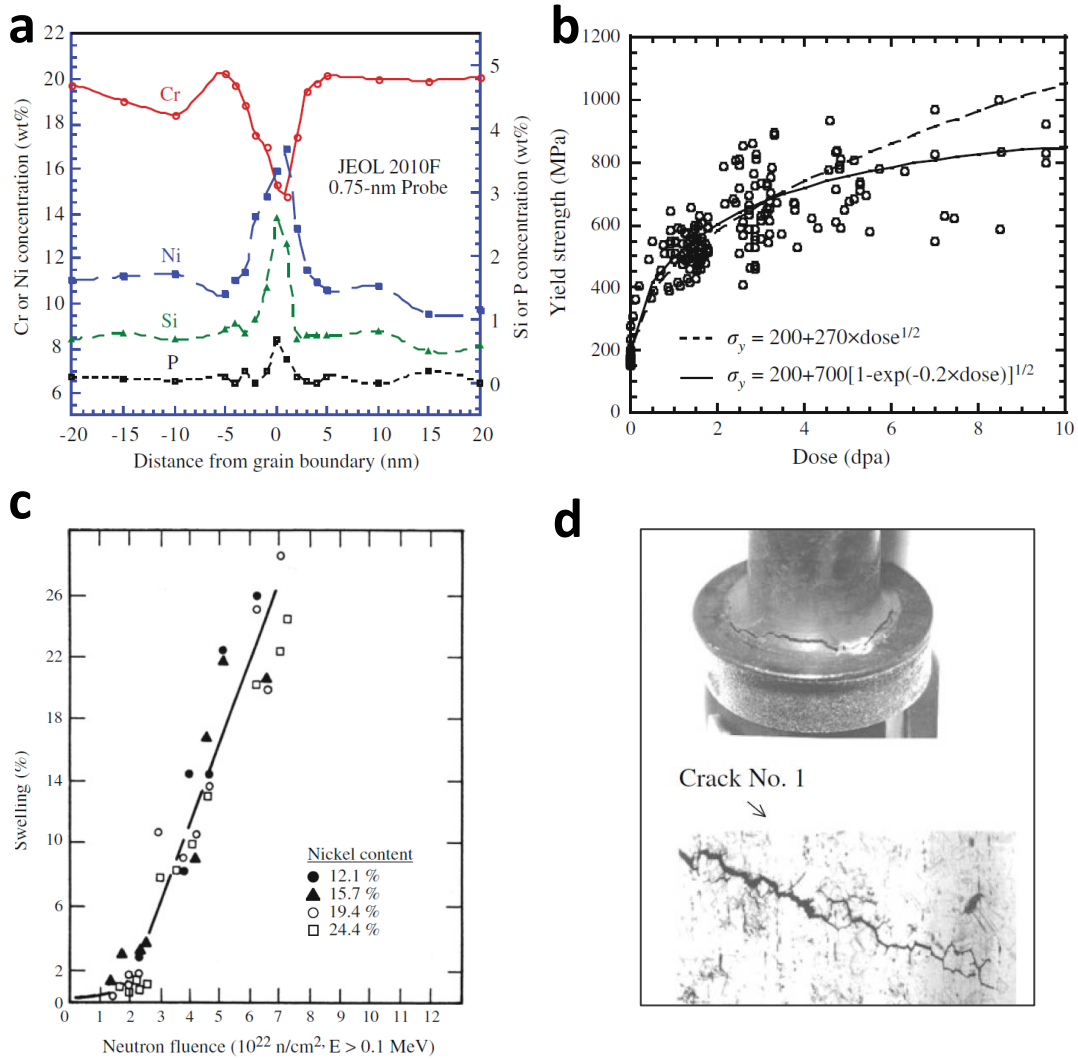
Figure 2-1: Radiation effects [1]: (a) Radiation-induced segregation of Cr, Ni, Si, and P at the grain boundary of a 300 series stainless steel irradiated in a light water reactor core to several dpa at 300 °C; (b) Effect of irradiation dose on measured tensile yield strength for several 300 series stainless steels irradiated and tested at a temperature of about 300 °C; (c) Swelling of Fe-15Cr-xNi ternary alloys in EBR-II at temperatures between 400 and 510 °C for nickel levels between 12.1 and 24.4 wt%; (d) Irradiation-assisted stress corrosion cracking: cracks in cold-worked 316 stainless steel baffle bolt. The location of the cracks received a neutron dose of about 7 dpa at ~ 310 °C.

Zooming in on the radiation damage process, it starts from the collisions between energetic incident particles and lattice atoms. Part of the energy is transferred as

the kinetic energy of the target atoms which are referred as primary knock-on atom (PKA). The PKA can then be displaced out of its lattice position and continue colliding with other atoms. A damage cascade may be generated given higher enough incident energy. Finally, as the PKA energy has dropped to an amount smaller than the displacement threshold, it rests in the lattice. An approximate timescale for the process which constitutes the initial $10^{-11}s$ is shown in Table 2.1 [1]. During the time span, particles loses energy in several ways during transport, by collision, electron excitation, ionization, or Bremsstrahlung. The energy loss can be described in two main forms: nuclear (S_n) and electronic (S_e) stopping power. In the high energy regime, S_e dominates and atoms are less likely to be displaced from their lattice sites. In the low energy regime, $S_n > S_e$, where deposition of energy which leads to displacement of target atoms becomes dominant.

Table 2.1: Approximate timescales in the primary stage of radiation damage.

Time (s)	Event	Result
10^{-18}	Collision between incident particle and target atom: energy transfer	Creation of a PKA
10^{-13}	Displacement of lattice atoms by the PKA	Damage cascade
10^{-11}	Energy dissipation and lattice recrystallization	Defects and clusters

Corresponding to Table 2.1, the primary stage can be roughly divided into three steps: ballistic stage, thermal spikes, and quenching. During the first phase, atoms undergo high-energy binary collision and many atoms are displaced from their original lattice sites. However, these temporary defects are not stable. During the following thermal spike, the kinetic energy of PKAs is shared with surrounding atoms, which induce local melting. As energy is dissipated, the molten zone quenches back down to thermal equilibrium within a few pico-seconds. At the end of this stage, defects are left behind, in the form of defect clusters or isolated point defects including vacancies and interstitials. The number of residual defects is, however, much lower than that from the ballistic stage. Displacement efficiency, defined as the ratio of between the residual defects from quenching the cascade and the estimated "ballistically" produced

defect, is introduced to quantify the damage, although argument still remains on whether this concept is a good measure considering the microstructural evolution induced by produced defects with different characteristics. It should be noted that damage cascades are closely related to the type and energy of incident particles. Well-separated subcascades may be formed with high energy incident particles. Meanwhile, the morphology of residual defects vary significantly with the particle types. Light ions such as electrons, protons and helium tend to produce isolated Frenkel pairs while heavy ions and neutrons create large defect clusters. Figure 2-2 [1] illustrates the differences by considering 1 MeV incident particles to target nickel. The reason is that the energy transfer cross-sections of heavy ion or neutron are usually much larger than those of light ions, so that the former can more efficiently transfer kinetic energy to target atoms, which then generate a cascade of displaced atoms rather than isolated defects.
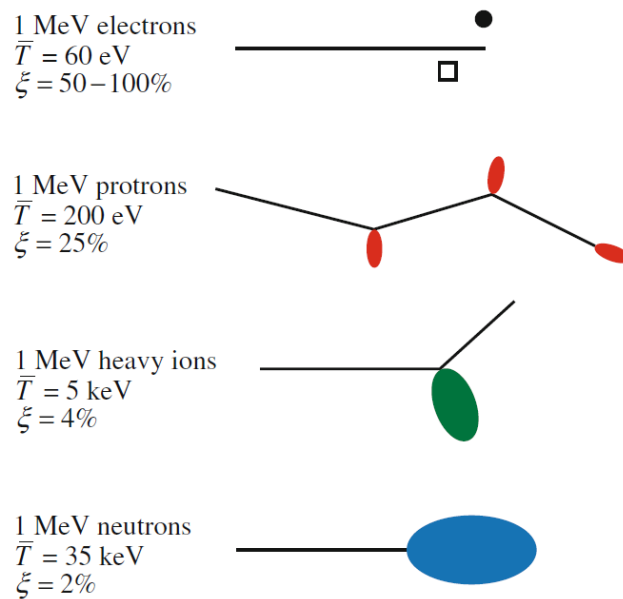
Figure 2-2: Difference in damage morphology, displacement efficiency, and average recoil energy for 1 MeV particles of different types incident on nickel [1].

Radiation damage is inherently multi-scale process as depicted by Figure 2-3 [7]. Beyond initial cascade stage ($\sim 10^{-11}s$) as described in Table 2.1, the annealing of residual damage involves defect migration and interaction, through thermally activated diffusion of mobile defects species. The long timescale evolution of defects over
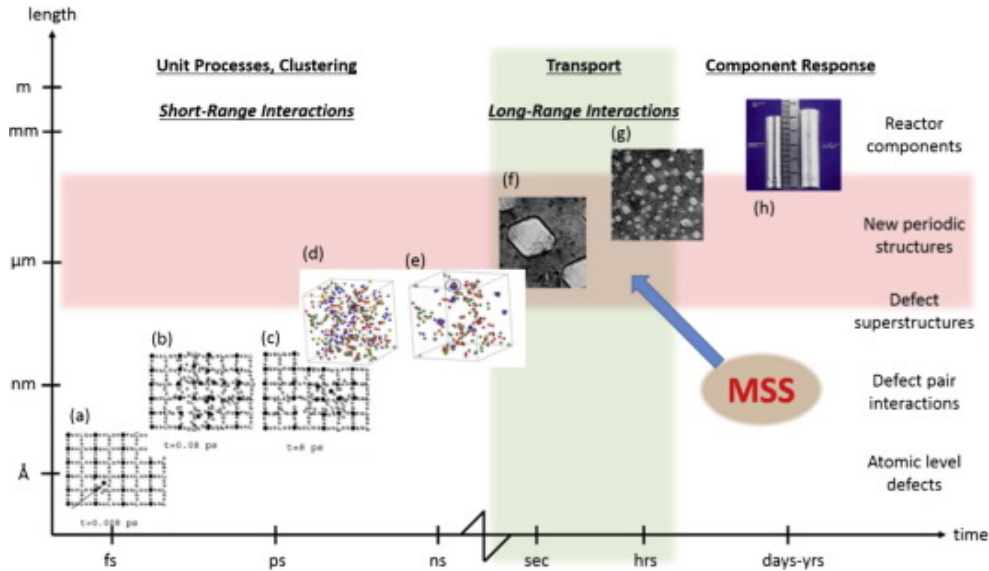
Figure 2-3: Spatial-temporal scales of processes involved in void swelling. In (a)-(e), radiation knocks host atoms out of their lattice points, causing local melting, followed by annealing where most atoms return to lattice sites. With longer time for vacancies to migrate and accumulate, (f)-(g) show the observed material response in the form of void swelling [7]. MSS denotes mesoscale science which bridges micro- and macro-response.

periods of seconds to decades induces microstructural evolution [8], causing material property changes such as void swelling, hardening, and embrittlement [9]. Thus long timescale studies are important to quantify real damage to irradiated materials. Currently, radiation damage continues to be quantified using displacements per atom (dpa) [1], which only describes the initial, ballistic stage of radiation damage. One dpa means that on average all atoms have been displaced from their lattice points once. It was initially introduced to reconcile differences in observed radiation damage from reactors or irradiations with different energy spectra [10], and made great strides in discovering similarities between formerly disparate experiments. The Norgett-Robinson-Torrens (NRT) model [11] which modifies the basic Kinchin-Pease model is commonly used to estimate the number of displacements,

$$\nu(T) = \frac{\kappa E_D}{2 E_d} \tag{2.1}$$

where E_D is the damage energy available to displace atoms, by subtracting the energy

33

lost in electron excitation from the total energy of the PKA, κ is a factor around 0.8 accounting for the two-body potential approximation, and E_d is the threshold displacement energy. While the NRT model provides a quick estimation of the number of displacements, it does not describe the process within the cascade, the configuration of defects, or the fraction of defects that survives the ballistic stage. Since the actual surviving defects from damage cascades and the spatial correlation will affect the evolution of microstructure, dpa itself is an inadequate measure in comparing the level of radiation damage. Woo and Singh later conceptualized a production bias model to treat the scenario of damage cascade where intracascade recombination, clustering, and thermal dissociation of clusters become non-negligible [12]. It was found that the bias has a controlling effect on the void swelling rate. It signifies the need of proper theories to characterize radiation-induced microstructure evolution.

2.2 Brief review of previous work

Radiation effects such as void swelling that alters physical and mechanical properties of nuclear components have been a drive force in understanding the mechanisms. Since the mid-last century, a number of sophisticated radiation experiments have been done: materials ranging from highly purified metal to industrial alloys, bombardment with a variety of particles, very low temperature environment, in-situ observations, and recolonization of recovery stages with careful annealing. As aforementioned, radiation damage is multiscale in nature, the evolving of defects especially during the short time scale in the collisional phase can not be resolved experimentally, which calls for simulation techniques that cover time scale from feto-second to years in order to efficiently examine microstructural evolution. Thanks to the increasing capability of computation power, the development of radiation simulation techniques is much expedited. Section 2.2.1 and 2.2.2 give brief reviews of experiment effort and simulation achievement, and provide references for detailed studies on specific phenomena such as voids near grain boundaries, decoration of edge dislocations by SIA loops, self-organized void lattice, etc., for interested readers.

2.2.1 Experiments and theories

A comprehensive coverage of the physical effects of radiation damage is given by Was [1], such as dimensional evolution and mechanical degradation. In this book, the author specifically talks about the following phenomena with ample directly related experimental studies as manifest of long-time microstructural evolution: element segregation, void swelling, growth, hardening, embrittlement, and irradiation-assisted stress corrosion cracking. Overall, the damage accumulation that gives rise to dimension changes and segregation has been treated in terms of chemical rate theory. The assumption behind the theory include homogeneous production of point defects, which can be justified under conditions such as electron irradiation. However, conventional rate theory becomes inadequate where damage morphologies vary significantly and material parameters change dramatically in space.

Although it may appear that the rest of research is patchwork attempts to previous framework, in fact, inconsistencies and confounding interpretations always arise, such as the relation between spatial correlation of cascades and swelling rate, the effect of impurities in affecting defect migration barrier, and the role of injected interstitials using charged particles. With more advanced and high resolution characterization techniques, new phenomena and explanations are revealed and in the meantime, some old understandings are open to scrutiny because of factors like dpa calculation, instability of neutron source, and migration dimensionality of mobile defects.

Unfortunately, lengthy experiments are often infeasible to conduct in realistic conditions, owing to the worldwide scarcity of simulated neutron sources and low dose rates. Therefore, heavy/light ion irradiations and simulations are often used to emulate the effect of neutrons in order to speed the irradiation process with a much lower cost. Since the resultant PKA spectrum vary significantly from that of neutron irradiation, and neutron spectra in different reactors and even at different locations within the reactor are not the same and much less controllable than ion irradiation, the emulation is still a recognized technique to test material response. However, the residual radiation damage in the form of various microstructural defects,

ultimately of interest in experiments and material property evolution predictions, is significantly affected by the types of incoming particles [13], the temperature [14], and the dose rate [15]. Meanwhile, some unique effects of ion irradiation are revealed such as surface sputtering, mixing, and chemical change in the target. Generally, ion can penetrate much less in depth and introduce strong spatial variation along the trace in contrast with neutron irradiation. A cross-sectional sample may become a confounding factor for experimental observations. Hence, it still remains controversial in drawing equivalence with a proper measure of radiation effects between charged particle and neutron irradiation.

Up to now, a number of characterization techniques have been used. On the microstructural level, TEM (transmission electron microscopy), SEM (scanning electron microscopy), scattering imaging techniques (eg. neutron, x-ray) are commonly used. At the atomic scale, APT (atom probe tomography) offering extensive capabilities for both 3D imaging and chemical composition measurements is becoming favorable. Specifically, microstructure characterization has benefit significantly from sophisticated TEM imaging. The resolution can be down to $\sim nm$ on the thin foils of samples. With settings such as bright field, dark field and microdiffraction, one can identify and then quantify the defects like dislocation loops and cavities (see Figure 2-4 for demonstration). A depth dependent image may suggest the void swelling after transformation of the raw cavity counts [16]. These quantities are valuable in assessing simulation results and perform parametrization of the models.

2.2.2 Simulations

Commonly employed simulation approaches to describe radiation damage process are adapted to the dominant physical processes over different scales. Figure 2-5 sketches the commonly applied methods in different regimes. They include the binary collision approximation (BCA) of the initial stage of radiation damage, molecular dynamics (MD) simulations of damage cascades, kinetic Monte Carlo (KMC) and rate theory (RT) for long term evolution, etc. It is these microstructures at extremely long times, ranging from seconds to years, which are of interest to experimentalists and reactor
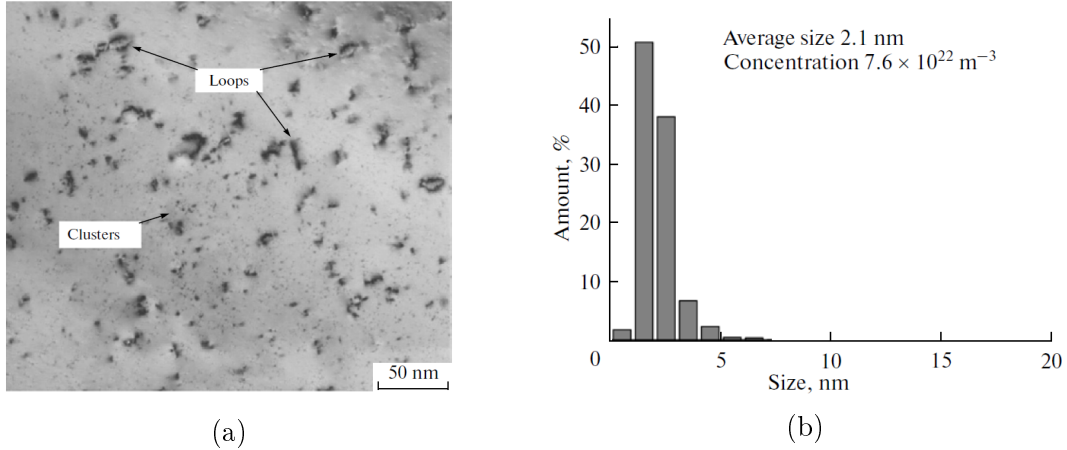
Figure 2-4: TEM imaging [17]: (a) Vacancy clusters and dislocation loops in Ni (neutron irradiated at 305 K to 0.15 dpa); (b) Histogram of the vacancy cluster count corresponding to (a).

designers. A full picture of the multiscale evolution of radiation damage, culminating in the accurate prediction and understanding of long timescale phenomena, should consider material-specific properties, irradiation conditions and then utilize proper approaches to reach experimental scales without sacrificing important information. The following paragraphs give brief introduction of the common techniques.

The initial production of defects can be obtained from BCA Monte Carlo simulations. The NRT and Kinchin-Pease model can be used to save computational cost by calculating defect production in terms of dpa with simplified equations [11]. A well-used software package is called SRIM, standing for the Stopping and Range of Ions in Matter [18]. This Monte Carlo simulation code can compute a number of results relevant to ion implantation. A 1D profile of damage level in dpa along the depth can be conveniently acquired by setting basic parameters such as displacement energy and composition. Recently, Stoller et al. [19] pointed out that the inconsistencies between SRIM calculation and more detailed atomistic simulations of damage cascades, and proposed several recommendations such as using "Quick" Kinchin-Pease option. While the dpa cannot determine the defect populations produced by radiation damage, the resulting PKA spectrum is useful in follow-on simulations of damage cascades, which allows for the precise description of the production of defect clusters.

MD has been extensively used in this regard to generate a comprehensive database
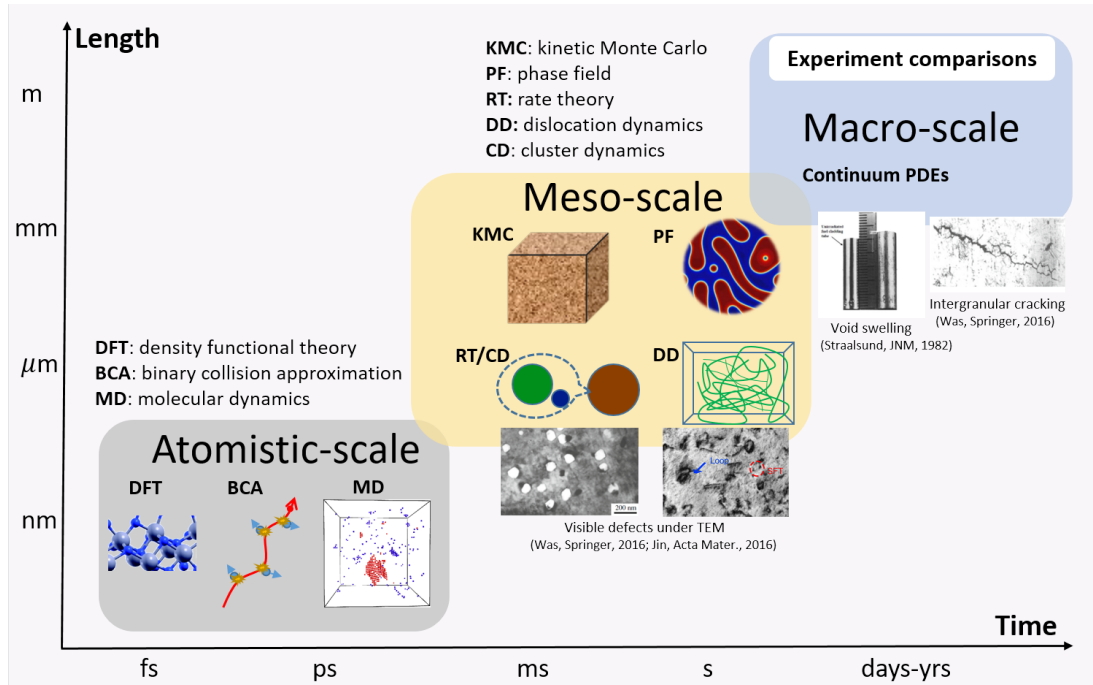
Figure 2-5: Typical methods for scale-dependent processes ranging from atomistic study on defects to continuum modeling of macro-scale experimentally measurable effects.

of surviving defects in simulation model resulting from various PKA energies [20]. It was found that interstitial and vacancy cluster production on MD (nanosecond) timescales varies significantly with temperature, cascade energy and interatomic potential. By examining the detailed damaging process across multiple time steps, one may extract interesting mechanisms related to defect migration and interaction. For example, Bai et al. [21] found that grain boundaries have a "loading-unloading" effect, i.e. interstitials are loaded into the boundary upon irradiation and then get emitted into the bulk to annihilate vacancies. It should be noted that the time and length scales of MD simulations are usually on the order of nanoseconds and tens of nanometers respectively, though some more advanced techniques have been developed to extend to much longer time scale. Considering the limitation of these accelerated MD in simulating cascades, an accurate simulation of further annealing of residual damage from multiple cascades calls for larger scale methods.

KMC fits into the frame, by describing system evolution process with discrete

38

events of object creation and destruction based on the rate constants,

$$\frac{dP_i}{dt} = \sum_j -k_{i \to j} P_i + k_{j \to i} P_j \qquad (2.2)$$

where P_i and P_j denote different states, and $k_{i \to j}$ and $k_{j \to i}$ are transition coefficients. An event is selected randomly according to its occurrence probabilities. It can explicitly handle the temporal and spatial fluctuations in defects production. The probabilistic nature of cascade initiation, nucleation and growth are intrinsically considered. In addition, the anisotropic mobility of defects can be very easily implemented. There are several variants of KMC, including: (1)AKMC, accounting for atomic jump details with potential; (2) LKMC, latticed based KMC; (3) OKMC, or object-KMC. Among these, OKMC is a very practical method to evolve the system in a relatively easy way. It can be applied to model the microstructural evolution of materials from the atomic to the mesoscopic scales [22–24]. It relies on pre-existing knowledge of all important interaction mechanisms of modeled entities, defect stability, and migration properties [25]. OKMC simulations sometimes suffer from serious inefficiency due to the enormous catalog of events and dominant low-barrier events. In addition, the number of simulated entities should be large enough to guarantee statistical quality of the results.

Rate theory approach based on chemical reaction kinetics can simulate meso- and macroscale time and length evolution of microstructures due to radiation damage. Ignoring the stochastic nature of the system, rate theory based on diffusion and reaction (master equation, ME) is a mesoscopic description of kinetics with rate coefficients from transition state theory. At microscopic level, the time evolution of a system can be characterized by molecular dynamics and Monte Carlo simulations. The tracking of particle positions can become computationally prohibitive, and thus the application of MEs gains popularity in recent years. It implicitly assumes 1) the system evolves deterministically, i.e. the volume is large enough such that the atomistic fluctuation can be safely ignored; 2) the system the well-mixed via diffusion or constant stirring [26]. A specific realization of MEs in the study of evolution of radiation-induced

defects in materials is referred to as cluster dynamics (CD). Although classical rate theory assumes the concentration of species is homogeneous (mean-field rate theory, MFRT), the spatially dependent factors such as the production of defects, inhomogeneous microstructure, and surface effects, necessitates an appropriate treatment of spatial dependence in MEs. Typical examples are heavy ion implantations and thin film experiments, where the production bias needs to be considered [12]. Then neutron and electron irradiation may be simplified as a degenerate scenario with a homogeneous model. Similar to OKMC, it also requires the parameterization of interaction coefficients. CD modeling of radiation damage has made many recent advances with. Multiple species have been modeled simultaneously, such as triple beam (H, He, and Fe) irradiation of ferritic alloys [27]. CD modeling of anisotropic materials, such as zirconium, has matched experimental predictions of growth [28]. Stoller et al. have proposed the conditions under which KMC and rate theory calculations overlap well [29]. More recently Jourdan et al. compared the effectiveness of different CD models and cluster size grouping methods [30]. Major advances have also been made in directly linking CD with experiments, such as direct observation of defect production and migration under in situ ion irradiation [31], and parameterizing cluster dynamics simulations directly with experimental TEM observations [32].

2.3 Radiation resistant materials

Although dose is commonly used to quantify radiation damage level, the effectiveness is compromised because certain materials can effectively recover from the initial ballistic collisional damage which means the real residual damage in materials due to radiation is not necessarily correlate with the dose level. In fact, the key to radiation resistance is the recovery of damage, so that serious radiation effects in reactor systems such as void swelling, segregation and precipitation can be postponed or avoided. Considerable efforts have been devoted to this subject, and they follow the general rule of enhancing defect annihilation, such as increasing defect sink density and tuning defect diffusion mode to boost recombination. There are four main categories as

summarized below.

2.3.1 Compositional and structural tailoring

Traditional austenitic stainless steels of type 316 and 304 experience series void swelling in reactors. It is then found that cold work and certain solute additions, particularly Ti, Si and P can extend the incubation period. The reason can be the formation of fine precipitates such as TiC carbides, FeTiP phosphides and $\gamma' - (Ni_3(Si, Ti))$, which act as efficient traps for helium atoms and defer void growth rate [33,34]. Along with microstructure tailoring, Ferritic-martensitic (FM) steels based on 9-12%Cr composition exhibit exceptional low swelling response, but the reduced high temperature strength restricts the use to certain low stressed components. As another example, Figure 2-6 compares several alloys in terms of the swelling response. It can be seen that ferritic alloys generally outperform austenitic alloys. Such difference may be explained by the solute-mediated defect annihilation and the dislocation stress field (Cottrell atmosphere) for defect absorption in the BCC structure, hence defects are reduced to limit void nucleation rate.
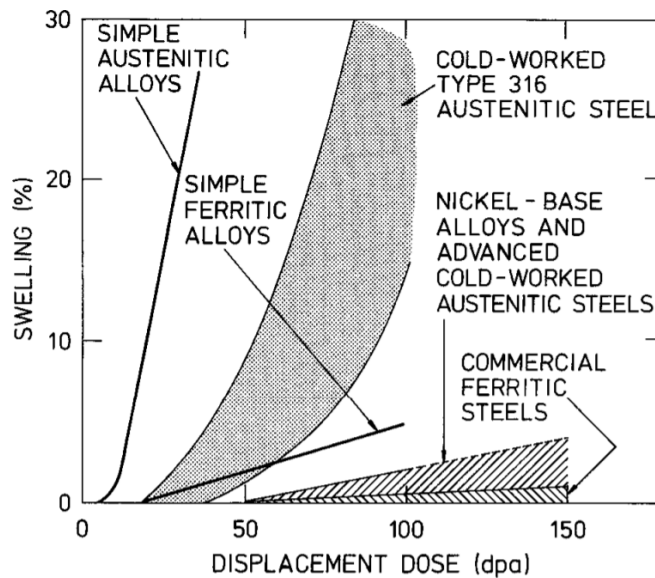
Figure 2-6: Comparison of swelling response in various austenitic and ferritic alloys as a function of dose [34]. It can be seen that ferritic structure outperforms austenitic.

41

2.3.2 Dispersion

Dispersoids in steel matrix can effectively tune materials performance. For example, oxide dispersion strengthened (ODS) steels have been seen as a promising structural material in future nuclear systems due to their superior radiation resistance, high-temperature creep strength, and chemical stability [35, 36]. Embedding oxide dispersion in the matrix of FM steels can address the deficiencies of high-temperature strength [37]. Small Y_2O_3 nanoclusters are uniformly dispersed in the steel matrix with a high number of density ($\sim 10^{23} m^{-3}$ [37]). The co-addition of elements such as Ti and Zr were extensively investigated to control oxide particle size and stability. It turns out that a small amount of addition of Ti can effectively reduce the oxide particle size and improve the creep rupture strength [38]. Stability is still maintained in intense neutron irradiation environment, and at temperatures as high as 1400 °C, around $0.9 T_m$, where T_m denote melting temperature. Hirata et al. [39] attributes such unusual stability of the oxide nanoclusters to defective NaCl structure with a high lattice coherency with the BCC steel matrix. It means that the interface energy between oxide and matrix is very low and can effectively prevent particle coarsening. In the presence of radiation, there have not been consistent observations on the particle size evolution as a function of dose [37]. Size reduction and density increase generally shows up only at higher temperature and dose (see Figure 2-7 for an example). Overall, the fine dispersion with long-term stability create extensive sites to absorb defects, thus such designs are inherently radiation tolerant.

2.3.3 Nanostructuring

Nanostructured materials provide extensive interface areas of defect sinks accounting for the high radiation tolerance. Nanostructure can be in the forms of nanocrystalline, nanotwinned, nanolayer, nanoporous, and nanowires. Figure 2-8 depicts the applications. Zhang et al. comprehensively [40] summarized recent studies on these emerging materials. Although the key idea is to create defect sinks by increasing boundary areas, the underlying mechanisms are drastically different. For example, it is proposed
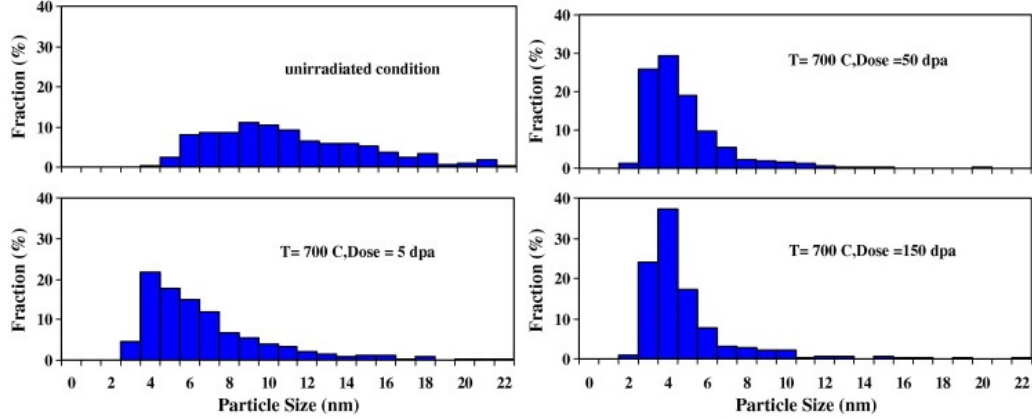
Figure 2-7: Oxide size distribution for samples irradiated with Ni ion at 700 °C to 0, 5, 50, and 150 dpa [37].

that nanotwinned metals accommodate additional defects by the incoherent segments on the coherent twin boundaries. In nanoporous materials, the abundant free surfaces are considered as effective sinks, where defects clusters including dislocation loops and SFTs can be absorbed [41]. Misra et al. [5] showed that the interfaces of Cu-Nb nanolayered composites can effectively trap point defects and rapidly remove them due to the greatly reduced formation energy of interfacial defects, which traces back to the unique structural characteristics of the interfaces.

2.3.4 High entropy alloys

High-entropy alloys (HEAs), with multiple elements in near-equiatomic composition, have recently received extensive attention because of the excellent properties in contrast with traditional alloys containing one primary element, such as high strength, structural stability, thermal stability, and corrosion resistance. Such alloys exhibit simple BCC or FCC crystal structure. The compositional complexities and local lattice distortion of the random well-mixed solution effectively reduce damage accumulation. Figure 2-9 shows the void distribution for several Ni-containing equiatomic materials after Ni ion irradiation at 773 K. It can be seen that much smaller voids in NiFe and NiCoFeCr, which implies higher swelling resistance than Ni and NiCo. Zhang et al. observed that suppressed damage accumulation by increasing the con-
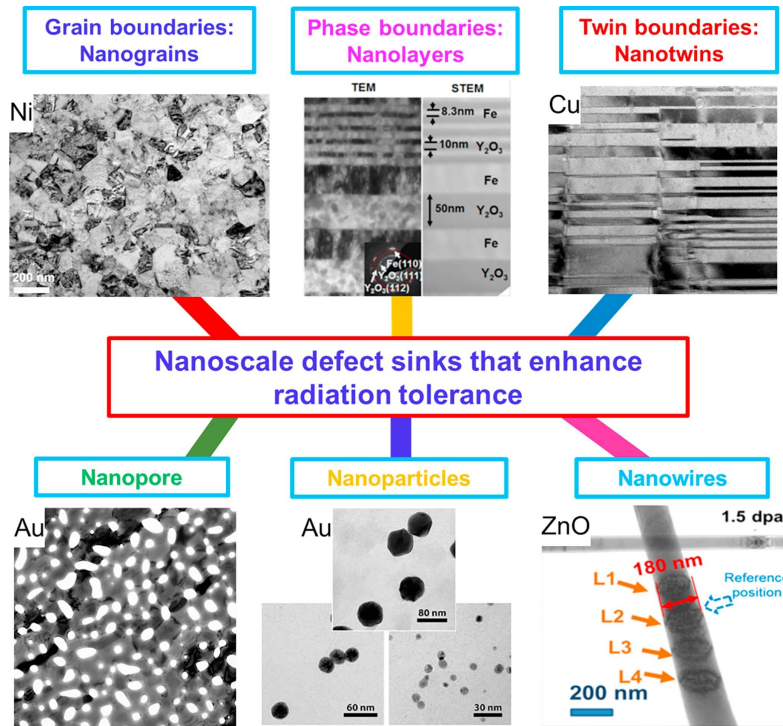
Figure 2-8: Nanostructured materials in various forms to improve radiation tolerance, including nanograins, nanolayers, nanotwins, nanopores, nanoparticles, and nanowires [40].

stituent elements [42]. Chemical alternation turns out to be an effective way to achieve higher radiation resistance [42–45]. This also calls for an effective design rule to optimize candidates for experimental testing.
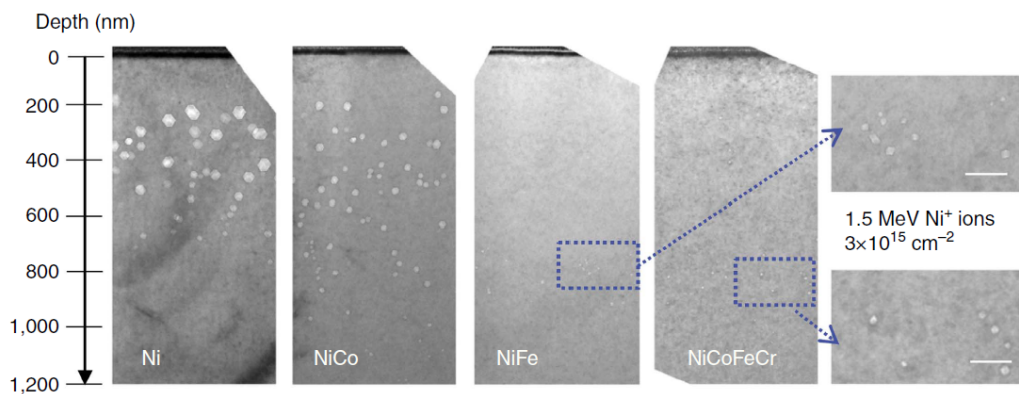
Figure 2-9: Cross-sectional TEM images on void distribution: Ni, NiCo, NiFe, and NiCoFeCr irradiated with 1.5 MeV Ni$^+$ ions to 3×10^{15}cm^{-2} at 773K, scale bars in rightest zoomed images are 50 nm [46].

2.4   Summary

Radiation effects are heavily dependent on both material internal properties (e.g. crystal structure, microstructure, and composition) and external conditions (e.g. such as radiation type, temperature, dose rate, and stress state). The complexity in real systems where multiple physical processes may dominate, introduces knowledge gaps in building theoretical descriptions and computational models. In this sense, understanding the fundamental mechanisms in controlling defect dynamics and ultimately predicting material behavior under prolonged irradiation is of utmost importance to assess material performance with high fidelity. In the next Chapter, efforts are paid to examine the radiation behavior of selected material systems including high entropy alloys and nanocrystalline materials using atomistic simulations; they build the foundation of more extensive investigation and optimization of the aforementioned new material designs.

Chapter 3

Atomistic characterization of radiation-induced defect dynamics

Atomistic simulations on simulating damage cascades on the order of tens of pico-seconds render a complete picture of the primary damage stage of radiation damage, and deliver an atom-resolved resolution. By tracking atom trajectories, detailed evolution process and interaction mechanisms can be uncovered. Conventional simulations commonly assign an atom with a high energy which constitutes the single-cascade simulation, however, it limits the scope of study and may generate misleading results, as continuous irradiation is expected in realistic scenarios. To break such limitation, an algorithm is developed to consecutively introduce damage cascades into the system to simulate continuous irradiation. The subsequent analysis generates experiment-consistent observations and uncovers mechanistic understanding towards radiation resistance. The following sections detail these findings in high entropy alloys and nanocrystalline materials.

3.1 Radiation resistance in high entropy alloys

Declaration: This section mainly cites from my published work in [4], with permission from the publisher.

3.1.1 Introduction

The main technical impediment to the development of advanced nuclear power systems lies in the creation of radiation-resistant structural materials. Various approaches are under active research, ranging from oxide dispersion strengthened (ODS) steels [47], to nanograined alloys [48], to severely plastically deformed (SPD) materials [49]. Recently, a new class of materials, called single-phase concentrated solid solution alloys (SP-CSAs) [50], including high entropy alloys (HEAs) [51], has received great attention due to their extraordinary, potential radiation resistance [44]. SP-CSAs are typically composed of two or more principle elements in a simple, single-phase solid solution, with near-equiatomic concentrations. The random arrangement of atoms results in a complex local atomic environment [42], with implications ranging from high strength [52] while retaining ductility [53], to high fracture toughness [54], to excellent corrosion resistance [55]. Moreover, recent experiments and simulations indicate that these single-phase alloys have significantly better radiation resistance than their corresponding elementary metals [44, 45].

Varying alloy elemental concentrations and types changes the local atomic environment, which can significantly influence the migration energy barriers and pathways of radiation defects. This has been demonstrated by tuning the composition of alloys to increase their radiation damage tolerance. Wang et al. found that radiation-induced defect sizes resulting from ion irradiation of Ni-Cu alloys decrease when increasing the Cu concentration from 10% to 50% [56]. Jin et al. and Zhang et al. observed enhanced radiation tolerance in Ni-Fe alloys by increasing the Fe concentration up to 60% [57, 58], and suggested chemical disorder be a key factor for controlling radiation performance [57]. Molecular dynamics (MD) simulations of radiation damage accumulation have been studied intensively from elementary metals to many SP-CSAs [43–45], revealing that more alloying (both in species and concentrations) demonstrates higher radiation resistance. However, these investigations focus on the reduction of damage in a few selected alloys in comparison to elemental Ni. A comprehensive understanding of the effects of alloy composition, defect

dynamics, damage accumulation, and defect recombination are necessary to gain a more fundamental basis for designing radiation tolerant alloys.

In this work, radiation-induced defect evolution and damage accumulation in elemental Ni and $Ni_{1-x}Fe_x$ alloys with x ranging from 10-90% have been studied. The face-centered cubic (FCC) structure is considered so as to study the pure effect of the single variable of Fe concentration x on radiation resistance, without introducing any additional complexity of crystal structure. However, it should be noted that when x is larger than $\sim 70\%$, the FCC system is in a thermodynamically metastable state. A hybrid Monte Carlo and Molecular Dynamics (MC+MD) approach (see Methods) is employed to prepare well-mixed systems. MD is then utilized to impose consecutive radiation collision cascades to achieve radiation doses of about 0.5 DPA (displacements per atom) (See Methods). By analyzing defect production and evolution, it has been found that defect accumulation clearly shows a dependence on alloy composition, and the rate of damage accumulation is controlled by the speed of large defect cluster growth. The largest reduction in damage is observed near the minimum of mixing energy. To obtain a more fundamental understanding of the results, defect migration energy barriers and pathways of point defects in these alloys using the nudged elastic band (NEB) method [59] are examined. The variance of these barriers, which reflects the complexity of the local potential energy landscape (PEL), indicates increasingly heterogeneous point defect migration in the more highly radiation-tolerant compositions. These results provide atomistic details of damage evolution and reduction, suggesting a quantitative basis for developing radiation-tolerant materials.

3.1.2 Methods

3.1.2.1 Hybrid MC+MD simulations and atom swapping

$Ni_{1-x}Fe_x$ alloys are modeled using the embedded atom method (EAM) potential developed by Bonny et al. [60]. This potential is an improved version of the Bonny 2011 potential [61], which was developed to model the production and evolution of collision cascade-induced defects. It has been extensively applied to successfully

49

predict concentration-dependent radiation defects in NiFe alloys as observed in experiments [44, 58]. The initial FCC alloy structures is prepared by randomly mixing Ni and Fe atoms at each specified composition. The simulation cell contains 108,000 atoms, and periodic boundary conditions are applied in all three directions in all simulations.

One possible concern in atomistically simulating SP-CSAs involves the creation of the initial atomic structure. The approach used in previous MD studies [45,62,63] was to randomly replace one atom type with the other, which may not recreate truly mixed SP-CSA structures. This random procedure can produce local atomic structures with high potential energy, which are thermodynamically unstable. The as-prepared metastable system becomes a particular concern when simulating radiation damage, as the dissipation of damage energy and structural relaxation of the initial high-energy atomic configuration would become convolved. Recently, an effort to construct SP-CSAs via a quasirandom structure was made in [64], where the Warren-Cowley short range order [65] was optimized to produce a truly random atomic structure. In this work, a hybrid MC+MD algorithm [66, 67] is used to anneal each generated system. In each MC trial step, a randomly selected Ni atom is swapped with another randomly selected Fe atom. The trial move is accepted with a probability of unity or $P = exp(-\Delta U/k_\mathbf{B}T)$, whichever is smaller, depending on the value of ΔU, where ΔU is the change in system potential energy after the atom exchange and T is the system temperature of 300K. Following 100 MC trials, 0.1 ps of MD simulation is then performed in the isothermal-isobaric condition (NPT ensemble). This MC+MD procedures is repeated to anneal each alloy, and a total of 50,000 MC trials and 50 ps MD runs are performed. The equilibrated systems show much lower potential energies than those which were randomly generated.

3.1.2.2 Molecular dynamics simulations

The MD method as implemented in LAMMPS [68] is utilized to simulate self-ion radiation damage. To deal with high energy radiation damage collisions, a Ziegler-Biersack-Littmark (ZBL) repulsive potential [69, 70] is smoothly joined to the afore-

mentioned EAM potentials [21], and an adaptive time step algorithm is used to limit atomic movement to 0.05Å in each timestep. The choice of ZBL joining parameters could affect the generation of primary damage as discussed by Stoller et al. [71]. In this work, the smoothly joined potentials adequately capture the features of Fe concentration-dependent radiation defect production and evolution as seen in ion irradiation experiments. First, each system is relaxed at 300K for 100 ps. An atom is then randomly chosen as the primary knock-on atom (PKA), and the entire cell is shifted such that the PKA is at the center. This avoids the damage cascade from reaching the system boundaries. The PKA is assigned a kinetic energy of 5 keV, and 50,000 adaptive timesteps of MD simulation (~45ps) are performed. The Nosé-Hoover temperature-rescaling thermostat [72, 73] is applied to the atoms at the sides of the simulation cell with a width of half the lattice constant, to absorb the collision cascade energy and cool the system to 300K. This process is repeated with each PKA randomly chosen and shifted to the center of the cell, simulating the spatially random arrival of radiation damage cascades. Up to 1500 consecutive 5 keV cascades result in radiation damage levels of ~0.5 DPA. The short simulation time (an inherent limitation of MD) between collision cascades yields a dose rate several orders of magnitude higher than that in experimental conditions. Although the difference in dose rate between MD and experiments is quite large, a recent study using similar approaches has shown good agreement with experiments [44]. Twelve independent 1500 consecutive 5 keV cascade simulation runs for each system were performed to obtain more reliable results. Defects are identified by comparing the irradiated system with the initial perfect structure using Wigner-Seitz cell method. Defects analysis and visualization are realized with the OVITO package [74] using an adaptive common neighbor analysis.

3.1.2.3   Defect migration energy barrier calculations

Vacancy and interstitial migration energy barriers are computed with the climbing image nudged elastic band (NEB) method [59]. By removing one atom from the equilibrated system, a vacancy is created and all twelve (not necessarily equivalent) diffusion pathways on the FCC lattice are considered by exchanging with the twelve

first nearest neighbors. The NEB method is used to identify the saddle point along each minimum energy pathway, and from that the migration energy barrier is calculated. Considering all possible vacancy sites in the relaxed system, the energy barriers corresponding to ~10,368 pathways are evaluated. Similarly, by inserting Ni or Fe atoms into the lattice, [100] dumbbell interstitials are created. Note that due to local lattice distortion, placing an atom at the designated position may not create the desired dumbbell structure after relaxation. Therefore, extreme care needs taken to confirm the initial and final configurations for interstitial migration. Only valid rotations are considered in the calculations.

3.1.3   Results

3.1.3.1   Annealed alloy systems and their mixing energies

By preparing a stable, well-equilibrated single-phase alloy using the hybrid MC+MD method, the system potential energies are effectively reduced for all alloys studied, indicating a more energetically favorable system (Figure 3-1). The radial distribution function $g(r)$ of Ni and Fe in $Ni_{40}Fe_{60}$ in Figure 3-2(a) clearly demonstrates the atomic structural differences between the two systems (randomly prepared and MC+MD annealed). Both the Ni and Fe distributions exhibit a smaller first peak and a larger third peak in $g(r)$ in the annealed system, showing that more dissimilar atoms become first nearest neighbors after the MC+MD swaps. This change in $g(r)$ implies that a better mixed Ni-Fe structure is obtained after the annealing operation.

The equilibrated Ni-Fe alloy systems enable precise measurement of the mixing energy ΔE, a change in energy caused by elemental mixing. Before mixing, the system energy E_0 can be computed as $E_0 = E_{Ni}N_{Ni} + E_{Fe}N_{Fe}$, where E_{Ni}, E_{Fe} are per-atom energies of Ni and Fe, and N_{Ni}, N_{Fe} are the numbers of Ni and Fe atoms, respectively. The inset of Figure 3-2(b) shows how E_0 and E_f vary with changing Fe concentration. The mixing energy ΔE defined as $\Delta E = E_f - E_0$ is plotted as a function of Fe concentration in Figure 3-2(b), where a local minimum is noted near the vicinity of equiatomic concentration.
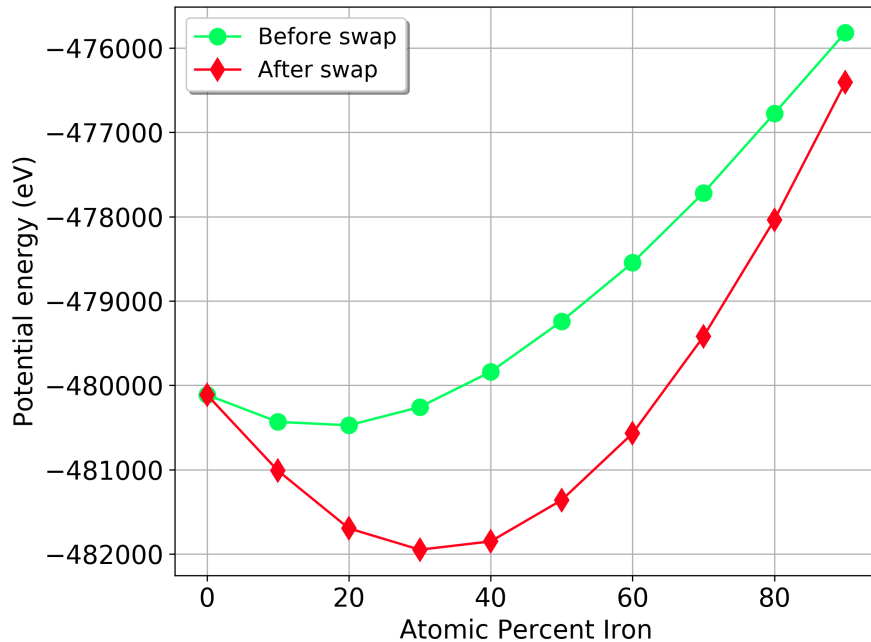
Figure 3-1: Comparisons of randomly generated system energy with MC+MD annealed system. The annealed systems show smaller energies for all alloy compositions, showing that better-equilibrated configurations are obtained after MC+MD relaxation. The energy is computed based on system of containing 10,800 atoms.

3.1.3.2 Radiation damage accumulation

The level of defect production during irradiation can be obtained by analyzing the atomic structures from the MD simulations of consecutive damage cascades. Figure 3-3(a) presents a heat map of damage accumulation, with the x- and y-axes representing Fe concentration and number of cascades, respectively. The map is color coded by the number of defects (Frenkel pairs) remaining after each damage cascade. The map shows that the level of damage increases with subsequent cascades, while the rate of defect accumulation clearly depends on alloy composition. Figure 3-3(b) provides a supplementary view on the trend for selected compositions with Fe ranging from 0% to 50%. It can be seen that the number of defects is essentially the same for these compositions up to around 50 cascades, implying that defect production from the initial stages of radiation damage depends weakly on composition. At this stage, damage from consecutive cascades has not yet begun to significantly overlap,
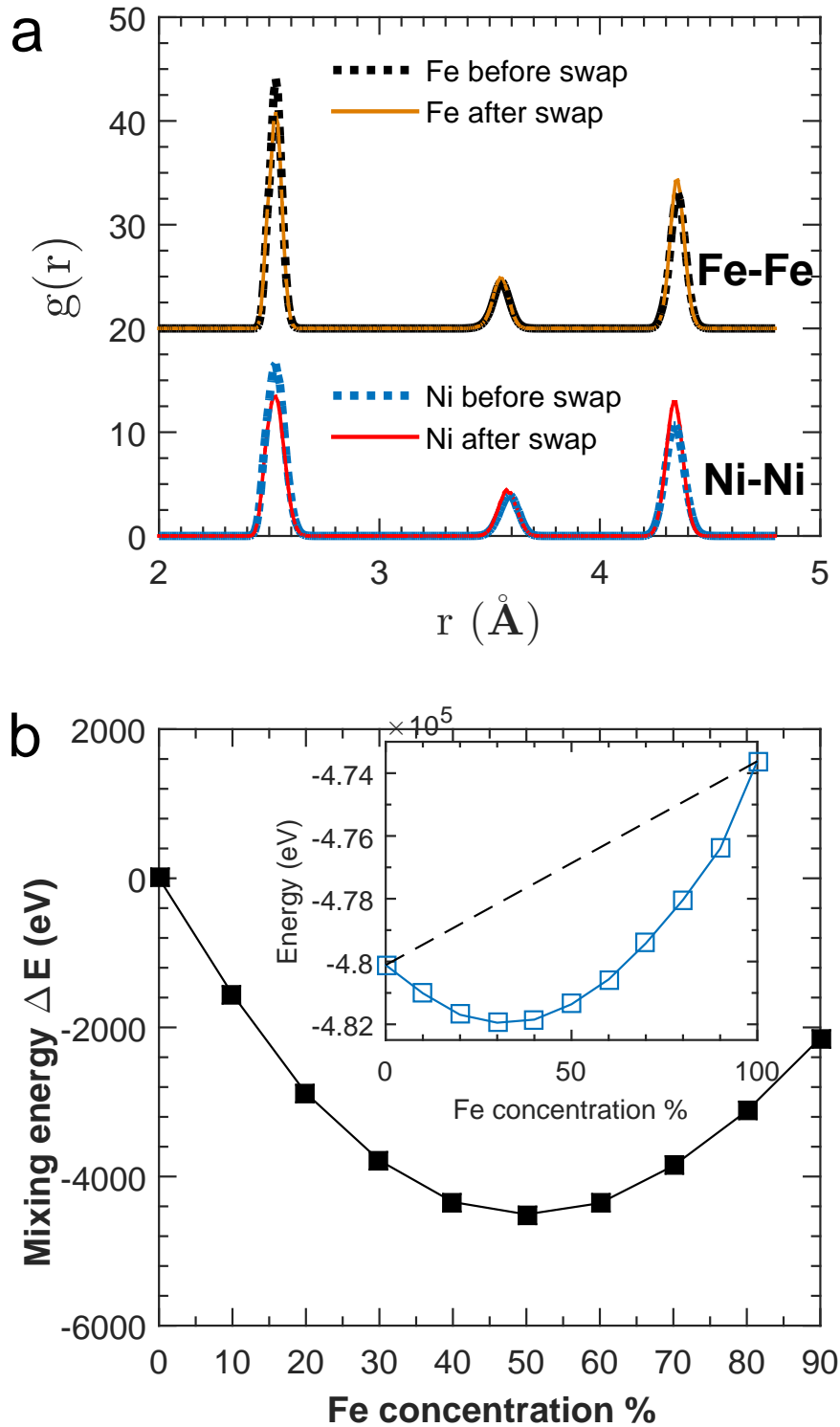
Figure 3-2: (a) Radial distribution function $g(r)$ for Fe-Fe and Ni-Ni before (i.e. randomly generated configuration) and after MC+MD swap annealing of $Ni_{40}Fe_{60}$. (b) Mixing energy ΔE versus Fe concentration. The blue squares in the inset show the energy of the annealed system E_f, while the black dashed line shows the energy E_0 before mixing.

and the discrete cascades mainly produce localized point defects (see Figure 3-3(b)). However, the curves start to separate after 100 cascades, and defect accumulation shows a clear dependence on composition with a significant reduction in damage with increasing Fe. It is reasonable to assume that this observed damage reduction at high Fe concentrations is the result of enhanced defect recombination. In recent low fluence ion irradiation experiments, a similar behavior has been reported in elemental Ni and Ni-Fe alloys [57, 58].

To clearly see how damage accumulation depends on material composition, Figure 3-4(a) shows the number of defects as a function of Fe concentration at different damage levels. At all damage levels, the number of defects initially decreases with increasing Fe, and then starts to increase. The very low damage level of 300 cascades displays a maximum damage reduction near the equiatomic composition, i.e. 50% Fe, at which the system also has the largest magnitude of mixing energy as shown in Figure 3-2(b). With an increasing number of collision cascades, it can be seen that the composition with the minimum number of defects slightly shifts to 60% Fe, in agreement with recent ion irradiation experiments of Ni-Fe alloys [58]. The interesting shift of minimum defects at higher damage levels highlights the effects of defect dynamics and diffusion on damage accumulation, which will be analyzed in detail in the following subsection. To highlight the good agreement between the experimental observations and the simulation results, the damage level as measured by backscattering yield for various Fe concentrations up to 60% is shown in the inset of Figure 3-4(a).

The amount of radiation damage can be further connected with the mixing energy ΔE in Figure 3-4(b), where the number of surviving defects is plotted against mixing energy for all simulated materials (including Ni and nine $Ni_{1-x}Fe_x$ alloys). In the early stages of radiation damage (300 cascades), the damage is strongly correlated with mixing energy ΔE with an excellent linear fit. After 900 cascades, the damage is still an essentially linear function of ΔE, though it does exhibit a somewhat weaker dependence. The results show that the energy change during alloy mixing correlates well with radiation tolerance, suggesting that ΔE may serve as a key metric when
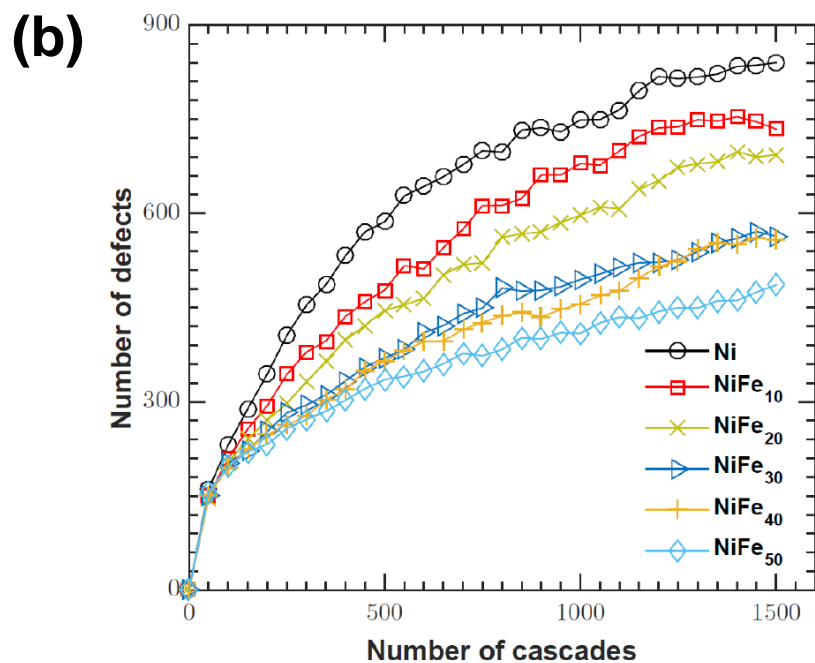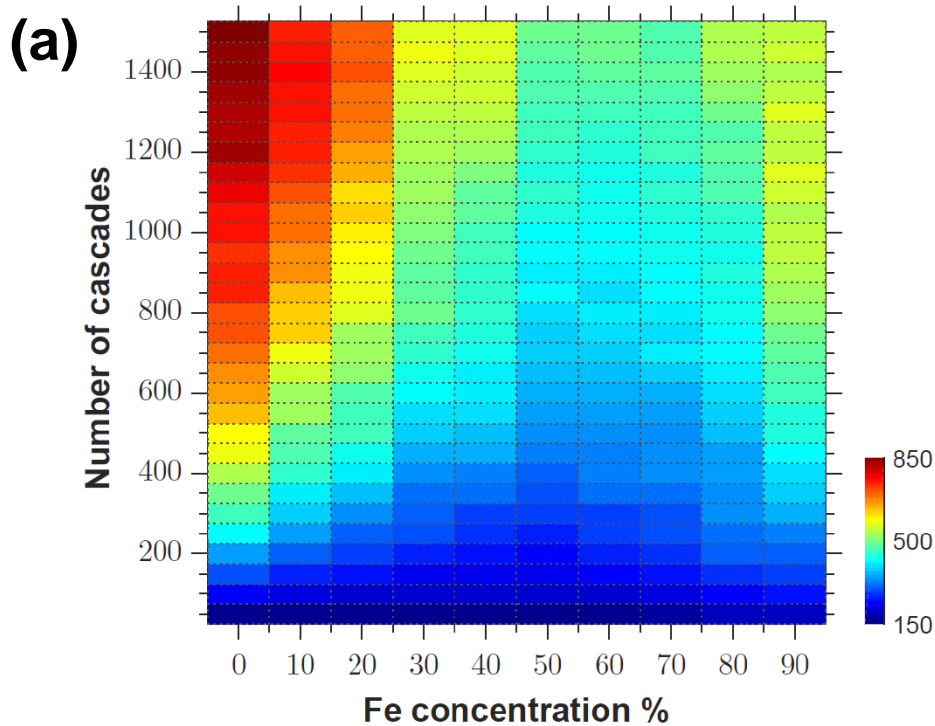
Figure 3-3: (a) Damage production map for elemental Ni and $Ni_{1-x}Fe_x$ alloys with various Fe concentrations, subjected to radiation damage from up to 1500 consecutive cascades ($\sim$ 0.5 DPA). For each composition, the map is color coded by the average number of defects (Frenkel pairs) produced from twelve independent simulations. (b) Number of defects as a function of number of cascades for Ni and various Ni-Fe alloys as indicated.

56
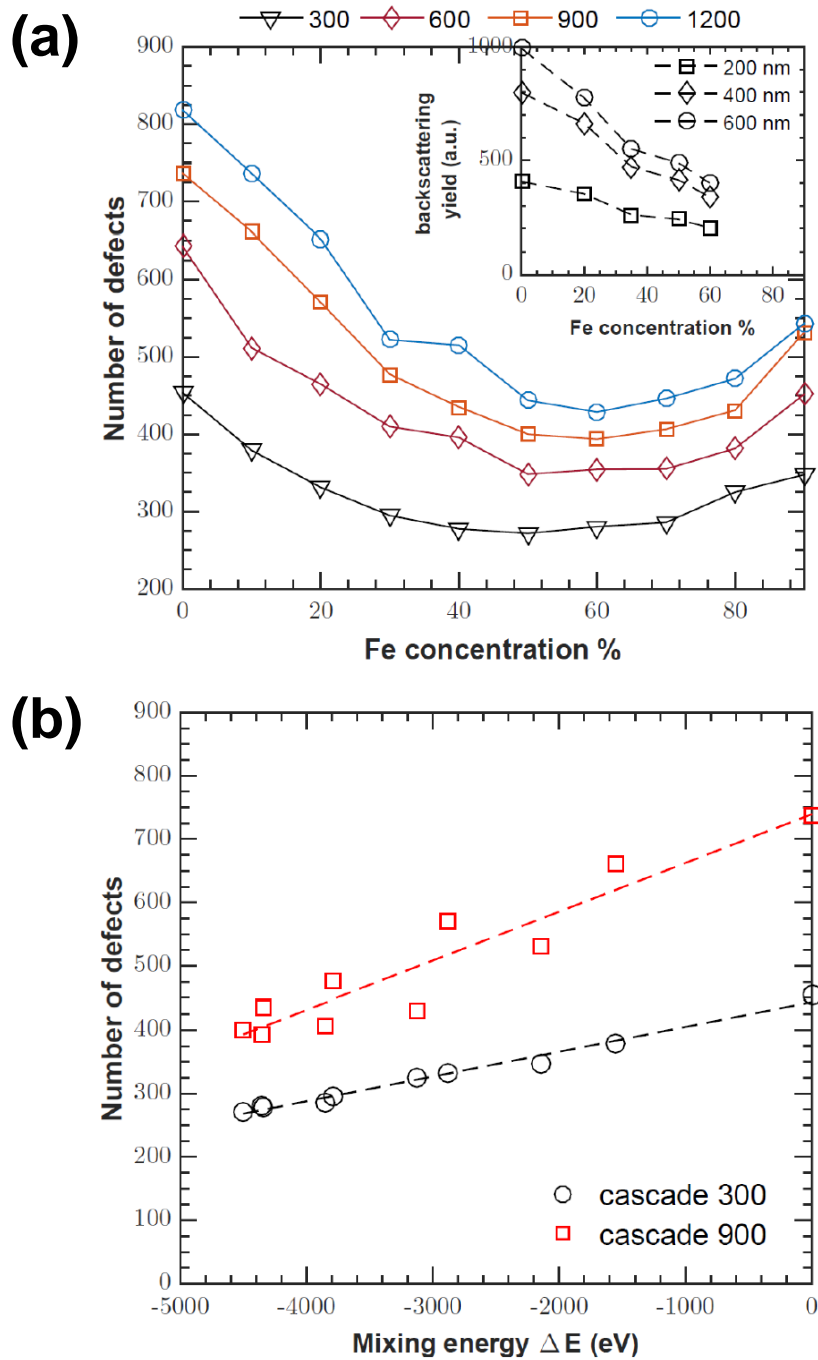
Figure 3-4: (a) Fe concentration-dependent defect production at different stages of radiation damage (300, 600, 900 and 1200 cascades). The error bars indicate one standard deviation. The inset shows experimentally measured radiation damage at different depths, as a function of Fe concentration from 0 to 60% [58]. (b) Correlation between radiation damage and mixing energy ΔE for Ni and nine $Ni_{1-x}Fe_x$ alloys.

designing radiation-resistant single-phase alloys.
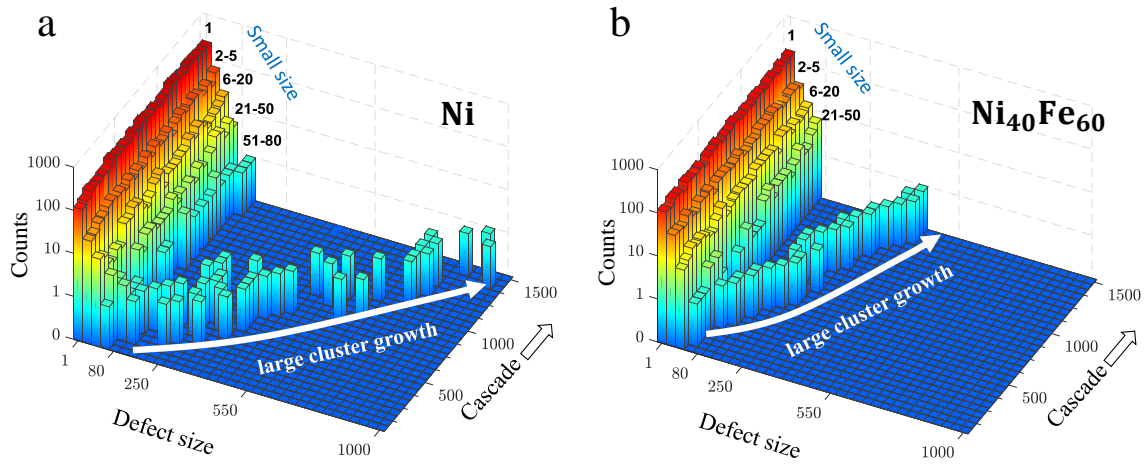
Figure 3-5: Evolution of defect size as a function of damage cascades for (a) Ni and (b) $Ni_{40}Fe_{60}$.
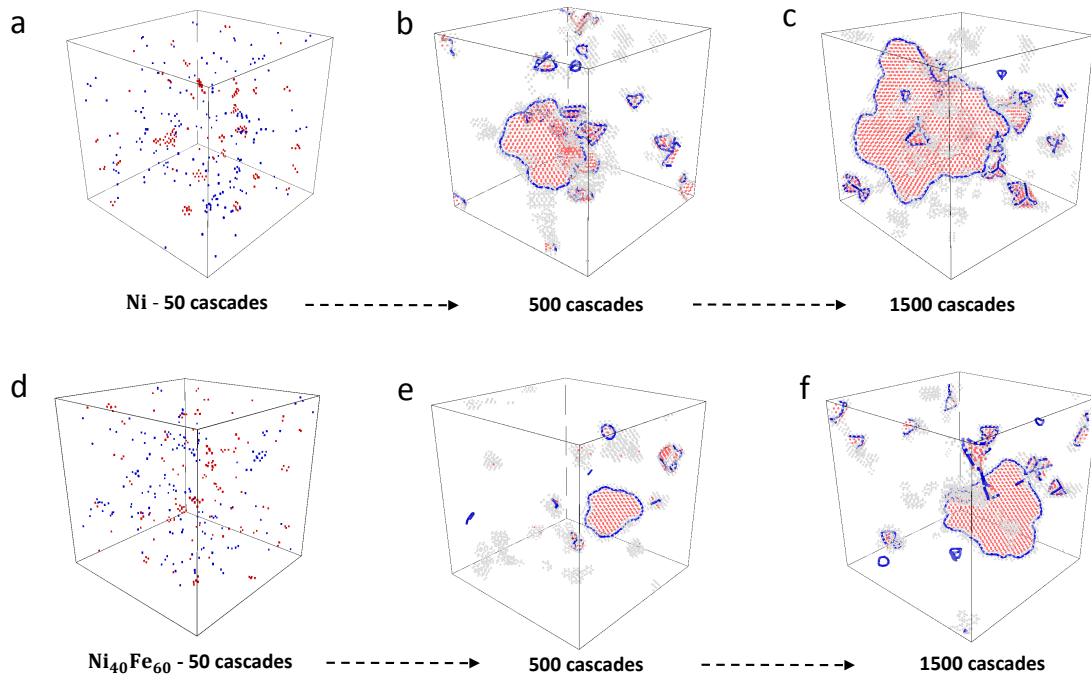
Figure 3-6: Defect distributions at different damage stages in Ni and $Ni_{40}Fe_{60}$. (a)(d) Point defects produced after 50 cascades. Red indicates interstitials, while blue shows vacancies. (b)(c) and (e)(f) Ordered defect structures formed at 500 cascades and grown in size at 1,500 cascades in Ni and $Ni_{40}Fe_{60}$, respectively. Only large defect cluster are shown. The atoms shown have non-FCC structures. The red atoms are hexagonally close packed (HCP) stacking faults, while the solid lines indicate dislocations.

3.1.3.3 Atomistic processes of defect evolution

Figure 3-3 summarized the defects produced by radiation for different $Ni_{1-x}Fe_x$ compositions, indicating that stoichiometry has a significant effect on damage reduction. One then must know the details of defect evolution associated with the observed damage accumulation, to mechanistically understand the dynamical processes of radiation damage. A detailed analysis of defect size distributions as a function of dose in irradiated Ni and $Ni_{40}Fe_{60}$ is presented in Figure 3-5(a-b). The size distributions (bar graphs) are colored by the number of defects in each size bin, ranging from 1 to 1000 atoms. These plots show the evolution of small (size<50) and large (size>80) defects to clearly differ. The number of small defects quickly saturates for both materials, while larger defects continue to grow throughout the simulated damage stages. Recall in Figure 3-3(b) that the total number of defects continues to increase with successive cascades. It is reasonable to conclude from Figure 3-5 that the radiation damage accumulation is essentially governed by the growth of larger clusters. The behaviors of radiation-induced defects are particularly interesting when comparing $Ni_{40}Fe_{60}$ with Ni, as one can see in $Ni_{40}Fe_{60}$ that the saturation density of small defects is smaller, and the growth of large clusters is significantly slower.

To see which defect types could be associated with the behavior in Figure 3-5, the details of the atomic structures of the damaged materials can be analyzed. The spatial distributions of defect structures in Ni and $Ni_{40}Fe_{60}$ after different numbers of cascades are presented in Figure 3-6. After 50 cascades, both Ni and its alloys display similar point defect distributions (Figure 3-6(a)(d)). However, after 500 cascades, one can clearly see the growth in defect cluster size, and ordered defect structures such as stacking faults and dislocation loops are formed as shown in Figure 3-6(b) and (e). The formation of ordered defects and their growth is more pronounced in Ni (Figure 3-6(c)), as far more atoms are involved in processes of defect agglomeration in Ni compared to $Ni_{40}Fe_{60}$ (Figure 3-6(f)). One can see stable defect structures forming at the early stages of radiation damage (about 100 cascades) in Ni, which rapidly expand in size when interacting with surrounding defects. By contrast $Ni_{40}Fe_{60}$ develops

stable defect structures after ~380 cascades, which implies inherent resistance to defect growth.

The results presented in Figure 3-5 and 3-6 show that certain alloy compositions have higher resistances to the formation of large clusters. This may be interpreted from the two perspectives of thermodynamic mixing energy and defect dynamics. At the system level, the large absolute value of mixing energy of an alloy implies a strong propensity for better mixing between Ni and Fe atoms, and an inherently energetic resistance to the formation of large-scale defect structures. This point has been discussed before, as Zhang et al. have noted energy dissipation as a controlling factor in radiation resistance [57]. This is because most defects represent less elemental mixing with higher potential energy when compared to a properly mixed, unirradiated alloy. At the microscale, the dynamic behaviors of defects play an essential role in damage reduction and accumulation. In Figure 3-4(a), the increase in radiation damage resistance when increasing the Fe concentration from 0 to 60% is attributed to the enhancement of defect annihilation. To understand these defect dynamics, the dynamical diffusion of vacancies and interstitials can be examined through their migration pathways and energetic barriers.

3.1.3.4 Heterogeneity of defect migration

The dynamical behavior of defects in a material can be determined by its underlying PEL, where defect migration corresponds to the hopping (thermal activation) process between neighboring local energy minima. A schematic illustration of hopping in the PEL is shown in Figure 3-7(a-b). The types of migration pathways of point defects in Ni are very limited due to the inherent symmetry in the PEL. In contrast to Ni, the migration pathways are much more complex in alloys as a result of local atomic complexity and lattice distortion, which generate anisotropic stress fields and make diffusion intrinsically heterogeneous (Figure 3-7(b)). Here, the characteristics of PELs is explored by sampling energy barriers $E_{\mathbf{b}}$ along defect (interstitial and vacancy) migration pathways, where $E_{\mathbf{b}}$ is the energy difference between an initial local minimum and a nearby saddle point. A significantly large number of pathways

are sampled to obtain good statistics (see Methods). As a demonstration, one sample path for vacancy and interstitial migration is shown in Figure 3-7(c). Results of energy barrier distributions for all compositions are listed in Figure 3-9 and 3-10, where a constant migration energy in Ni is indicated by the dashed vertical line. The variance of these distributions reflects the roughness of the PEL, and hence the heterogeneity of diffusion.
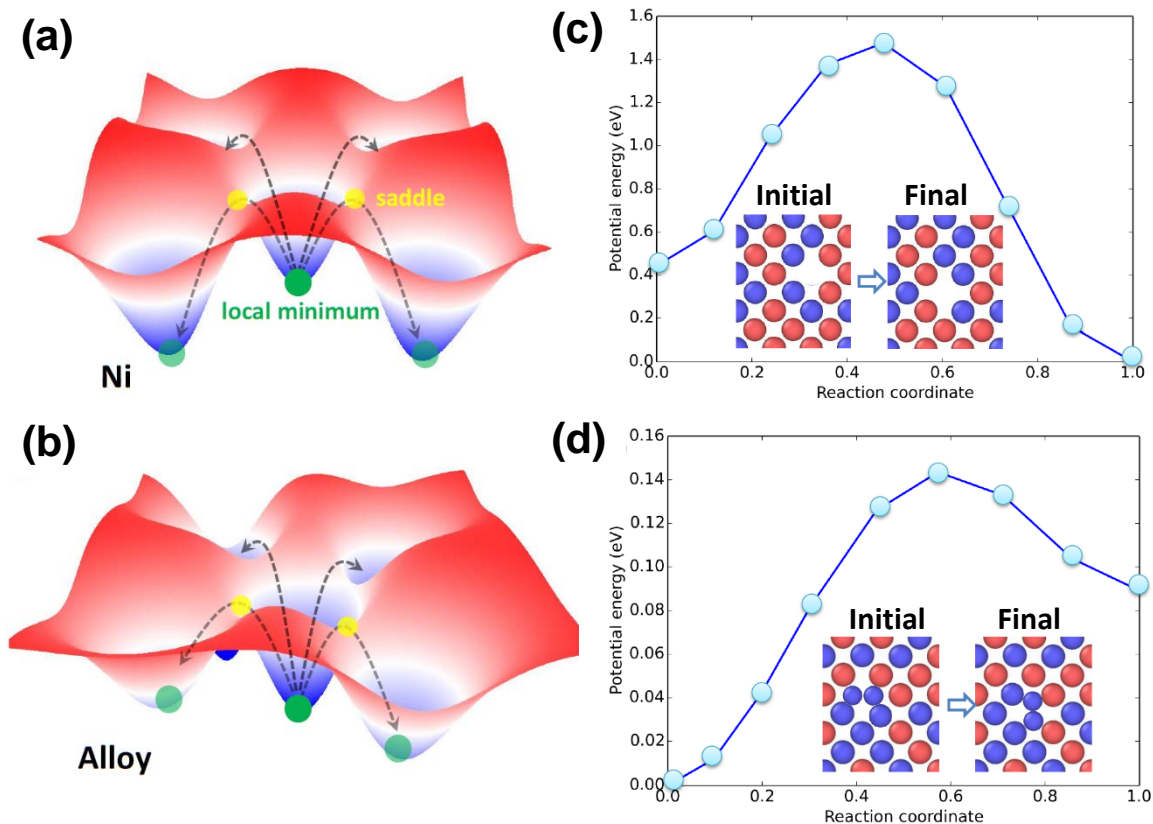
Figure 3-7: (a-b) Schematic illustrations of defect migration pathways in the potential energy landscape (PEL) for Ni (a) and (b) Ni-Fe alloy, respectively. The energy difference between a local minimum and nearby saddle point constitutes the energy barrier for defect migration. (c-d) Two examples of NEB computed point defect migration minimum energy pathways (MEPs). The insets illustrate the corresponding initial and final atomic configurations. (c) The calculated MEP for a vacancy exchanging position with one of the neighbors indicated. In this work, all possible 12 pathways for each atom are considered. (d) MEP for interstitial [100] dumbbell rotation MEP. The migration barrier is energy difference between initial state and activation state (saddle point).

These histograms show considerable spread in the distribution of local defect mi-

61
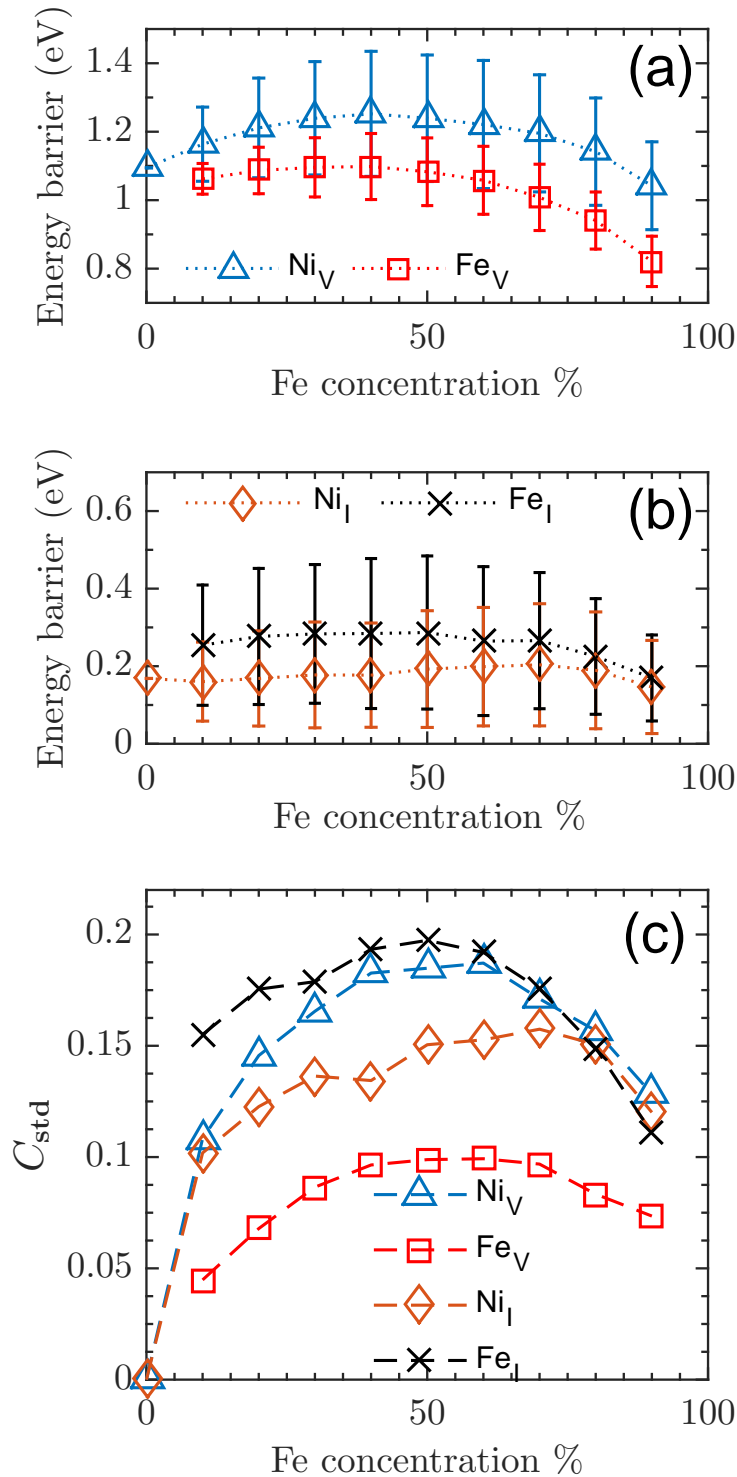
Figure 3-8: (a) Average vacancy migration energy barrier versus Fe concentration in $Ni_{1-x}Fe_x$ alloys. The error bars represent one standard deviation c_{std}. (b) Average interstitial migration energy barrier versus Fe concentration. (c) Standard deviation of the migration energy barrier c_{std} for all defect types versus Fe concentration.

gration barriers. While the mean value of each distribution would be cited as its 'migration energy', the broad spread in local migration energies should be noted especially for compositions near $Ni_{40}Fe_{60}$. Similar computations for the full range of $Ni_{1-x}Fe_x$ alloys are summarized in Figure 3-8(a-b). The diffusion processes are dominated by low energy pathways according to transition state theory [75], which means that unlike elementary Ni, diffusion in $Ni_{1-x}Fe_x$ alloys is spatially heterogeneous and directionally anisotropic. The standard deviation c_{std} of energy barriers in each alloy is calculated to quantify its diffusional heterogeneity, as shown in Figure 3-8(c). The values of c_{std} for both vacancies and interstitials increase with Fe concentration, and then decrease at around 60% Fe. Particularly interesting is the observation that c_{std} negatively correlates with the accumulation of radiation damage (Figure 3-4(a)). The comparison suggests that the more complex PEL of alloys results in heterogeneous diffusion of vacancies and interstitials, enhancing the recombination of defects.

3.1.4   Discussion

By simulating consecutive damage cascades in Ni and Ni-Fe alloys, it has been shown that defect production in the initial stages of radiation damage is similar across all $Ni_{1-x}Fe_x$ alloys. Nevertheless, some alloys are more efficient at annihilating defects and restoring their crystal structures over longer periods of irradiation, thus demonstrating better radiation tolerance. It has been found that the such tolerance correlates strongly with mixing energy ΔE, thus minimizing ΔE may be an indicator of improved irradiation performance.

The notion that the energy of mixing (related directly to alloying energy or the enthalpy of formation) may be a descriptor of stability in catalysts has been discussed previously by Greely et al. [76] and Vej-Hansen et al. [77], who demonstrated a strong correlation between diffusion barriers of the minority component and alloying energy in Pt/Pd/Al-based binary alloys. Mantina et al. show that these energies are intimately related to the first-principles calculation of diffusion constants [78]. In the scenario of radiation damage in Ni-Fe alloys, it has been found that such a simple thermodynamic measure scales extremely well with the resistance to disorder.
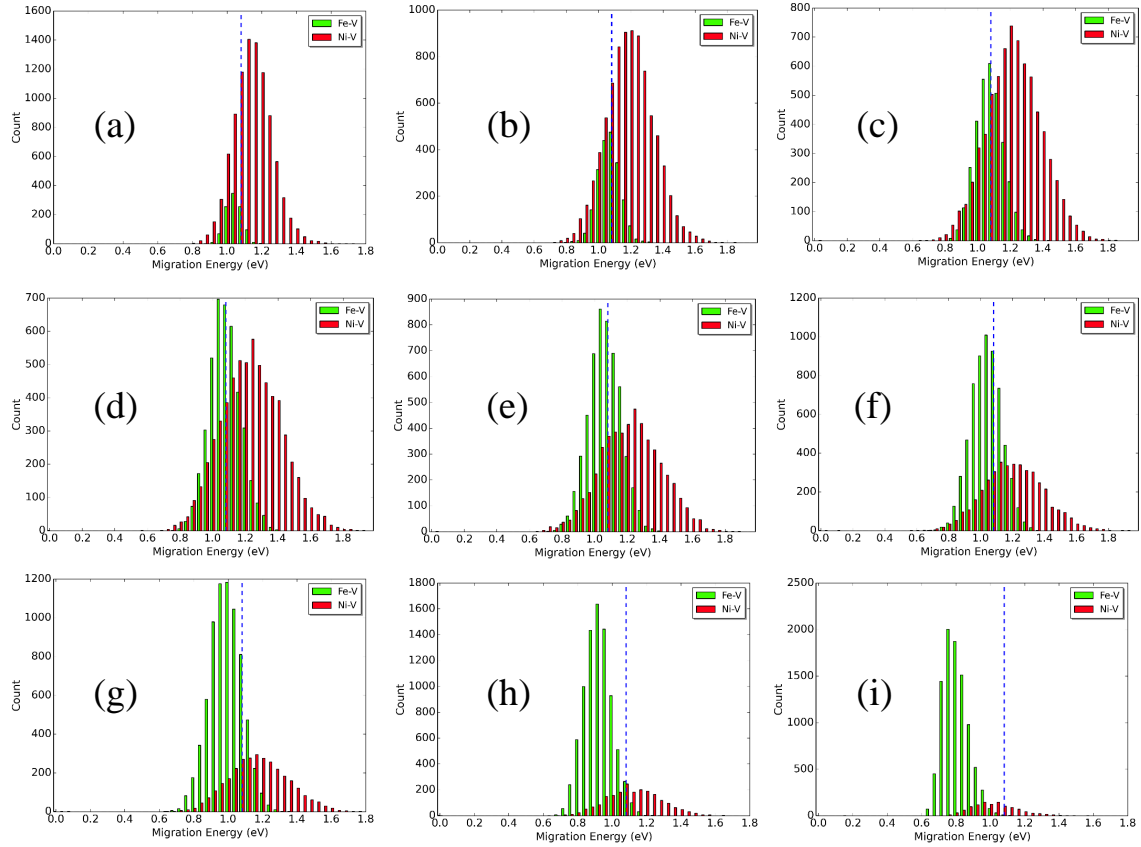
Figure 3-9: Distributions of Ni- and Fe-vacancy migration energy barriers in $Ni_{1-x}Fe_x$. (a)-(i) correspond to x = 10%-90%, respectively. The vertical dashed line denotes the migration energy barrier for pure Ni. The energy barriers are calculated for $\sim$10,368 paths.
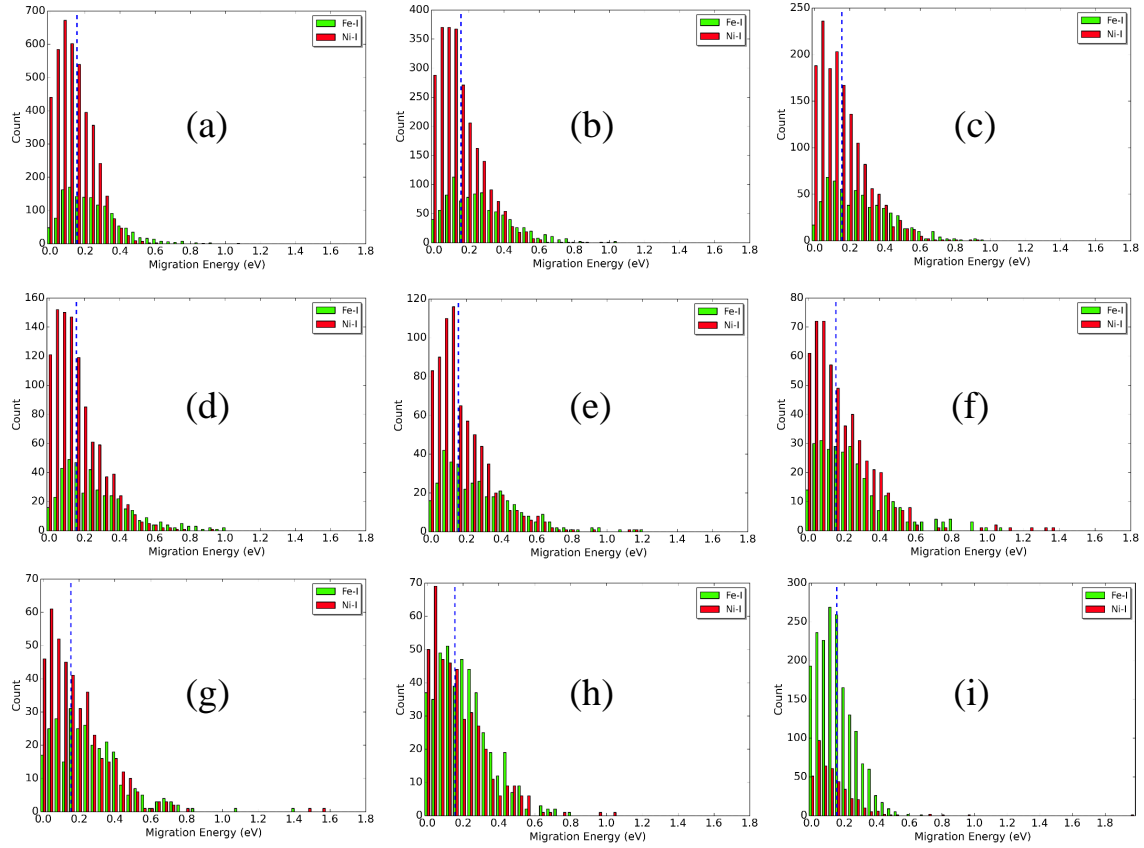
Figure 3-10: Distributions of Ni- and Fe-interstitial migration energy barriers in Ni$_{1-x}$Fe$_x$. (a)-(i) correspond to x = 10%-90%, respectively. The vertical dashed line denotes the migration energy barrier for pure Ni.

A mechanistic explanation for the enhanced radiation resistance of alloys which energetically favor mixing lies in the modification of defect migration dynamics. The different compositions and atomic sizes of elements in SP-CSAs substantially reduce electron, phonon, and magnon mean free paths [57], which influence defect formation energies and their dynamical evolutions. The differences of atomic size and type specifically lead to lattice distortion, producing local structural complexity. It is known that the defect diffusion pathways and their associated migration barriers are governed by their surrounding atomic structures. The wide distribution of migration barriers on the complex PEL results in significant heterogeneous defect diffusion processes, which enhance the recombination of radiation-induced defects as observed in the simulations. It has been reported in recent experiments that the heterogeneity of defect diffusion makes alloys more radiation resistant than pure metals. Lu et al. [46] explained in a recent study that the three dimensional (3D) migration of interstitial clusters rather than one dimensional (1D) crowdion diffusion accounts for the enhanced radiation resistance of NiFe, NiCoFe, NiCoFeCr, and NiCoFeCrMn. The basic understanding is that defects moving in 3D forms, instead of faster-moving 1D crowdions, are confined to smaller regions of material and therefore increases the likelihood of recombination over clustering by long range migration. Here, diffusional heterogeneity from the spectrum of migration barriers of point defects is considered. It has been found the interstitial diffusion in highly radiation resistant alloys is significantly heterogeneous (high standard deviation in the distribution of migration barriers), which could potentially slow the clustering movement of interstitials across complex PELs. Hence a higher defect recombination rate is expected, which eventually results in fewer residual defects in the system.

To summarize, these simulation results on Ni-Fe alloys show that there is a strong correlation between the energy of mixing and radiation resistance. Conceptually, defect clustering becomes energetically unfavorable in SP-CSAs that strongly prefer mixing, and an enhanced defect recombination is then expected. The general understanding is that local compositional complexity significantly adjusts defect migration behavior, and ultimately modifies radiation performance. From a quantitative point

of view, the computation of point defect diffusion barriers demonstrated increasing heterogeneity of defect mobility in more radiation-resistant alloys. Further study is needed to confirm whether SP-CSAs containing more elements exhibit the same properties, and whether the energy of mixing correlates well with radiation resistance in more complex alloy systems. In the end, minimizing the mixing energy and enhancing diffusion heterogeneity in SP-CSAs may represent a promising design criterion to develop improved radiation-resistant materials for nuclear applications.

It should be noted that this study starts with perfect crystal with FCC structure, the high radiation resistance boils down to the efficient defect recombination enabled by the highly heterogeneous defect diffusion mode derived from the PEL. As mentioned in the Section 2, tuning the microstructure through nanostructuring can reinforce the exceptional radiation performance via increasing the defect sink density. In the next section, nanocrystalline pure metal (Cu) is analyzed in detail to highlight the effects of grain boundaries on radiation resistance.

3.2 Radiation resistance in nanocrystalline metals

Nanocrystalline materials have indicated very good radiation resistance, as introduced in Section 2. Although it follows the concept of increasing defect sinks provided by the grain boundary areas, the boundary-mediated defect annihilation mechanisms for the radiation performance are still under investigation. This study aims to provide detailed process of radiation damage and the mechanistic understanding of radiation resistance in the nanocrystalline Cu.

Declaration: This section mainly cites from my published work in [79], with permission from the publisher.

3.2.1 Introduction

Nanostructured materials, in the form of nanocrystalline [80], nanolayered [81], nanoporous [82], and nanodispersed [3] structures have received much attention due to their exceptional tolerance of radiation damage compared with their coarse-grained counterparts [49]. During irradiation, point defects including vacancies, interstitials, and defect clusters are produced by displacement cascades [83]. These defects further migrate and aggregate, forming larger clusters such as dislocation loops, interstitial clusters, stacking fault tetrahedra (SFTs) [84,85], and voids [86]. The continual alteration of the microstructure due to radiation leads to severe degradation of material properties, including radiation hardening [87,88], embrittlement [89], creep and swelling [90], and eventual material failure. In nanocrystalline (NC) materials, the high fraction of grain boundaries (GBs) or interfaces serve as defect sinks, ultimately contributing to defect reduction. Recently, NC materials have been intensely studied by *in situ* [91–94] and *ex situ* [80,95] ion irradiation experiments. It has been found that NC materials exhibit smaller defect sizes and lower defect densities than their polycrystalline counterparts [94,96]. Moreover, the defect cluster density shows strong dependence on the average GB spacing, with a more refined nanostructure giving rise to a lower defect density. It is reasonable to attribute these changes to GB-mediated defects annihilation, such as SFTs absorbed during their interaction

with twin boundaries [93,97]. Despite these successful experiments, the mechanistic understanding of GB-mediated SFT annihilation in these materials was not fully elucidated, mostly due to the inability to resolve the complexity at the atomic level.

To unravel the mechanisms of GB-mediated point defect annihilation, a number of atomistic simulations have explored how collision cascades interact with GBs. The influence of GBs on defect production was extensively investigated by many groups, including Samaras et al. [98,99], Bai and Uberuaga et al. [21,100], and Demkowicz et al. [101]. The GBs act as defect containers by preferentially absorbing collision cascade-produced interstitials. As a result, defect distributions are strongly biased by the GBs, leaving behind vacancy-rich bulk regions and interstitial-concentrated GBs [49,99,102]. The interstitial-rich GBs lower the energetic barriers to interstitial migration and efficiently emit interstitials to interact with nearby vacancies, leading to enhanced interstitial-vacancy recombination processes [21,103].

In addition to point defects, clustered defects such as SFTs are the predominate type in many irradiated face centered cubic (FCC) metals including Cu, Ag, Ni and Au [97,104]. Dislocation pinning by these radiation-induced defect clusters increases the resistance to plastic flow, causing material hardening and embrittlement [88]. Therefore, their reduction or removal is key to radiation damage resistance. For these reasons, the interaction of SFTs with various types of pristine GBs has been simulated [105–107], and the ability to remove SFTs depends on the GB's structural characteristics. Despite the successes of previous atomistic simulations, the detailed mechanisms of SFT interaction with GBs as a function of irradiation dose and their mechanisms for damage reduction in NC materials remain elusive, because the microscopic structures of the GBs themselves are constantly changing under irradiation.

Essentially, the way in which defects interact with irradiated GBs is different from that with pristine GBs and interfaces [49,100]. For a comprehensive understanding of damage reduction and the enhanced radiation-tolerance in NC materials, a consecutive displacement cascade algorithm is developed to perform atomistic simulations of prolonged radiation damage in NC-Cu, a system that has been widely used in irradiation studies [21,70,91,94,101]. The aims of this work are to understand (1)

radiation-induced defect evolution with increasing damage dose, particularly defect cluster nucleation, migration and aggregation in the presence of GBs, (2) the mechanisms and processes for SFT annihilation, and (3) how radiation-induced defect density depends on grain size.

3.2.2 Computational models and methods

This work focuses on two representative high-angle $\Sigma 5(210)$ and $\Sigma 5(310)$ symmetrical tilt GBs in Cu, modeled by an embedded-atom method (EAM) potential developed by Mishin et al. [108]. Figure 3-11(a) shows the simulation model, with periodic boundary conditions applied in all three directions. The GBs in the simulation cell are separated by a spacing λ. The lengths of the simulation box along $X-$, $Y-$ and $Z-$directions are $2\lambda \times 11.4$ nm $\times 10.9$ nm, with a series of λs ranging from 5.7 nm to 28.5 nm and atoms from 117,600 to 588,000 considered. The GB is built by joining two perfect crystals along the (210) or (310) planes followed by static energy minimization. A number of configurations are sampled by varying the relative positions of the two crystals and removing atoms within a cutoff distance which is varied to obtain equilibrium state. The stable structure with the lowest potential energy is chosen for this study. Figure 3-11(b) and (c) show the equilibrium structures of the two symmetrical boundaries $\Sigma 5(210)$ and $\Sigma 5(310)$, respectively. It highlights the structural units [109] to illustrate the boundary characteristics, where both GBs appear to be composed of kite-shaped units [103, 110, 111]. Atoms are color-coded according to their volumetric value calculated by Voronoi analysis [112]. It is worth noting that atoms in the GBs indicate larger free volume than those in the bulk, implying potential sites for accommodating interstitials.

To reach a high damage dose and reveal defects evolution during irradiation, the same methodology is used as in Chapter 3.1 in the molecular dynamics (MD) method as implemented in LAMMPS [113]. The Ziegler-Biersack-Littmark (ZBL) repulsive potential [69, 70] is smoothly joined to the aforementioned EAM potential [21] to deal with high energy atom collisions, and an adaptive time step algorithm is used to limit atomic movement to 0.05 Å per timestep. Before the collision cascade simulation,
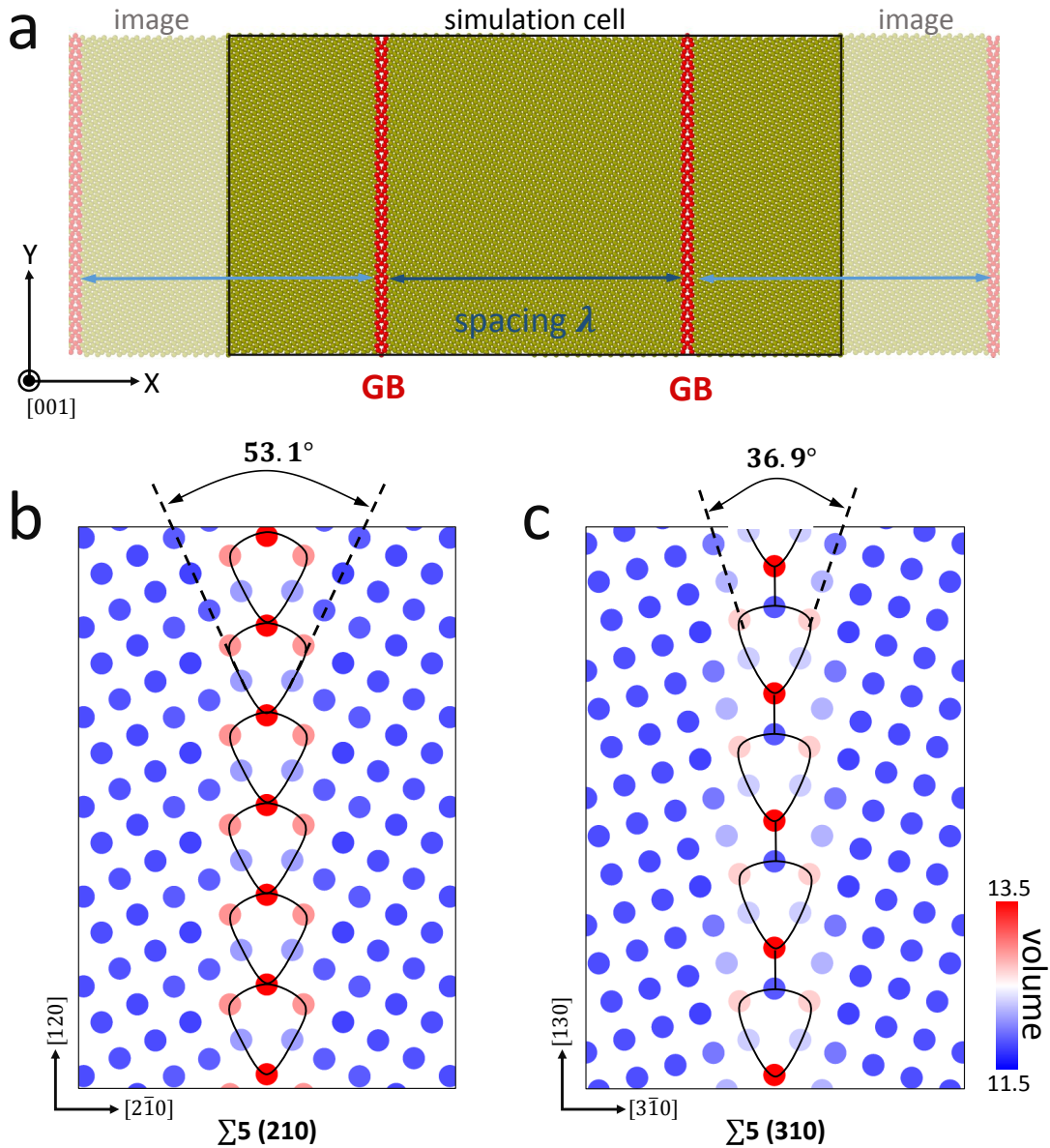
Figure 3-11: (a) Illustration of the simulation model used in this study. Brown atoms have a FCC structure, while GB atoms are shown in red. Periodic boundary conditions are applied in all three directions, with periodicity along the x-direction plotted to show GBs separated by a spacing λ. (b-c) GB structures and atomic volume. The GBs structures of $\Sigma5(210)$ (b) and $\Sigma5(310)$ (c) are viewed along the [001] axis. The kite-shaped units are marked to illustrate the GB structures, where atoms are colored by the volume of their Voronoi cells. The misorientation angle is defined by the [100] direction of the two crystals.

the system is relaxed to zero pressure at 300K for 100 ps. Then, an algorithm is developed to consecutively introduce 5 keV damage cascades into the system randomly. A damage level of ~ 0.27 dpa (250 to 1,250 cascades depending on system size) is achieved according to the NRT approximation i.e. $n \times E_{\mathrm{pka}}/2E_{\mathrm{d}}$, where n is number of cascades, E_{pka} is the PKA energy and E_{d} represents atom displacement threshold energy [11]. The short simulation time (an inherent limitation of MD) between collision cascades yields a dose rate several orders of magnitude higher than that in experiments. Although the difference in dose rate between MD and experiments is quite large, recent studies using similar simulation approaches have shown good agreement with experiments [4]. It should be noted that the chosen incident energy 5 keV is one representative value from common PKA spectrum in irradiation experiments [114]. This energy enables a reasonable simulation cell to reach a damage level comparable to experiments, and allows studying defect evolution and diffusion processes and the underlying SFT annealing mechanisms with the presence of GBs.

To uncover defects nucleation and evolution after each displacement cascade, the adaptive common neighbor analysis (a-CNA) [74] and Wigner-Seitz cell method [70] are utilized to identify defective structures and defect types in OVITO package [115] . Specifically, the evolution of interstitial and vacancy is analyzed by comparing the series of irradiated systems with the initial perfect structure. All data files supporting the findings of this study are available on a public data repository [116].

3.2.3   Results

3.2.3.1   Dynamic evolution of defects during irradiation

The results of radiation-induced damage in Cu with $\Sigma5(210)$ GBs are presented in Figure 3-12, where defective structures (non-FCC atoms) are shown at various doses. Similar results and defect evolution are found for $\Sigma5(310)$ GBs. At a low damage level of 0.001 dpa, one can see in Figure 3-12(a) the production of points defects and small clusters, which cause the left-hand GB to wiggle due to its preferential absorption of interstitials. This preferential uptake of interstitials by GBs results in a biased defect
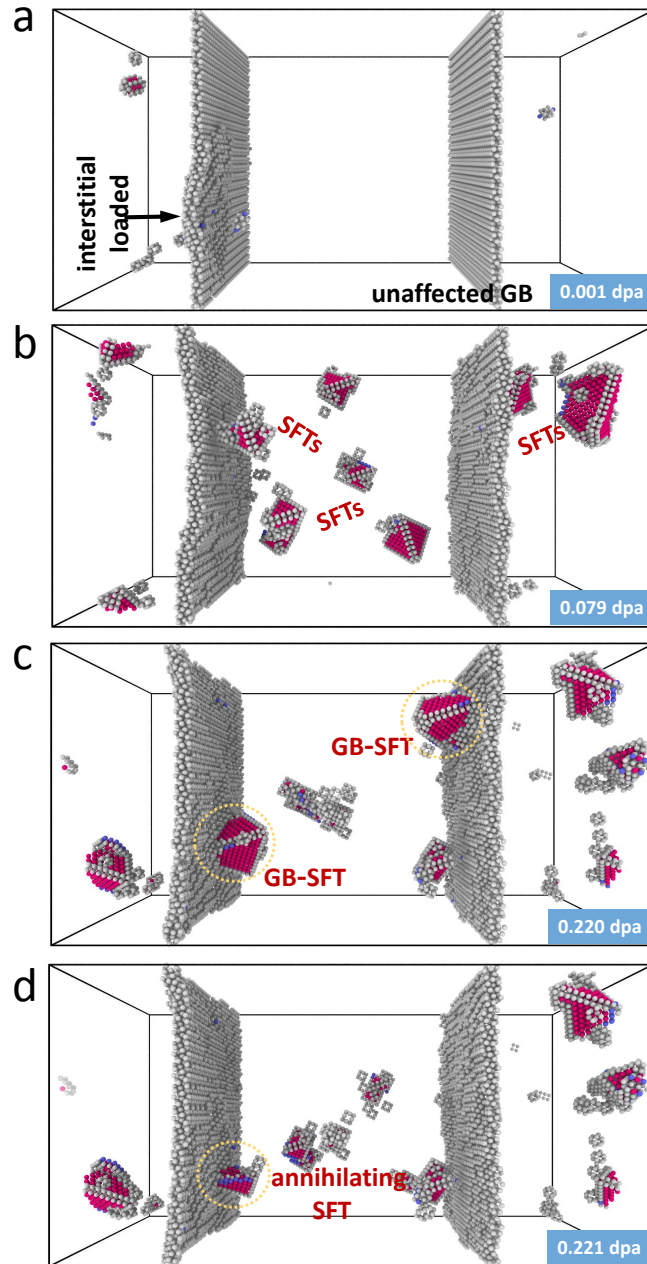
Figure 3-12: Radiation-induced defect clusters and GB evolution in $\Sigma 5(210)$ Cu at different doses. The grain spacing λ is 11.4 nm. Atoms are color coded according to their structures (red $\rightarrow$ HCP, blue $\rightarrow$ BCC, grey $\rightarrow$ other structure, FCC atoms not shown). For the sake of clarity, only the ten largest defects are shown in the figures. (a) shows the point defects and interstitial-loaded GB produced at a low radiation dose of 0.001 dpa (two collision cascades at 5 keV). (b) displays the irradiated GBs and radiation-induced SFTs at 0.079 dpa. (c-d) indicate that SFTs do not appear to grow in size and number at higher doses, as they are observed to be interacting with GBs. The SFTs are annihilated via the GB-SFT interaction. Abbreviations are as follows: FCC, face centered cubic; HCP, hexagonal close packed; BCC, body centered cubic; GB, grain boundary; SFTs, stacking fault tetrahedra.
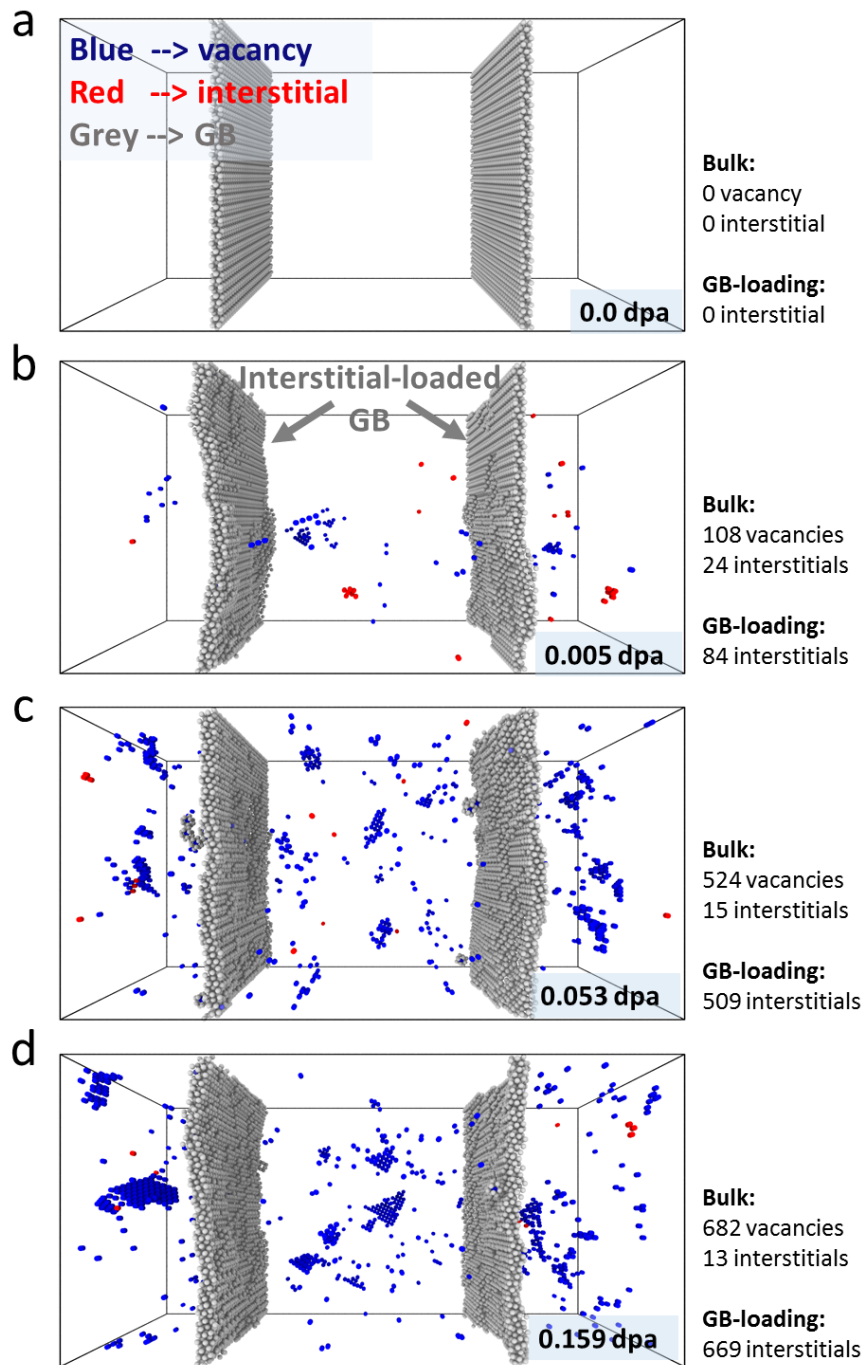
Figure 3-13: (a)-(d) Distributions of vacancy and interstitial at various doses in $\Sigma 5(210)$ system with spacing 11.4 nm. Grey atoms represent GBs, while blue and red are vacancy and interstitials, respectively. The GBs absorb most radiation-induced interstitials, becoming interstitial-loaded and leaving vacancy-rich bulk regions. The interstitials and vacancies are identified by Wigner-Seitz cell method.

distribution, with a vacancy-rich bulk and interstitial-loaded boundary region (Figure 3-13). As the damage level increases, small defects are continuously produced and the interstitials further gather in the boundary region. The GBs in Figure 3-12(b) can be regarded as highly irradiated, which appear thicker compared with pristine ones. They are observed to be more active to dynamically interact with the surrounding defect clusters such as SFTs which are formed through collision cascades or vacancy aggregation. These SFTs preferentially diffuse towards GBs and interact with them as shown in Figure 3-12(c), eventually being removed in Figure 3-12(d). At the high damage level of 0.221 dpa, there is not a clear increase in SFTs compared with 0.079 dpa, implying that the defect density may have saturated (see discussion of Figure 3-14). During irradiation, GBs are observed to oscillate, sweeping up nearby defects, and this phenomenon further contributes to the damage reduction.

The total number of defective atoms (non-FCC) induced by radiation as a function of damage dose is shown in Figure 3-14(a). The defect number rapidly increases with doses up to about 0.08 dpa, and after that the defect production rate markedly slows, approaching saturation. Both GB types show essentially the same defect accumulation behavior, while $\Sigma5(210)$ has a slightly lower saturated defect density than that of $\Sigma5(310)$, which could be attributed to the extra free volume (Figure 3-11(b)) and higher energy of $\Sigma5(210)$ [117]. A similar two-stage process has been observed for the behavior of SFTs in Figure 3-14(b). However, the SFT saturation appears to reach a slightly higher dose as compared with that for total defective atoms, because the system requires extra time to rearrange the vacancy defects into SFTs. After about 0.1 dpa, the number of SFTs starts to fluctuate with a characteristic zigzag shape, suggesting a dynamic equilibrium between SFT creation and annihilation.

3.2.3.2 Mechanisms of SFT annihilation

Atomistic mechanisms underlying the removal of SFTs constitute one key to understanding the enhanced damage-tolerance of NC metals. It should be noted the following results are described for $\Sigma5(210)$, whereas the same behavior is also present in $\Sigma5(310)$. The formation of SFTs during irradiation is mainly caused by defect aggre-
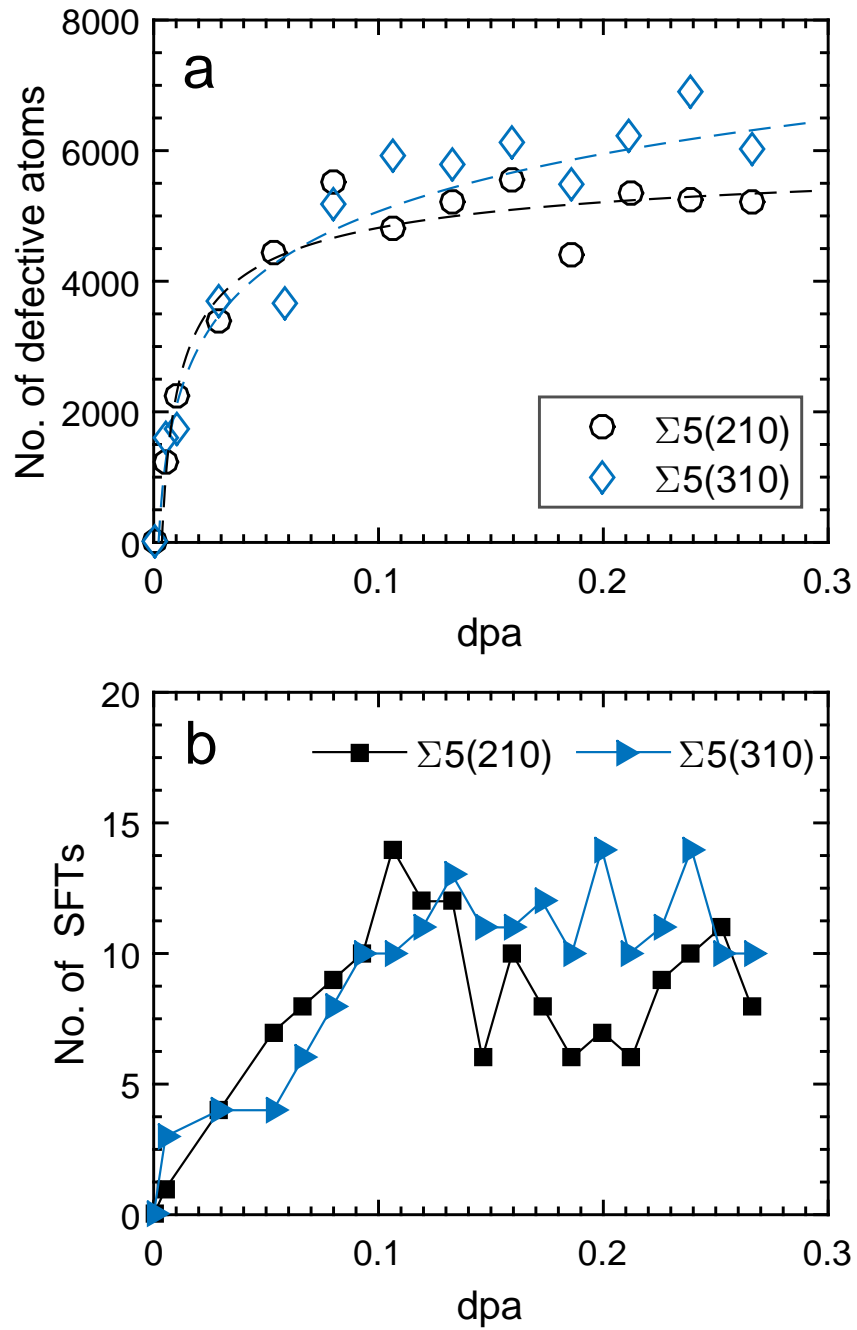
Figure 3-14: (a) Total number of defective (non-FCC) atoms as a function of dose in Σ5(210) and Σ5(210) systems. The dashed-lines are shown to guide the reader. (b) Number of large SFTs (clusters containing more than 15 vacancies) versus dose.
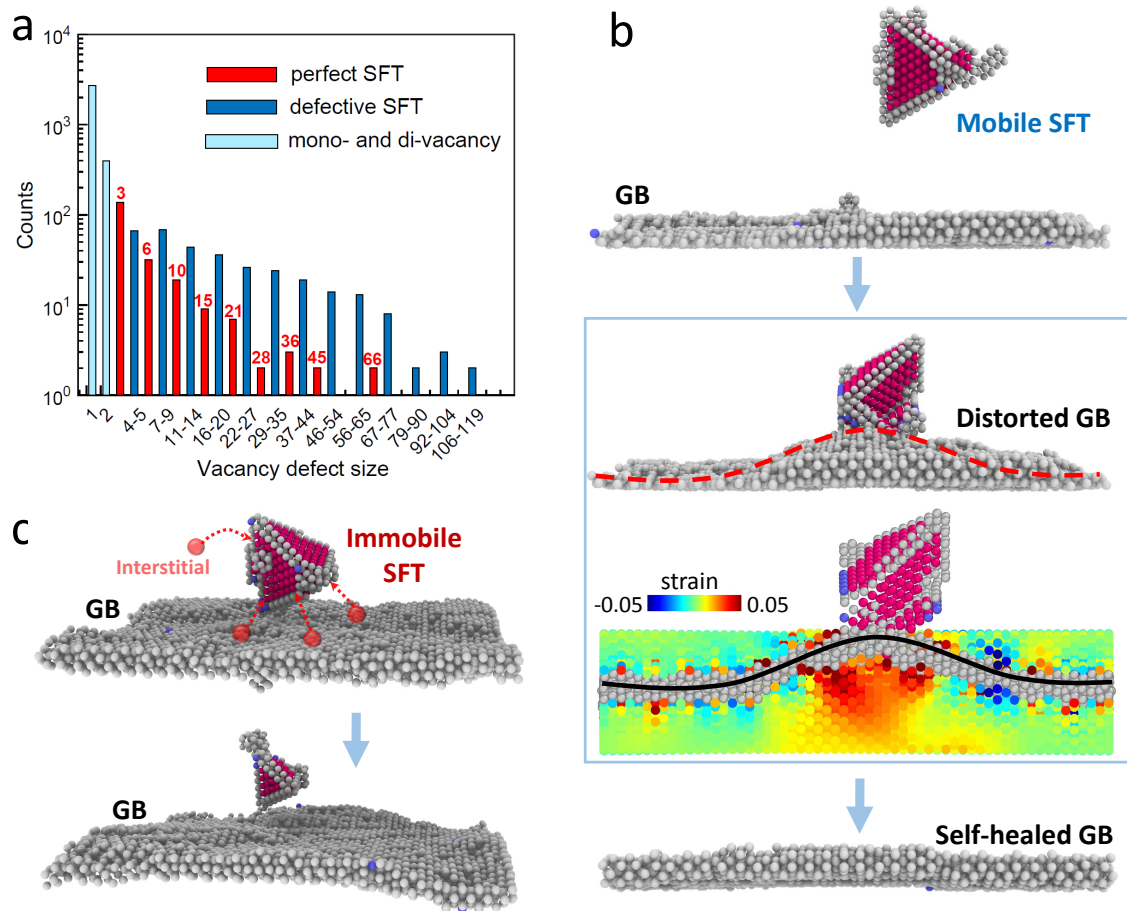
Figure 3-15: (a) Statistical distribution of vacancy-type defect sizes in irradiated $\Sigma 5(210)$ Cu with grain spacing of 11.4 nm at damage dose from 0.01 dpa to 0.27 dpa. Mono- and di-vacancies, defective SFTs, and perfect SFTs are grouped and shown according to their sizes (number of vacancies). (b) SFT annihilation process via interaction with a GB. A radiation-induced SFT (upper panel) migrates to a GB, which becomes locally distorted upon contact (middle panel). A cross-sectional view is also provided where neighboring atoms of the GB are colored by atomic strain. Finally, the SFT is absorbed, returning the distorted GB to a straight profile (bottom panel). (c) shows the process of SFT annihilation by interstitial recombination. An immobile SFT shrinks in size due to absorbing interstitials resulting from GB emission and nearby cascades.

gation and vacancy-void self-reorganization [118]. SFTs are commonly known to be immobile and stable, with their energetic stability increasing with their size [119,120]. In a recent study, it was found contrary to common belief that defective SFTs are quite mobile, and their diffusivities can be even higher than that of mono-vacancies [121]. Thus the population of different types of SFTs produced under irradiation can be significant to understand the radiation resistance and performance of NC-Cu. Figure 3-15(a) shows the size distributions of SFTs formed during irradiation, where the size of each is measured using Wigner-Seitz cell method by the number of constituent vacancies [70]. All the defects have been grouped into three categories: perfect SFTs, defective SFTs, and mono- and di-vacancies, where the sizes of perfect SFTs are so-called magic numbers [118]. More than 82% of the SFTs are found to be defective in the irradiated systems, and their diffusivities, depending on the size, are several orders of magnitude higher than those of the perfect SFTs [121]. The strong heterogeneity of the SFT diffusion is significant in damage reduction.

By probing the atomistic processes of defect evolution, two typical SFT annihilation modes are identified, i.e. removal by GBs and elimination through interstitial recombination. Their occurrence depends on the corresponding SFT mobility. Since most SFTs are defective and mobile, GB removal is found to be the major mechanism for SFT annihilation in NC-Cu. Figure 3-15(b) illustrates such a process of removing an SFT via interaction with a GB. A mobile SFT is formed 4.5 nm away from the boundary, which at first appears to be straight. After a short time, the SFT quickly migrates towards this interstitial-loaded GB, while the GB atoms rearrange themselves to accommodate the incoming SFT. In the middle panel of Figure 3-15(b), one can see that the distorted GB and the SFT are in direct contact, suggesting an attractive interaction between the irradiated-GB and the SFT. In the meantime, a tensile strain field develops just below the distorted GB. Following SFT annihilation, the GB once again becomes straight in appearance, revealing a resilient, self-healing response to radiation damage [93]. It is expected that the interstitial-loaded GBs will reduce the defect diffusion barrier, allowing interstitials to migrate readily to redistribute themselves along the GB region to facilitate the GB-SFT interaction. The

SFT migration during irradiation is not purely random, but shows some bias towards the GBs. This biased SFT diffusion implies attractive forces between interstitial-load GBs and SFTs. Such preferential drift of radiation defects towards GBs and subsequent self-healing interactions lead to radiation damage reduction, with a similar mechanism observed in the interaction between point defects and interfaces [122].

The second annihilation mechanism of interstitial recombination mostly occurs in less mobile clusters, such as perfect SFTs whose diffusivities can be several orders of magnitude lower than that of defective ones. Figure 3-15(c) illustrates the annihilation process, where a nearly perfect SFT appears some distance from a GB. In this case, the SFT and GB are not directly connected, yet the SFT still decreases in size (bottom panel of Figure 3-15(c)) and eventually disappears. The detailed processes of immobile SFT annihilation is provided in 3-16. This SFT elimination signifies interstitial absorption, which could arise from the surrounding bulk region and GB emission. Even though nearly 18% of the SFTs in the simulations are perfect, their structures can be disrupted by adjacent collision cascades or by incoming defects, and conceivably some of them turn into defective ones with high mobilities. The possible perfect-defective transformation facilitates SFTs reaching GBs, and ultimately annihilation via GB-SFT interaction.

3.2.3.3   GB size-dependent defect density

It has been reported in experiments that NC materials with smaller grain sizes have higher tolerance to radiation in comparison with large grained materials [123], which sparks the curiosity to study the correlation between grain size and defect density. All defects produced by radiation damage are extracted and their size distributions in the irradiated systems with grain spacings of $\lambda = 5.7$ nm, 17.1 nm, 28.4 nm are shown in Figure 3-17(a). It can be seen that the system with the smallest λ of 5.7 nm has no defect cluster larger than 500 atoms, whereas in the large λ systems many large clusters appear. The correlation between defect cluster density and λ is shown in Figure 3-17(b). The density shows small variation with decreasing λ down to 11.4 nm, below which there is a clear reduction in density at the smallest λ of 5.7
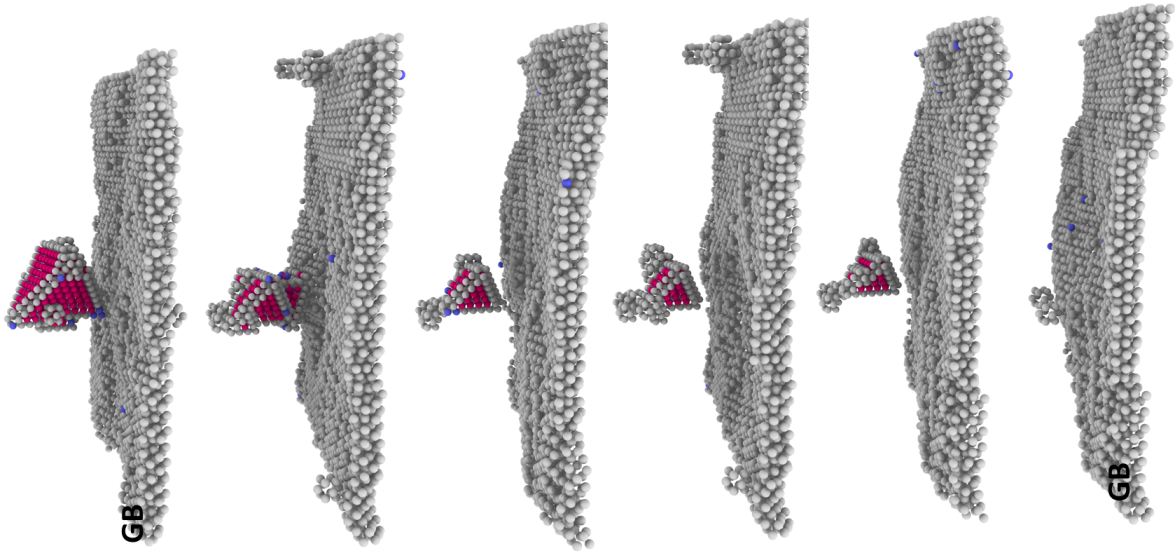
Figure 3-16: Processes of immobile SFT annihilation. The size of the SFT decreases by absorbing interstitials.
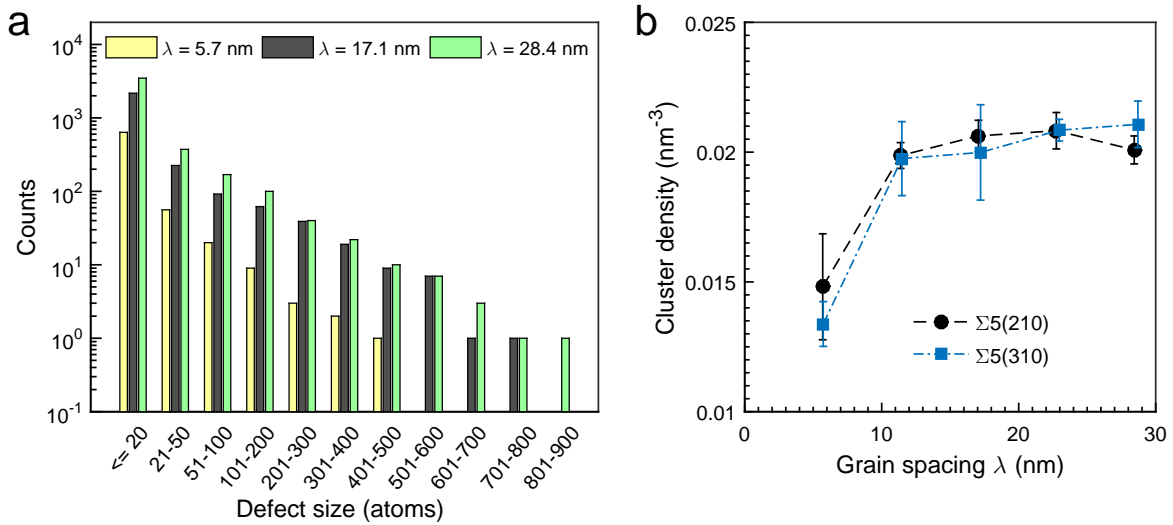
Figure 3-17: (a) Statistic distributions of defect size for different $\Sigma 5(210)$ spacing λ. Three independent simulations are performed for each grain spacing λ, and all defects produced at damage dose from 0.01 dpa to 0.27 dpa are extracted. (b) The density of defect cluster (with size > 1) as a function of λ for both $\Sigma 5(210)$ and $\Sigma 5(310)$ systems.

nm. A similar value of 8 nm was reported in recent experiments of nanotwinned Ag by Yu et al. [97], at which the defect density is significantly reduced. Although close agreement is obtained between the simulations and the experiments, it is worth noting that defect annihilation in NC materials is a complex process, dependent on the material, radiation-induced defect type, GB structure, and dose rate [124–126], all of which can influence the defect-sink performance of a GB.

Figure 3-18(a-b) show the distributions of defect clusters in $\Sigma 5(210)$ systems irradiated to 0.27 dpa with grain spacings of 22.9 nm and 11.4 nm, respectively. One can see that a number of large clusters are formed in the bulk region away from the GB. The drastic defect reduction at small grain spacing of 5.7 nm in Figure 3-17(b) suggests a synergistic effect on damage reduction, more effective than the sum of two individual GBs. The synergistic effect can be interpreted by Figure 3-18(c) which depicts two GBs operating synchronously and cooperatively to interact with a large SFT. This explains the irradiated system maintaining only few small-size defects (see Figure 3-18(d)). It should be noted that similar behaviors are consistently observed in $\Sigma 5(310)$ systems with corresponding spacing. The results suggest an approach to improving material radiation tolerance by optimizing grain size from the standpoint of this synergistic effect.

3.2.4 Discussion

In this work, the detailed, atomistic evolution of radiation-induced defects in NC-Cu is presented with increasing dose up to 0.27 dpa. The defect density variation with dose is found to consist of two stages, an initial stage of rapid density rise, followed by a saturation stage at which defect creation and annihilation are approximately in balance. GBs preferentially absorb interstitials, as has been seen in previous studies, leaving behind a vacancy-rich bulk region. SFTs formed via the vacancy coalesce and cluster rearrangement would retard the motion of dislocations in mechanical deformation, and be responsible for radiation-induced hardening. The interstitial-loaded GBs are mobile, fluctuating and strongly interacting with the surrounding defects, thereby the motion of defective GBs further enhances the absorption of defects.
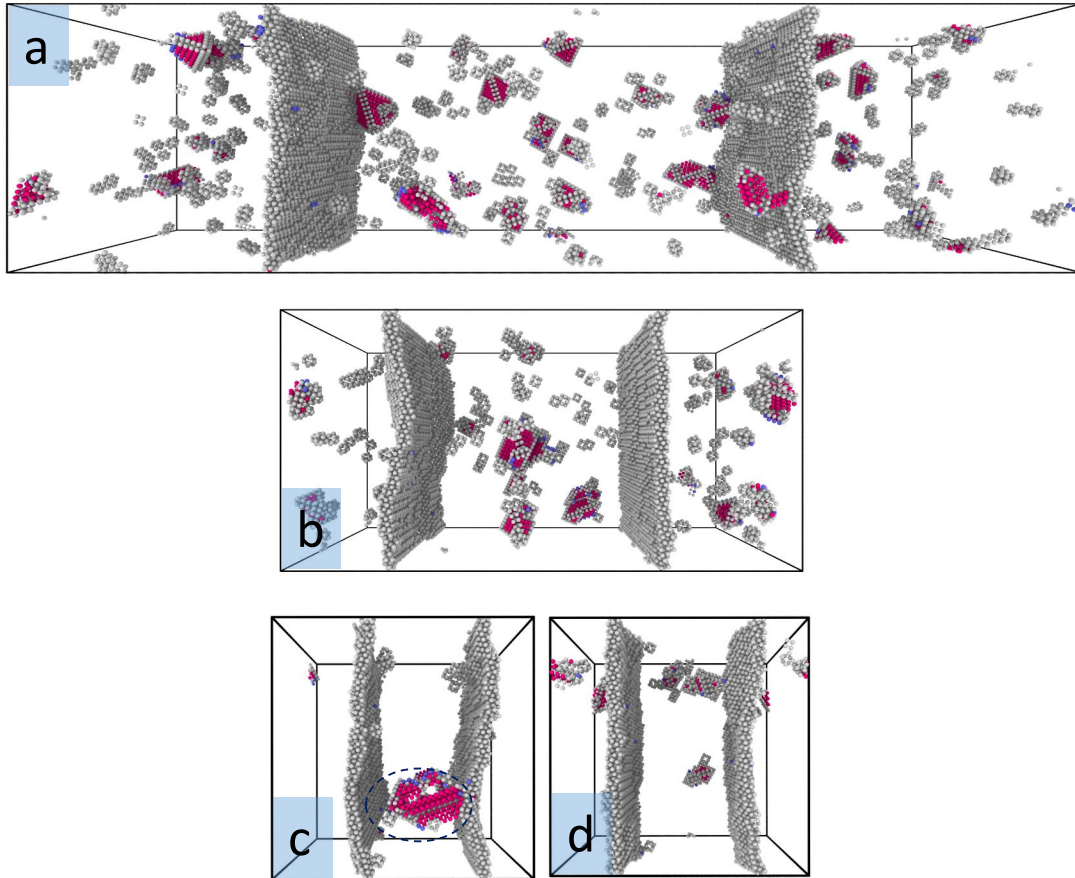
Figure 3-18: (a) and (b) spatial distributions of defect clusters in irradiated $\Sigma 5(210)$ systems at 0.27 dpa with λ values of 22.9 nm and 11.4 nm, respectively. (c) Two GBs simultaneously interact with a large SFT at a small λ of 5.7 nm. Small defects are the primary forms of damage (d).

The simulations reveal two characteristic mechanisms involved in SFT annihilation. The interaction between interstitial-rich GBs and defective SFTs is the dominant and efficient process for SFT removal, while interstitial recombination appears to contribute more to annihilate immobile, perfect SFTs. The GBs are dynamically resilient during their interaction with defect clusters. In response to the incoming SFTs, the GBs distort their structure and recover after absorbing SFTs in a self-healing manner. It is worth noting that SFTs can also be annealed via interaction with low-angle and irradiated coherent twin boundaries [92]. While the detailed process could depend on specific boundary characteristics, the effects of GB on defect removal and radiation-resistance appear to be quite general. The SFT annihilation-enhanced radiation resistance can also be applied to other FCC metals such as Ag, Ni and Au, which feature SFTs as the predominant defect type under irradiation. However, due to a high stacking fault energy, Al does not form SFTs under irradiation [104] and its specific damage reduction mechanisms require future investigation.

The diffusion of SFTs near GBs exhibits non-random walk migration characteristics, showing a drift towards the boundary. This directional diffusion suggests an attractive force exerted on the SFTs by interstitial-rich GBs, essentially the same as the elastic interaction between point defects and material interfaces [122]. The drastic defect density reduction at a small grain spacing of 5.7 nm signifies the synergistic effects of GBs on defect annihilation, leading to the interpretation of improved radiation damage tolerance in NC materials compared with their coarse-grain counterparts. On the other hand, small grains suffer from rapid radiation-induced growth, so that the overall radiation effects and structural impact may be governed by the competition between efficient defect annealing and simultaneous grain growth. Manipulating the GBs through segregating dopants [127] provides a potential path to stabilize the boundary structure and defer the rate of grain growth. The radiation-induced grain growth is not captured by current simulations due to the low GB mobility at low temperature and short MD timescale. It should be noted that grain growth has been frequently reported for irradiated nanocrystalline materials, and a thermal spikes model was proposed by Kaoumi et al. [128].

These results provide mechanistic insights regarding damage reduction in NC metals, and have important implications for designing and optimizing radiation-resistant nanostructural materials. The observed sharp change of defect density by varying grain spacing represents design guidance on grain size of Cu, and other FCC metals with low stacking fault energies, subject to irradiation. This observation likely illustrates a general trend in other materials, though the optimal size will depend on the material type, GB characteristics, and other competing effects such as grain growth. These results also motivate investigating the processes and mechanisms of radiation damage reduction in nanocomposites, such as metal-carbon nanotube composites [129], nanolaminates [130] and oxide dispersion strengthened materials [131].

Although increasing GB area by refining grains can significantly reduce damage accumulation in materials, the structural stability can be undermined due to the high grain boundary energy which constitutes a strong driving force to grain growth. The increase of grain size may degrade the mechanical strength, and such process can be largely accelerated by radiation, which will be detailed in next section.

3.3 Radiation-induced grain growth in nanocrytalline metals

Although nanocrystalline materials have demonstrated high radiation resistance, one of the concerns is radiation-enhanced grain growth, which increases the grain sizes and degrades the mechanical strength. However, the GB behavior actuated by radiation hasn't been fully elucidated. This study aims to provide detailed process and mechanistic understanding of radiation-induced GB migration and grain growth in the nanocrystalline Cu.

Declaration: This section mainly cites from my published work in [132], with permission from the publisher.

3.3.1 Introduction

Internal interfaces such as grain boundaries (GBs) play a central role in governing many material properties in metals. For example, decreasing grain size to the nanometer scale, which increases the volume density of GBs, considerably improves mechanical strength [133]. Microstructural evolution due to grain growth is controlled by a key process - GB migration. The growth of one grain at the expense of others can be driven by various forces, from elastic energy anisotropy, non-uniform defect or impurity density, a gradient in temperature, and capillary forces of the curved GBs [134]. These driving forces are frequently considered in experiments and simulations to study GB migration and growth in a variety of polycrystalline systems [135–137].

When the materials are subject to irradiation, the interface acts as an effective defect sink by annealing radiation-induced defects. In this sense, nanocrystalline (NC) metals with a high volume density of boundaries may be promising candidates for radiation-tolerant structural materials [49], but they are known to undergo radiation-induced grain growth at either low or elevated temperatures. In the studies of irradiated polycrystalline thin films, the average grain size increases with irradiation dose in a power law relationship with a power exponent depending on the microstructural

characteristics, material type, temperature, and irradiation condition [138,139]. The-oretical models based on thermal spikes at GBs were proposed to interpret the nature of radiation-induced grain growth [128, 140], in which GB is hypothesized to migrate through biased atomic diffusion; the process occurs within the displacement cascade (i.e. thermal spike) region in the vicinity of GB and is driven by local GB curva-ture. The curvature-assisted GB motion has also been observed in MD simulation of displacement cascades in nanocrystalline metals, but only arises if the thermal spike exceeds the grain size and overlaps GB [141]. By varying the irradiation temperatures on Zr, Pt, Cu, and Au NC thin films, Kaoumi et al. [142] suggested that there exists thermal and athermal regimes where thermal diffusion of defects or irradiation spikes dominates, and the transition temperature between the two regimes depends on the material properties. Although the aforementioned experiments and simulations on polycrystalline materials construct a picture of overall change in grain size, it's nearly impossible to extract a clear understanding of a specific type of GB's response to radiation damage due to the complexity of microstructures which contain a variety of connected GBs and the limitation in experimental temporal and spatial resolution.

Bicrystal system is a reasonable alternative to study the properties of individual boundaries. To prompt boundary motion, external driven forces are typically applied to the system. external forces are typically applied to the system, including shear stress [143], elastic stored energy [144], vacancy loading [145] and artificial synthetic forces [117]. These have been considered in both experiments and simulations. The resultant GB migration rates were found to be proportional to the magnitude of each force. Without external forces or internal energy gradients, planar GBs generally exhibit random-walk migration [146]. How they evolve under irradiation is an open and interesting scientific question, which is of central importance to understanding radiation-induced grain growth.

In this work, the mechanisms that govern GB migration and grain growth in NC metals during ion irradiation are explained. Meanwhile, the detailed behavior of the high angle GBs in NC Cu under irradiation and how the simulation results relate with grain growth are carefully examined. In contrast with previous studies where a single

cascade is initiated in the system [103, 141], this study elaborate the accumulating consequences by continuously introducing primary-knock-on atom (PKA) into the simulation box. The GB behavior revealed under such condition comes from the interplay of multiple processes including recrystallisation of the thermal spikes, GB preferential absorption of interstitials, interaction between SFTs and GBs, and short-range GB interaction.

3.3.2   Methods

A Cu bicrystal with representative high-angle, high-energy $\Sigma5(210)$ symmetrical tilt GBs is studied. The structure consists of an array of kite-shaped structural units by joining two perfect crystals along (210) planes, followed by static energy minimization. A schematic view of the simulation model is provided in Figure 3-19(a), with periodic boundary condition applied in each direction. The two GBs are separated by a distance λ, and the size of the simulation box is then $2\lambda \times 11.4\ nm \times 10.9\ nm$. Two spacings, i.e. $5.7\ nm$ and $11.3\ nm$ are analyzed to explore grain the size effect. Figure 3-19(b) shows atomic arrangement of the GB, colored by atomic volume identified by Voronoi method.
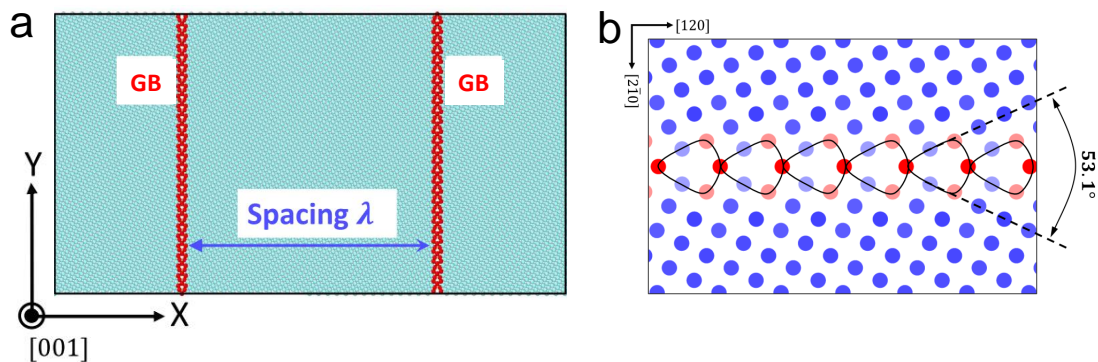
Figure 3-19: (a) shows the simulation cell with periodicity in each direction. Two values of spacing λ are studied. (b) plots the $\Sigma5(210)$ GB atomic arrangement. Atoms are colored by per-atom volume identified by Voronoi method after performing minimization to show the extra volume inside the GB.

The Cu-Cu interaction using the embedded-atom method (EAM) potential which is smoothly joined to the Ziegler-Biersack-Littmark (ZBL) repulsion to resolve highly

energetic collisions. The system is firstly equilibrated to a zero pressure for 100 ps and followed by cascade simulation using the same procedure as described in [79]. Randomly selected PKAs (primary knock-on atoms) are consecutively introduced into the simulation cell with a kinetic energy of 5 keV, where each cascade lasts around 28.8 ps. The system is fully annealed to ambient temperature before another PKA is introduced. It should be noted that this procedure inevitably leads to a much higher dose rate comparing with experiments, nevertheless, investigation can still generate meaningful results when microsctruture evolution is driven by high energy density cascades rather than the longer time scale thermal diffusion. Using the atomic configurations generated from MD simulations, GBs and defective structures are monitored throughout the irradiation process by common neighbor analysis. Visualization is based on the OVITO package [115].

3.3.3   Results

3.3.3.1   GB migration

The position of both GBs is monitored throughout the simulation process. Specifically, the GB position is calculated by averaging the x-coordinate of all constitute atoms based on common neighbor analysis. Figure 3-20(b) plots the GB x-position as a function of time for system with ambient temperature 800 K and initial spacing 11.3 nm, where at time $t = 0$ ns the initial GB 1 and 2 are located symmetrically with respect to $x = 0$. The two GBs show a general trend of approaching each other, and end up with direct contact and rapid disappearance, as an indication of grain growth. On the other hand, zooming in the position-time profile reveals two features of the migration pattern: i) the movement is conducted in a temporally intermittent manner, i.e. small gradual shift inter-weaved with abrupt change; ii) 'back and forth' oscillation resides in the global trend of closing in. Such fluctuation reflects a biased migration and local adjustment of GBs due to the influence of thermal spikes and interaction with defects. Correspondingly, Figure 3-20(c) shows the system potential energy change (δE) at the end of each cascade. The residual defects from damage
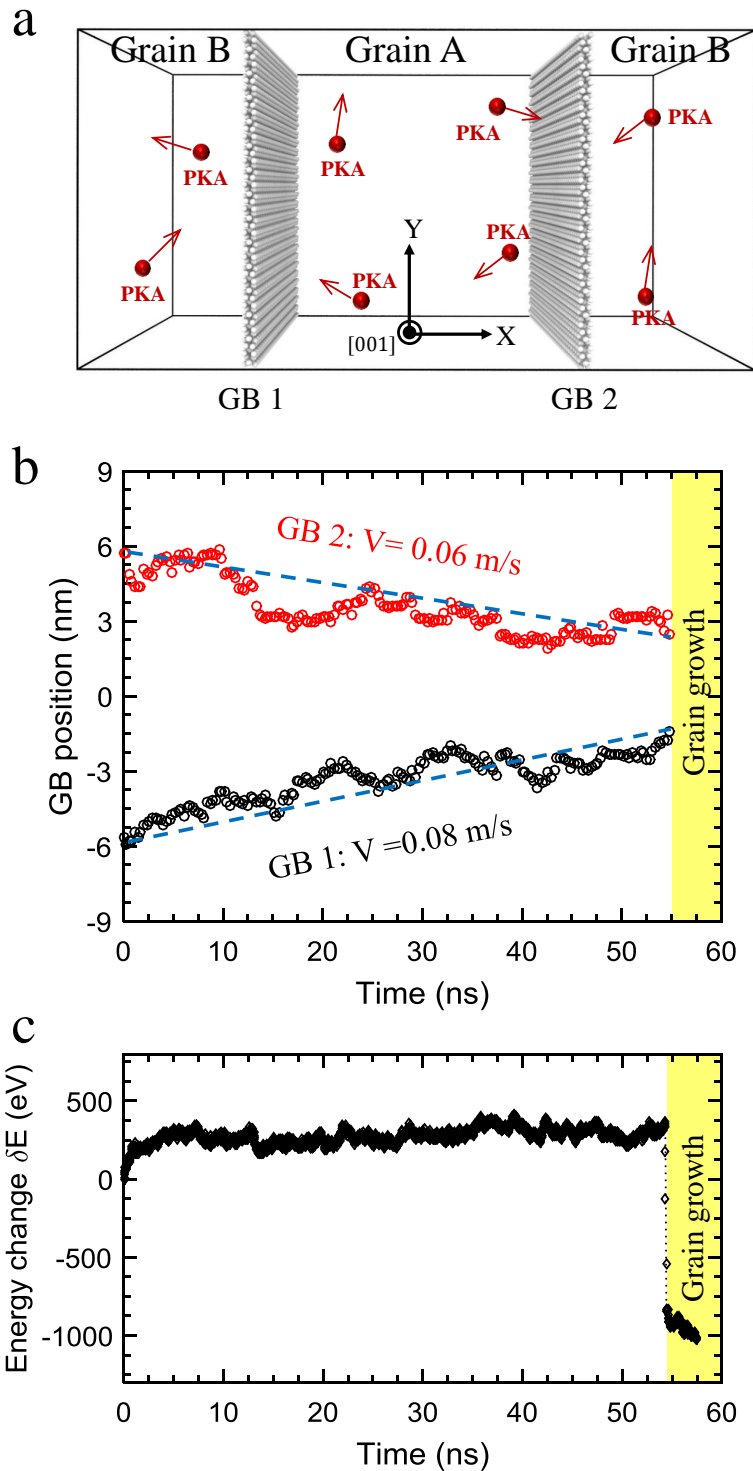
Figure 3-20: (a) shows the simulation cell with periodicity in each direction. GB spacing of 11.3 nm is used. PKAs are randomly selected atoms with 5 keV kinetic energy. (b) plots the GB position during the irradiation process. (c) shows the potential energy change corresponding to (b).

89

cascades introduce extra energy into the system. Small jitters in the profile are an indication of defect production and defect-GB interaction. Note that δE stays around the same level before final merge and a closer examination reveals that the interaction between the two GBs is negligible, which means the approaching trend in the long run is not attributed to any attraction between GBs.

Figure 3-21(a) shows the histograms of atom count at each damage level, by binning GB constituent atoms along horizontal direction. It can seen that the GBs approach closer in the long run (Δ), and ultimately annihilate. The spread widens as GBs becomes highly loaded with interstitials. In addition, the local distortion of GB also contributes to the spread. The profile of GBs can be significantly influenced by thermal spikes and nearby SFTs. Note that the removal of SFTs at GB is very efficient and a subsequent self-healing of GB to become straight are frequently observed. This resilient and restoring feature of GBs are also be inferred from occasional decreasing spread during the irradiation process. Figure 3-21(b) demonstrates the GB movement with $\lambda - \Delta$, where λ takes 5.7 and 11.3 nm. The migration of GBs is weakly influenced by the initial spacing. With λ=5.7 nm, as GB distance drops, large SFTs simultaneously interacting with both GBs contribute to the tendency of further approaching. In comparison, GBs with $\lambda = 11.3$ nm are still beyond the range of such type of interaction, hence they can readily retrogress. With reasonable values of Δ ($\gtrsim$ 5 nm), one may abstract the motion of GB disturbed by irradiation as random walk. It ultimately leads to a close separation where concurrent SFT-GBs interaction starts to play a role in drawing both GB closer. The mean position of GB drifts slowly from the initial location, and a large deviation becomes increasingly less probable. It follows that GB annihilation requires much longer time with a large λ.

As Δ shrinks to some point, the annihilation of GBs become very efficient, which implies a critical distance may exist, with a sharp increase in the probability of GB short-range interaction. To validate this point, multiple simulations are run for λ=5.7 nm and Δ is tracked until the rapid GB annihilation. Figure 3-21(c) demonstrates the results of five independent cases with an ambient temperature of 800 K, which is intentionally raised to accelerate the process. Examining the evolution process, one

90

can see that as the distance between two planar GBs slowly shrinks to a small value around 4 nm indicated by the shaded band, the annihilation of GBs become very efficient, as large SFTs in between attracting both GBs, combined with additional perturbation from thermal spikes can effectively trigger the grain growth.
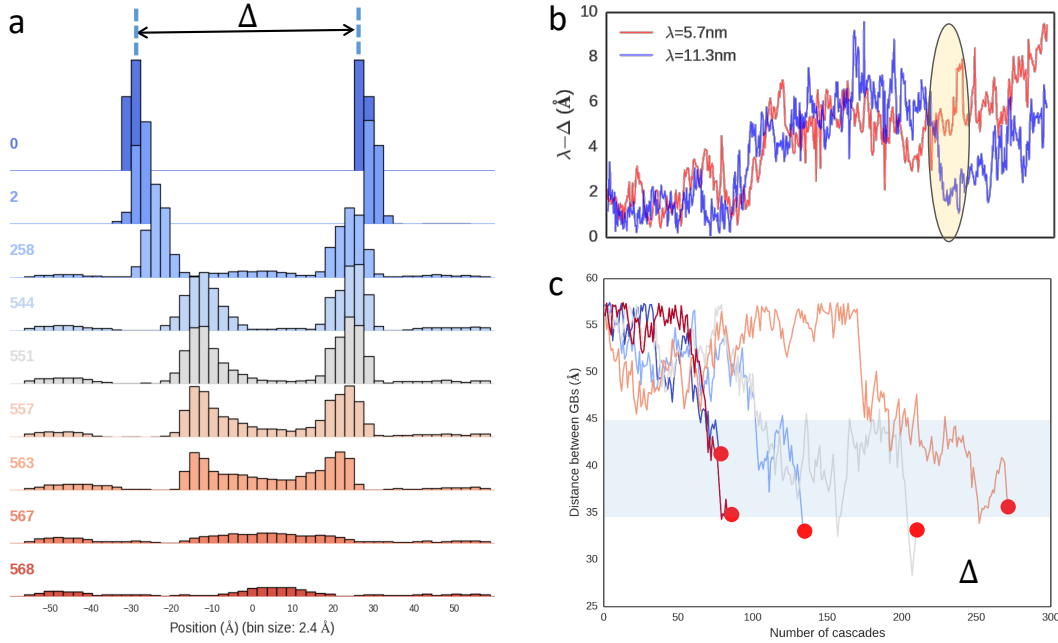
Figure 3-21: (a) Evolution of the distribution of non-FCC atoms along the horizontal axis at various damage level indicated by the number of cascades on the left (T=300 K and λ=5.7 nm); (b) The change in GB distance ($\lambda - \Delta$) for λ=5.7/11.3 nm at T=800 K with increasing dose level. (c) Multiple simulations on GB evolution prior to annihilation at 800 K and λ=5.7 nm, where the red dots indicate the start of rapid GB elimination. The shaded band illustrates a critical interval where GBs are very prone to annihilation. Note the temperature is raised to accelerate the process. The position of GB is calculated the taking the average of constituent atoms.

In the irradiation process, GB is preferentially absorbing interstitials and become interstitial-loaded. Such damaged GB is intrinsically different from the pristine one in terms of mobility. To characterize the migration capability, the method described by Trautt et al. [146] to extract the planar GB mobility in the zero driving force limit is adopted. In particular, the method relates the diffusion coefficient of random walk to mobility. Starting with irradiated and un-irradiated systems which contain interstitial-loaded and pristine GBs, respectively, each configuration is held at 1200 K using NVT setting for 500 ps after first applying NPT with zero pressure for 25 ps.
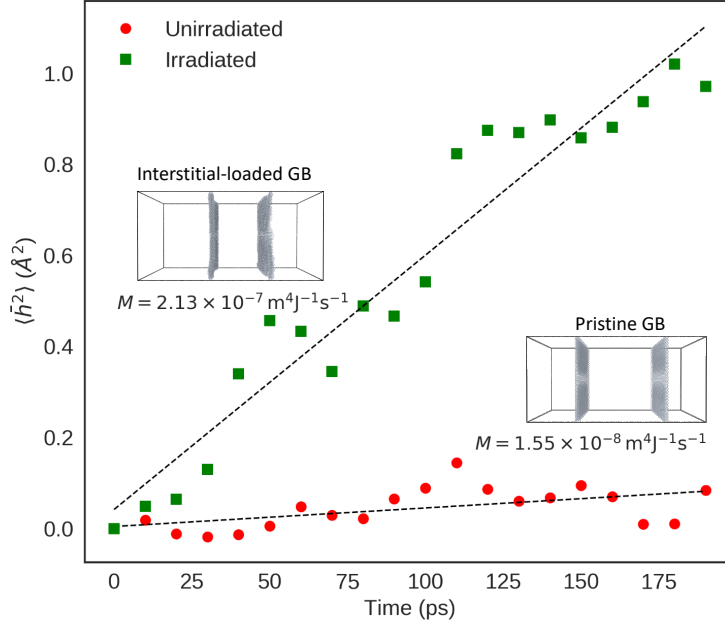
Figure 3-22: Temporal evolution of variance of GB position ($\langle \bar{h}^2 \rangle$) in irradiated and un-irradiated systems, respectively. The GB mobility (M) is calculated based on the linear fitting using $\langle \bar{h}^2 \rangle = Dt$, where D is the diffusion coefficient.

A total of 30 independent runs were performed to calculate temporal evolution of the variance of GB position, denoted as $\langle \bar{h}^2 \rangle$. The duplex GBs are out of interaction range in these cases. Figure 3-22 depicts linear trends of $\langle \bar{h}^2 \rangle$ with respect to the simulation time, and annotates the calculated mobilities (M). The damaged GB demonstrates a much higher mobility, which can be due to the more frequent atom re-organization in the disordered structure. The mobility of GB can be readily utilized to quantify the driven force provided by cascades assuming the interface velocity is linearly related to the force by M.

3.3.3.2   GB evolution

A complete process of GB evolution is captured after sequentially introducing sufficient number of damage cascades into the system. Such process is found to be generic by varying λ and system temperature. Starting from pristine $\Sigma 5(210)$, the random disruptions of thermal shock cause GBs to swing back and forth. Meanwhile, the initial flat profile becomes wider and rougher in view due to the preferential absorption

of interstitials, and interaction with nearby SFTs which induces localized curvatures. However, GBs maintain relatively straight profile due to the resilient nature and capability of self-healing [93, 97]. Figure 3-23(a) indicates a significant shift of GB position, and that the morphology is modified, being loaded with interstitials. Consequently, more vacancies are left in the bulk region as interstitial deficiency results in less recombination. The vacancies are mainly in the form of SFTs. These SFTs which are formed from aggregation of vacancies and direct production from cascades can be highly mobile [121] and then removed at GBs, which leads to a saturation of defect number density. The characteristic of GB being able to emit interstitials to annihilate nearby vacancies [21] and the wiggling motion sweeping up the defects in the way may contribute to a 'defect-free' zone near GBs [125] and the overall high radiation resistance in nanocrystalline metals. Note that most SFTs reside in the larger bulk region while the rare observation of SFTs in the small gap between GBs is an indication of GB's synergistic effect on efficiently absorbing SFTs generated during thermal spikes. Figure 3-23(b) shows that a SFT can simultaneously interact with both GBs and provides attraction that actuates GBs to get closer. After 1889 cascades as shown in Figure 3-23(c), the linkage provided by the SFT triggers direct contact between both GBs. Figure 3-23(d) describe the GB merging details within the span of 2 cascades. A rapid anisotropic expansion of perfect structure is observed and finally leads to the disappearance of GBs (Figure 3-23(e)). The system ends up with interstitial-type stacking faults and SFTs, confirmed with Voronoi cell analysis on defect types as shown in Figure 3-23(f).

3.3.3.3   Grain growth mechanism

The radiation-induced grain growth mechanism based on the analysis of GB evolution patterns is proposed. There are three stages involving different mechanisms as shown Figure 3-24. In stage I (Figure 3-24a), both GBs exhibit simple random walk due to the random occurrence of damage cascades. The fact that the initial stage of GB migration is weakly influenced by the spacing indicates that the two GBs are out of interaction range, and the migration is purely driven by cascades. In this period, a

93
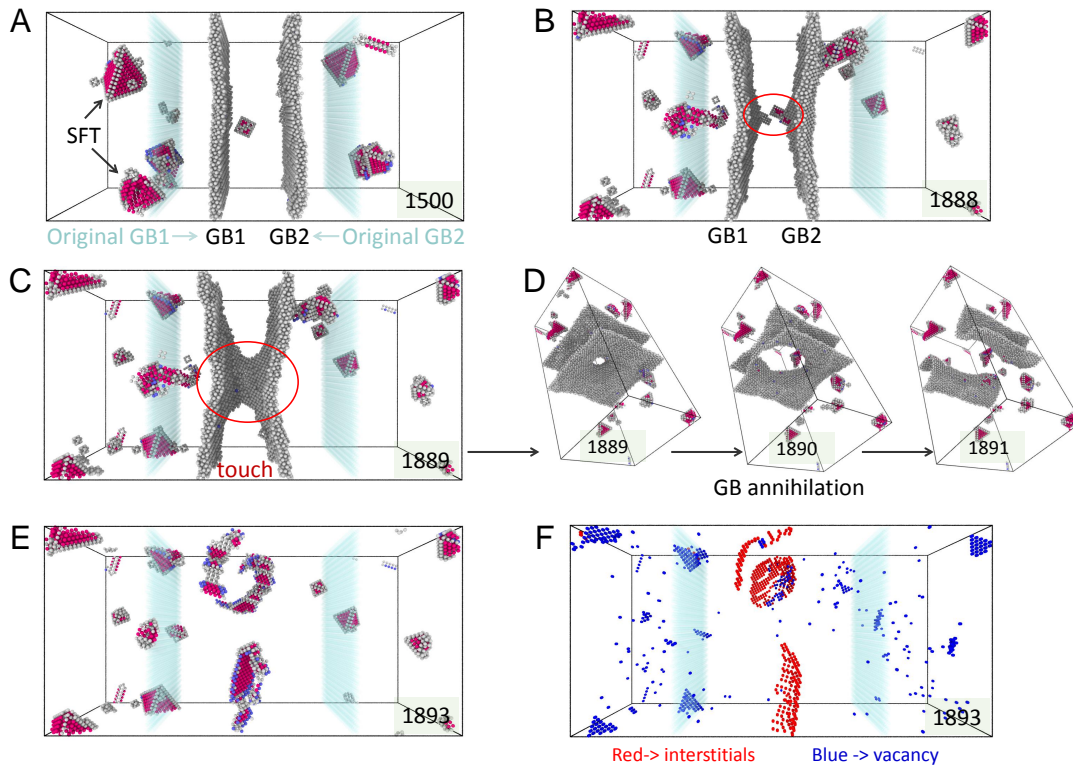
Figure 3-23: GB evolution under continuous irradiation within system λ = 11.3 nm, $T = 800$ K: (a) GBs and SFTs; (b) SFT interacts simultaneously with both GBs; (c) direct GB contact; (d) GB annihilation process; (e) GBs disappear into stacking faults; (f) defects in the system identified by Voronoi cell method. Number at corner denotes the configuration at the end of such many cascades. Atoms are colored by structure-type after minimization. Shaded turquoise indicates the location of initial GBs. Only large atom clusters are shown in (a-e) for ease of visualization.

random walk model as described in [146] can be able to characterize the mobility of GBs. The mean position of GB drifts slowly from the initial location, and a large deviation becomes increasingly less probable. By increasing the number of cascades, the random walk ultimately shrinks the distance between GBs to the extent that both GBs can synergistically contribute to the capture of defects generated inside the smaller bulk region. The observation of defect deficiency in the region as shown Figure 3-24b validates the hypothesis. Such efficient absorption of SFTs pull closer both GBs. Therefore, in this stage II, GB shows a biased migration behavior. Specifically, the random walk model breaks down here as the two GBs would rather continue approaching than depart. As distance decreases even more such that SFTs can directly connect both GBs, additional perturbation from cascades can effectively trigger the GB annihilation process. In stage III (Figure 3-24c), the rapid interface motion is driven by curvature. Perfect crystal structure quickly dominates the simulation cell. This process is finished within tens of pico-seconds in contrast with the slow motion for planar GBs.
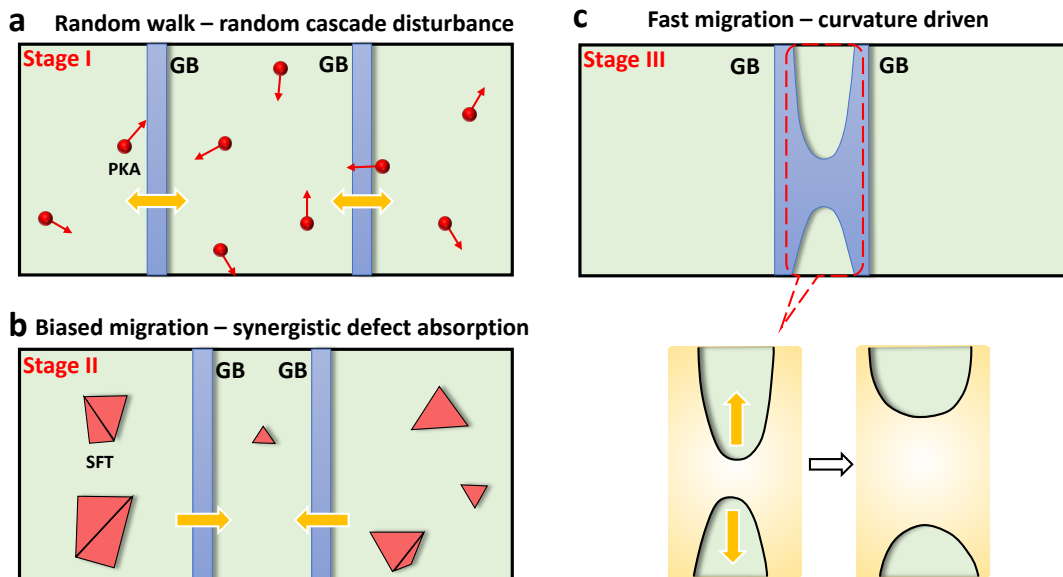
Figure 3-24: Grain growth mechanism from GB evolution: (a) Stage I: GB exhibits random walk due to the random disturbance from damage cascades; (b) Stage II: biased GB migration dominates as the distance decreases enough to allow for synergistic absorption of defects generated during thermal spikes; (c) Stage III: rapid curvature-driven GB migration after direct contact.

It should be noted that GB migration is a result of both direct impact of thermal spikes at GB region and GB-defect interaction. The former introduce local melting volume which can directly influence the atomic jumps in GB. Indirectly, the produced SFTs can be mobile to be absorbed at GB, which induces change in its morphology and mobility.

3.3.4   Discussions

Intense grain growth is expected in crystalline materials with ultra-fine grain size. Although thermally-activated grain growth has been well-analyzed [147], there is still limited understanding towards the mechanisms of radiation-induced grain growth in irradiated nanocrystalline systems. This simulation study aims to demonstrate the atomistic details to bridge the gap between GB migration and grain growth. Multiple simulations on spacing and ambient temperature have demonstrated this generic evolution process of GB migration until annihilation, regardless of grain size and system temperature, though the exact migration velocity varies with different settings. These MD simulations of radiation damage provide details of the impact from thermal spikes, the defect-GB interaction and GB migration, which are hard to resolve with experimental techniques. By monitoring the change in atomic configuration after each damage cascade, we can quantify the motion of individual boundaries, analyze the GB evolution and extract the mechanisms of radiation-induced grain growth. Although GB migration essentially boils down to thermal diffusion of atoms, the long range thermally-activated process is neglected due to the constraint of MD time frame. The evolution is driven by thermal spikes at GBs and GB-defect interaction including the preferential loading of interstitials in GBs and SFT-GB interaction. It is reasonable to believe that this study method works well at high dose rate or relatively low temperatures where diffusion of defects is restrained, but interstitials and defective SFTs [121] can still be mobile to be absorbed by GBs. GB evolution is accelerated by increasing the ambient temperature in the simulations, due to the elevated mobility of defects and deeper influence of thermal spikes at GBs. Consequently, GBs are observed to migrate faster, with much less dose required to facilitate GB annihilation.

The nonuniform local curvatures can be induced by thermal spikes at GBs and short-range GB-SFTs. On one hand, the curvature can explain the self-healing nature of GBs, which maintain the planar profile during irradiation. On the other hand, such distortion contributes to GB structure re-organization and observed profile oscillation. Due to the random occurrence of cascades, a random-walk model can be established to describe GB migration. Non-randomness emerges when the distance between both GBs decreases to a range where generated defects trapped in between are efficiently absorbed and large SFTs can simultaneously interact with both neighboring interstitial-loaded GBs. Ultimately, upon the adjoint of both GBs, curvature-driven interface migration dominates and leads to rapid GB annihilation, with a velocity orders of magnitude higher than that of planar boundaries. The proposed three stage mechanism of grain growth can be utilized to develop a more thorough theoretical analysis of radiation-induced grain growth rates and grain growth in polycrystalline metals when subjected to elevated temperatures [148] or radiation fluxes [149]. This methodology introduced here has practical guidance in engineering stable GB structures to maintain radiation resistance; future study could vary the characteristics of GBs such as boundary types and introduce solute atoms so as to provide guidance for optimizing radiation-resistant nanocrytalline materials. The desired structures are supposed to resist radiation-induced migration and grain growth, improving the long-term microstructure stability. It can be potentially reinforced by introducing external objects such as fine dispersoids [150, 151]. Another technique is via interface complexion, by introducing segregating solutes and transforming the original GB into an intergranular amorphous film. Such design will be analyzed in the next section with Zr-doped NC Cu.

3.4 Radiation effects in solute-stabilized nanocrystalline metals

Radiation-enhanced grain growth poses a serious concern for the application of nanocrystalline materials. Interface complexion has been used to stabilize grains by decreasing boundary energy. Specifically, replacing the original GBs with amorphous films may provide one avenue to achieve superior mechanical strength and structural stability. This study aims to provide an assessment of radiation-induced behavior and radiation performance in Zr-doped nanocrystalline Cu.

3.4.1 Introduction

Nanocrystalline (NC) materials can exhibit extremely high strength. However, they also experience rapid grain growth even at relatively low temperatures, due to the large driving force of grain coarsening provided by extra grain boundary (GB) area. Although grain growth was recognized as a consequence of thermal instability where curvature-drive GB migration is activated, radiation damage [128] can initiate such phenomenon even at low homologous temperature regimes where diffusion is very limited. Furthermore, the mechanism of grain coarsening can be substantially modified due to the GB chemistry [143, 152–154].

Alloying NC materials has been proposed to stabilize against grain growth in the way that it may effectively reduce GB energy via solute segregation or maintain barrier to GB migration. In the former scenario where alloying elements can strongly segregated to GBs, Kalidindi and Schuh introduced a stability criterion [155] by comparing the enthalpy of GB segregated state versus stable bulk phases. Stabilization requires that the segregated state is always preferred in comparison to forming other bulk phases such as solid solution, precipitates and ordered compounds. In addition to enthapic consideration, entropy can also contribute to stabilizing NC states [155]. Zhou et al. [156] utilized high-entropy GB complexions to enhance the thermal stability at high temperatures as the thermodynamic driving force for grain growth can

be effectively reduced. To date, various interfacial complexions such as solute doping, amorphous intergranular films (AIFs) have been explored to pursue superior material properties. Khalajhedayati et al. [127] reported that by combining nanostructuring and interfacial complexion engineering, both the ductility and strength of NC metals can be significantly improved.

Interfacial complexion with AIF provides a viable avenue to radiation-tolerant material design. Ludy et al. built a atomistic Cu model with Zr dopant pervaded a [310] GB and showed that the generated AIF acts as an unbiased sink to both vacancies and interstitials, whereas typical GBs preferentially absorb interstitials [6]. As the existence of AIF can increase the sink efficiency of radiation-induced defects, and also stabilize GB motion in radiation-free environment, the behavior of decorated GBs under intense irradiation has not been elucidated. In this work, an assessment of radiation performance of such design using Zr-doped NC Cu will be fully elaborated, including the ion-mixing behavior, defect dynamics, and interface evolution.

3.4.2 Methods and models

Molecular dynamics simulations with LAMMPS [68] are used to study the Zr-doped Cu system. Atomic interactions are described by an EAM potential from Borovikov et al. [157], which provides realistic stacking fault energies. The initial atomic configuration is prepared by referring to the procedures in previous Cu-Zr studies [158,159]: i) a bi-crystal with high angle symmetric tilt $\Sigma5(210)$ GBs is created; ii) two slices of atoms containing the GBs are selected and 25% of Cu atoms are replaced with Zr atoms; (iii) the two slices are then heated up to 1600 K and held for 200 ps, while the rest atoms are constrained to be fixed; (iv) the two slice of atoms are slowly quenched from 1600K to 650K over 200 ps; (v) the entire system is slowly quenched from 650K to 300K over 200 ps; (vi) relax the system at 300 K for 30 ps under zero pressure. From this process, a stress-free initial configuration containing two AIFs for radiation damage study is obtained. In order to characterize the interplay of the AIF thickness and grain size, configurations with multiple combinations by varying both parameters are created. Figure 3-25 demonstrates the structure with additional plot of atom

counts across one AIF. Note that the atoms in the AIF are mainly organized with short-range order while sharp peaks exist in the crystalline part indicating long-range order.

The system is firstly equilibrated to a zero pressure for 100 ps. In concert with the algorithm introduced in [79], consecutive PKAs with 5 keV kinetic energy are randomly introduced into the simulation cell. To accommodate high energy collisions, the Ziegler-Biersack-Littmark (ZBL) repulsive potential [69] is smoothly joined to the aforementioned EAM potential. An adaptive time-stepping technique is used to cap the maximum moving distance to 0.05 Å per timestep. A thermal bath to absorb excess energy is created by applying the Nosé-Hoover temperature-rescaling thermostat [72, 73] to the atoms at all sides of the simulation cell with a width of one lattice constant. The system is adequately annealed to the ambient temperature in MD time frame ($\sim$ 50 ps) before launching another PKA. In the way, $\sim$ dpa level estimated by Norgett-Robinson-Torrens (NRT) model can be achieved by increasing number of PKAs as necessary. It should be noted that the resultant dose rate is orders of higher than that under experimental conditions, nevertheless this procedure allows us to probe the material response and underlying mechanisms in the temperature regime where microstructural evolution is driven by damage cascades rather than long time thermal diffusion.

Defects and defective structures are recognized by Wigner-Seitz cell method [70] and common neighbor analysis in OVITO [115].

3.4.3   Results

3.4.3.1   Ion mixing

In current study, ion mixing due to damage cascades have been observed: the smoothly evolving Zr atom concentration profile during radiation damage. It implies a potential diffusion process of the doped Zr atoms driven by damage cascades, although Zr thermodynamically tend to segregate to GBs. The ion-mixed solid solution can be at meta-stable state.
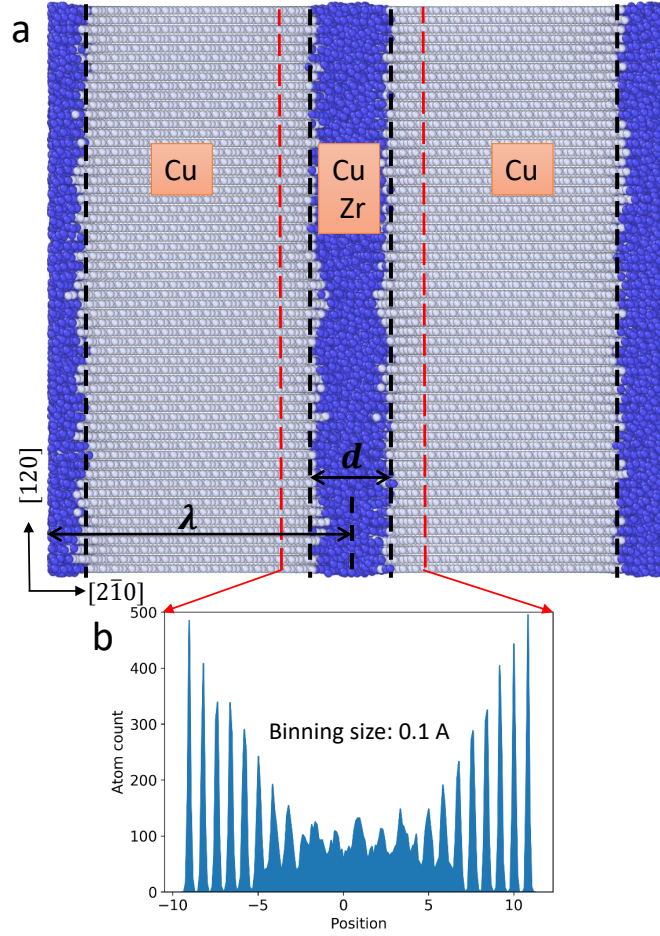
Figure 3-25: (a) A bi-crystal simulation cell containing two AIFs, where Cu Σ5(210) GBs are doped with Zr atoms (Cu-25 at.%Zr). λ and d denote the GB distance and AIF width, respectively. Atoms are colored by the structure type; (b) Atom counts across the AIF region between the two red-dashed lines, binned by a width of 0.1 Å.

A mathematical model may be applied to analyze the mixing process. Consider a thin layer sandwiched between two infinite bodies. One can characterize the system with 1D diffusion equation,

$$\frac{\partial c}{\partial t} = D \frac{\partial^2 c}{\partial x^2} \tag{3.1}$$

101

with boundary conditions,

$$c(\pm\infty, t) = 0 \qquad (3.2)$$

$$c(x \leq -d/2, 0) = 0 \qquad (3.3)$$

$$c(-d/2 < x < d/2) = c_0 \qquad (3.4)$$

$$c(x \geq d/2, 0) = 0 \qquad (3.5)$$

where d is the thickness of the AIF layer which centers at $x = 0$. The solution can then be written like this,

$$c_1(x,t) = \frac{c_0}{2}\left[\mathrm{erf}\left(\frac{x+d/2}{\sqrt{4Dt}}\right) - \mathrm{erf}\left(\frac{x-d/2}{\sqrt{4Dt}}\right)\right] \qquad (3.6)$$

where erf is the error function and is defined as,

$$\mathrm{erf}(x) \equiv \frac{2}{\sqrt{\pi}}\int_0^x e^{-t^2} dt \qquad (3.7)$$

Note that due to the periodicity of the GBs in MD simulations, the true solution should be a superposition of infinite single film solutions centered at λ separated locations.

$$c(x,t) = \sum_{k=-\infty}^{+\infty} c_1(x + k\lambda, t) \qquad (3.8)$$

Figure 3-26 schematically plots the Zr concentration profile resulting from Eq. 3.6: initially, Zr atoms concentrated inside the AIF (black step function); then the profile starts to broaden due to mixing (red curve); with longer irradiation, the neighboring profiles start to overlap (blue curve). Note that although $c_1(x,t)$ can provide a good depiction of early stages spread, more terms are needed as profiles start to overlap and nearby single film solutions contribute nonnegligibly to the overall solution.

As a simplified model, we can use three forms of Eq. 3.6 which center at 0, $-\lambda$ and λ (i.e. $k = 0, \pm 1$) to approximate the Zr atom concentration profile. As $4Dt$ is a manifest to the profile spread variance and ion mixing rate, this quantity will

be retrieved at each dose level by fitting to Zr distribution. By examining $4Dt$ with respect to dose (ϕ), the efficiency of ion mixing with AIFs can be assessed.
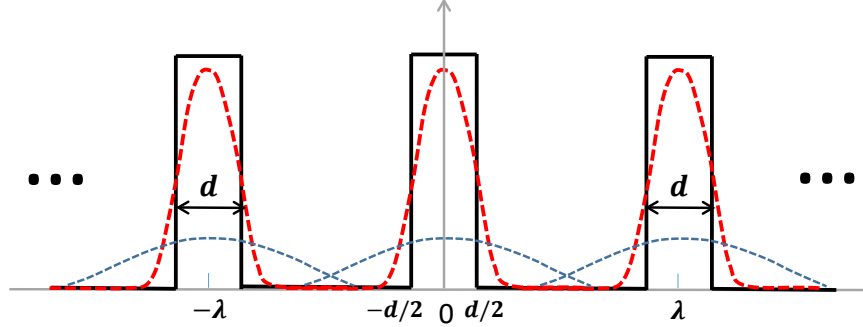
Figure 3-26: Schematic model of Zr atom mixing behavior: evolution of Zr concentration profile. Starting with initial condition (black step curve), before Zr atoms from neighboring AIFs coincide (red curve), Eq. 3.6 can provide a good estimation of Zr distribution. As the solution approaches the blue curve, more terms ought to be included to account for contribution from neighboring AIF.

In Figure 3-27, the fitting to the histograms indicates such treatment is a good approximation and the $4Dt$ is a strong indicator of the mixing pattern. Figure 3-27(a) compares the spread with respect to dose (ϕ) for systems with $\lambda = 5.7$ nm at 300 and 800 K with two initial AIF thickness settings, i.e. $d = 3.62, 10.85$ Å. It can be seen that $4Dt$ scales linearly with ϕ. However, with elevated temperature, the slope increases, which means that Zr atoms mix more efficiently due to fast diffusion in thermal spikes. On the other hand, thicker AIFs provide availability of more Zr atoms, and the slope becomes slightly larger. To examine the effect of λ, the calculation is repeated for λ=11.3 nm. By translating the number of cascades into the dose level for comparison, it can be seen from Figure 3-27(b) that the slope of the linear trend is not strongly related to the spacing λ. In contrast, the slope varies significantly with the ambient temperature and AIF thickness.

$$\frac{d(4Dt)}{d\phi} = \beta_{\text{CuZr}}(d, T) \tag{3.9}$$

where β denotes the slope from linear fitting. In this way, the ion mixing behavior can be estimated at different conditions. It is worth emphasizing that the ion mixing

behavior studied here isolated the long range thermal diffusion given the high dose rate. Figure 3-28 depicts the relation between β and T. The deviation from linear correlation (β vs. $1/T$) could attribute to the Darken biasing factor $(1 - \frac{2\Delta H_{mix}}{k_b T})$ in atomic diffusion at thermal spikes, as discussed by Johnson et al. [160]. It is expected the influence of increasing the ambient temperature comes from changes in the thermal spike region. To quantify the effect, a damage cascade is introduced into a well-mixed Cu-Zr system at different temperatures, and the mean squared displacement (R_{Zr}^2) is then calculated after annealing the cascade. The upper-right inset of Figure 3-28 plots R_{Zr}^2 versus β, which demonstrates a good linear correspondence. The displacement of Zr atoms are mostly inside the thermal spike region which contains larger volume at higher temperatures as shown in the left-bottom inset of Figure 3-28. It confirms that the temperature effect on ion mixing mainly lies inside the thermal spikes volume, rather than modify the diffusion of defects during this MD timescale.
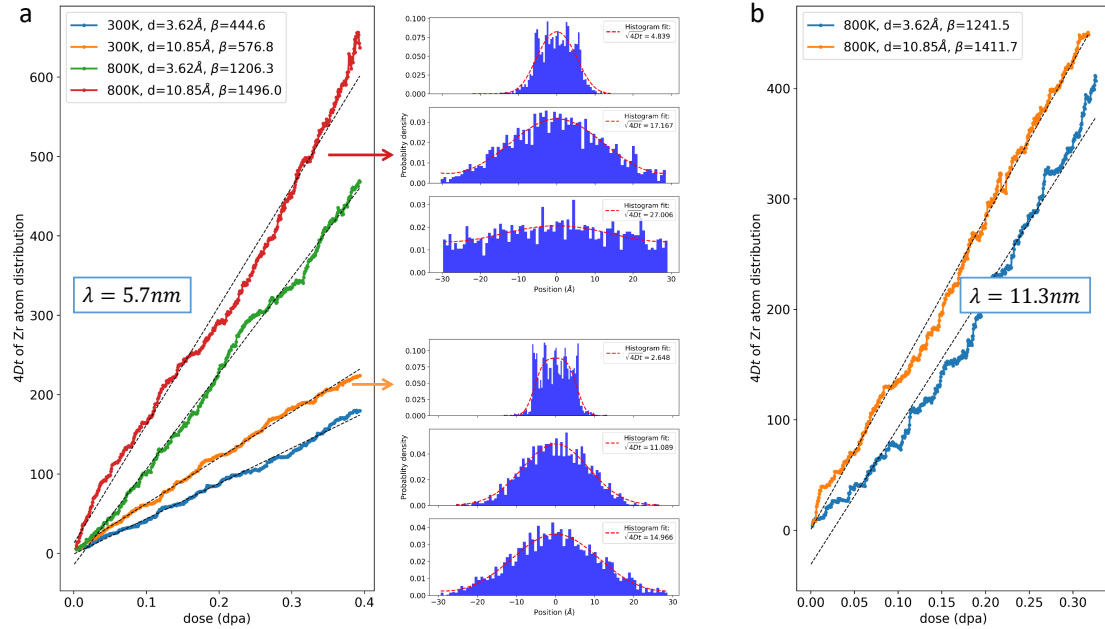
Figure 3-27: (a) Model fitted $4Dt$ of Zr concentration profile with respect to the damage level for systems with $\lambda = 5.7$ nm and initial $d = 3.62, 10.85$ Å at 300 and 800 K. Therein, the fitting to $d = 10.85$ Å are plotted along with the histogram after 10, 250 and 500 cascades, where $T = 800$ K shows much quicker Zr mixing rate. (b) Model fitted $4Dt$ of Zr concentration profile with respect to the damage level for systems with $\lambda = 11.3$ nm. β denotes the slope of linear regression.
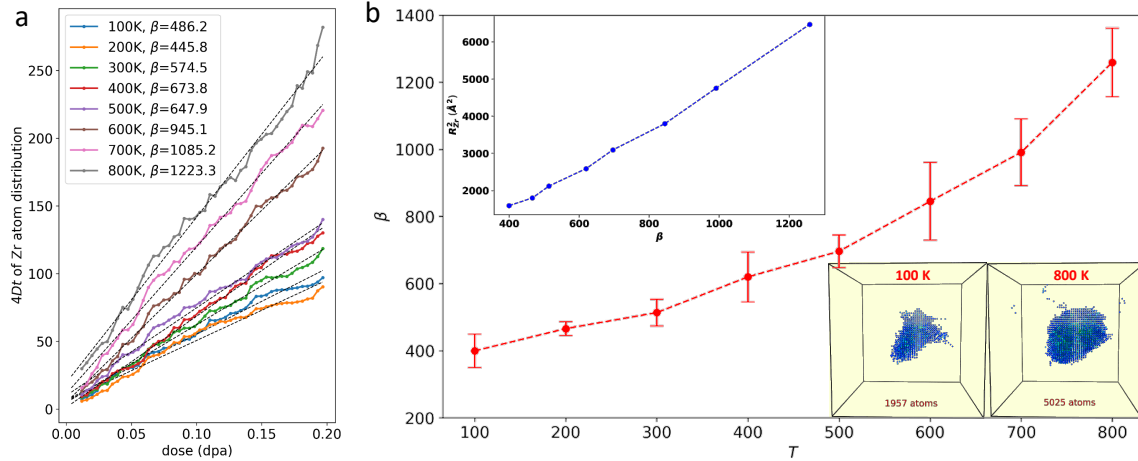
Figure 3-28: (a) Model fitted $4Dt$ of Zr concentration profile with respect to the damage level for systems with $\lambda = 11.3\,nm$ and initial $d = 10.85$ Å at 100-800 K. (b) Linearly fitted slope (β) versus T; upper-left: β versus the mean squared displacement of Zr atoms after single damage cascade in a well-mixed Cu-Zr system at different temperatures; bottom-right: cascade induced displacement field at 100 and 800 K.

Additional simulations show that if we continue introduce cascades into the system, Zr atoms eventually become well mixed with Cu atoms. The system becomes metastable; nevertheless, given sufficient thermal annealing time without the presence of irradiation, these bulk Zr atoms might segregate back into the GBs [127].

3.4.3.2   Defect reduction

The ample amount of GB area in NC materials provides strong sinks to irradiation induced defects. However, due to the presence of dopant atoms in GB and subsequent ion mixing, unique features emerge in terms of the defect reduction mechanisms. Figure 3-29 compares the radiation responses in Cu (a-b) and Cu-Zr systems (c-f). First, there are common observations shared between them: i) GBs can effectively absorb defects; ii) the residual defects in the bulk region are mainly vacancies. The differences include: i) initially, AIF layer is constructed in Zr-doped GBs instead of perfect symmetric tilt GBs as in Cu (a and c); ii) in Cu, there is frequent formation of large SFTs (b) due to aggregation of vacancies and direct production of cascades; while in Cu-Zr, SFTs are much less frequent and smaller (d); iii) in Cu-Zr, the defective structures are generally small in size (e); (iv) Zr atoms well-scattered in the bulk due

to mixing are mostly consistent atoms of the FCC lattice rather than interstitials (f). Therefore, the damage reduction mechanisms are significantly different for Cu and AIF NC systems. In the former, radiation resistance is mainly attributed to SFT annihilation at GBs, nevertheless, in the latter, it originates from the effective defect recombination without the formation of large defect clusters.
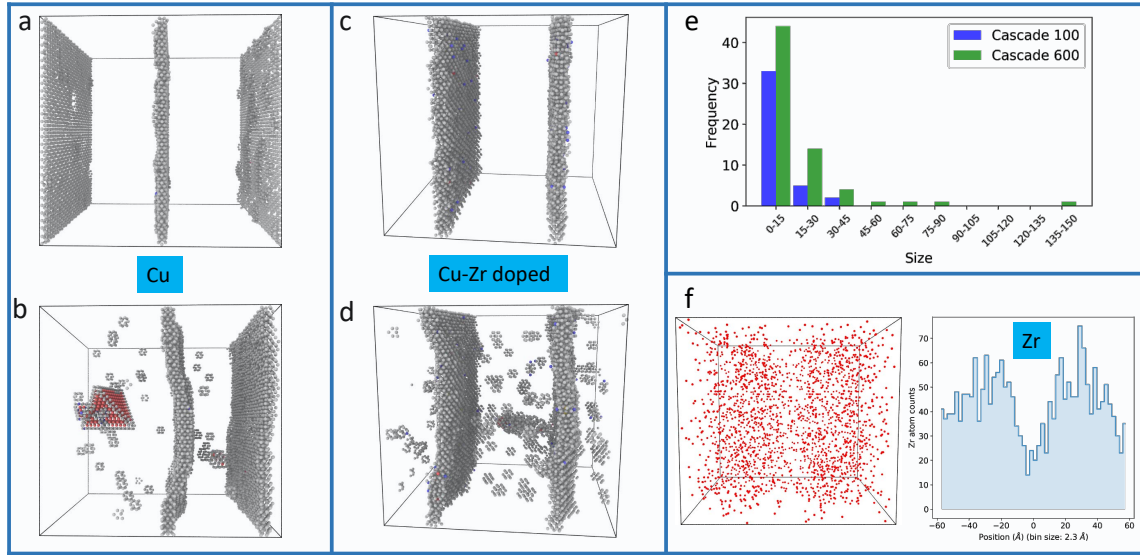
Figure 3-29: (a)-(b) non-FCC atoms shows the initial GB and atom configuration after around 200 PKA in pure Cu at 800 K, respectively. (c)-(d) non-FCC atoms shows the initial Zr-doped GB and atom configuration after 600 cascades at ambient temperature 800 K, $d = 3.62$ Å and $\lambda = 5.7$ nm. (e) Defective structure size distribution after 100 and 600 cascades for the Zr-doped system as in (d). (f) Zr atoms distribution in (d) where the left shows the atom positions and the right gives the histogram by binning atoms horizontally. (Non-FCC atoms are determined via common neighbor analysis)

The reason of predominant small defects in Cu-Zr system is the dispersion of Zr atoms from the AIFs. To identify the influence of Zr atoms in defect formation, we can utilize two systems containing no GBs: pure Cu with and without randomly distributed Zr atoms. From Figure 3-30 and evolution process, a few points can be summarized: i) in Cu, interstitials cluster into large stacking faults, whereas in Cu-Zr solution, small interstitial clusters scatter across the system; ii) larger vacancy clusters primarily appear in Cu across the whole radiation process; iii) the overall number of Frenkel pairs (FPs) are comparable. These observations imply that due to

the presence of defect-Zr binding, interstitials are less capable of long range diffusion. The binding energies between Cu point defect and Zr atom at lattice are calculated with molecular statics, with E_b(Cu vacancy, Zr)=0.11 eV and E_b(Cu [100] dumbbell, Zr)=0.36 eV. In this scenario, defects are more likely to annihilate locally or form small clusters. Therefore, ion mixing is an important contributing factor to the damage reduction of an AIF-engineered system.
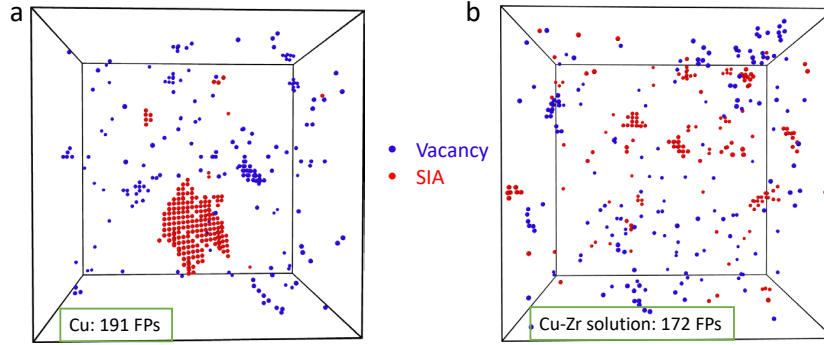
Figure 3-30: (a)-(b) Residual defects in pure Cu and Cu-4.65 at.%Zr solution after 500 cascades, respectively. Blue dots denote vacancies and red dots are SIAs, both of which are equal to the number of Frenkel pairs (FPs) shown in the figure. The concentration of Zr is approximated using the number of Zr atoms in $d = 3.65$ Å of Cu-4.65 at.%Zr and $\lambda = 5.7$ nm system.

The efficiency of defect reduction of AIF in comparison with perfect GBs can also be characterized by calculating the number density of defects in the bulk region. Figure 3-31 shows the total defect and vacancy density versus dose by counting corresponding defects in the simulation cell excluding the interface regions. It can seen that i) the residual defects in both system are comparable; ii) the majority of the defects are of vacancy type.

3.4.3.3 Interface evolution

One important motivation of Zr doping is to pin down GB and alleviate the problem of grain growth expected in NC materials. The addition of Zr atoms can not only reduce GB energy to lower the driven force, but also it provides additional drag to GB motion. Therefore, it is expected that the mobility of GB will decrease significantly. Figure 3-32 compares the interface movement in Cu (green) and Zr doped Cu (red). It can

107
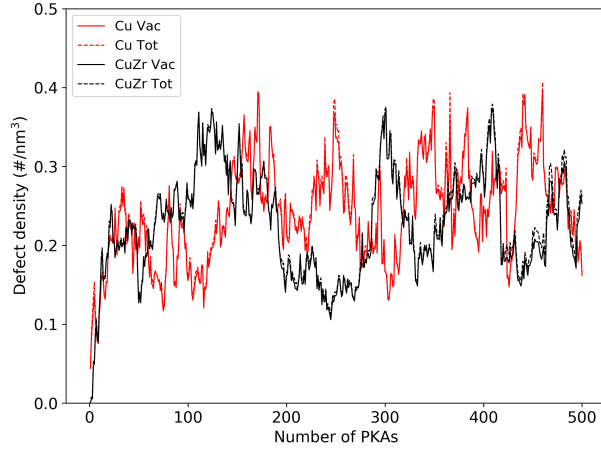
Figure 3-31: Residual defect density in the bulk region of in Cu containing GB (red) and Zr-doped GB (black), respectively. Solid curve denotes the total number of defects including both vacancies and interstitials, and dashed curve plots the number density of vacancies. System setting: $\lambda = 5.7$ nm and $T = 300$ K.

be seen that the location of the interface in the doped system stays almost the same with increasing irradiation; the fluctuation is induced by the random disturbance of cascades. By contrast, in the un-doped system, the two GBs shows apparent migration. Green curve in Figure 3-32 plots the gradual approaching of the two GBs, as also reflected in Figure 3-30(a-b); as the distance continues to decrease, the two GBs adjoin at some points, followed by quickly merge of GBs and ultimate disappearance implying grain growth. This process is elaborated in Chapter 3.3.

It should be noted that although the planar interfaces are observed to be flexibly distorted and then self-heals to straight profile in undoped Cu as seen in Chapter 3.2, the pattern has not been seen in the doped system. The reason could be the drag of Zr atoms so that the interfaces don't experience large morphological variations.

3.4.4 Discussion

This study focuses on the understanding towards radiation effects of interface-engineering nanocrystal, specifically, Zr-doped NC Cu. The amorphous layer created by Zr doping acts as interganular 'glue' and unsaturable defect sinks, which contributes to interesting phenomena, which are elaborated from three aspects: ion mixing, defect
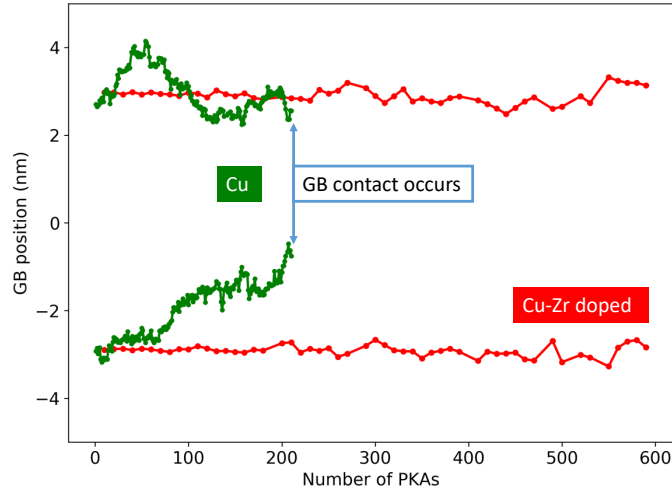
Figure 3-32: GB location in pure Cu (green) and doped Cu-25 at.%Zr GB with $d = 3.65$ Å, $\lambda = 5.7$ nm system (red) versus increasing damage level. The ambient temperature for both systems is 800 K. Note that in pure Cu, the two GBs have direct contact and start to merge at around 200 cascades.

dynamics, and interface evolution.

The ion mixing behavior can be well described by the diffusion model and the solution is approximated with three single film solutions. The fitted $4Dt$ has a linear relation with dose. Th slope is found to be dependent on ambient temperature and initial AIF thickness. Previous studies on ion mixing in bilayers under heavy ion bombardment characterize the mixing rates with the consideration of chemical effects. With suppressed radiation-enhanced diffusion at low temperatures, the phenomenological model proposed by Johnson et al. [160] assumes mixing occurs by chemically biased diffusional processes within a thermal spike, and the mixing rate ($\beta := d(4Dt)/d\phi$) depends on thermodynamic properties including heat of mixing and cohesive energy. Workman et al. later achieved excellent agreement by testing low temperature irradiated elemental $4d$-$5d$ metallic bilayers and comparing with the model prediction [161]. As an alternation to bilayer structure, the behavior of atom mixing with sandwiched AIF should also depend on the thermodynamic characteristics and potentially carry similar formulation of mixing rate. Additional parameters including the physical dimension of AIF thickness and temperature variations should also be accounted as noted in Eq. 3.9. By studying multiple combinations of doped

GBs, such hypothesis can be verified.

Note that the multiple cascade simulations imply a dose rate orders of higher than that in common irradiation experiments. By utilizing such simulation technique, system evolution is driven by thermal spikes and long term thermal diffusion is neglected. This assumption can be reasonable when thermal diffusion is not dominant. Although there is thermodynamic driving force for Zr to segregate into GBs, de-mixing has not been observed after holding the irradiated systems at 800 K for 1.0 ns. The irradiated mixed system is at metastable state, and segregation of Zr atoms to GB is not feasible during the simulation span.

Contrary to the understanding that GBs in NC materials preferentially absorb interstitials over vacancies, previous work done by Ludy et al. [6] characterize AIFs as unbiased sinks to both types of point defects by placing a PKA near AIF and launching towards the film. The single cascade simulation describes the direct interaction between AIF and thermal spike. The study demonstrated a high efficiency of AIF absorbing defects when cascades occur inside or very close to the AIF. However, the perspective is not enough to explain the results of multiple-cascades as i) residual defects in the bulk region are still vacancy-type dominated; ii) the number density of defects for both systems are closely comparable. The reasons are as follows. First, PKAs are randomly introduced into the system consecutively, which means a large proportion of thermal spikes do not have direct interaction with AIF. The residual defects from these cascades attempt to diffuse from the bulk. Interstitials with higher mobility are preferentially absorbed, either via recombination with vacancies or removal by AIFs. Hence, more vacancies are left behind, in the form of point defects or small clusters. On the other hand, for those cascade regions that overlap with AIF, one can expect ultra-efficient defect reduction without obvious bias towards any type of defects. Second, Zr atoms scattered in the bulk due to ion mixing can create a heterogeneous potential energy landscape, which means that the diffusion is confined to the local region. The long-range 1D diffusion mode for interstitials is limited. The decreased diffusion length supports the observations of isolated defects and small clusters, as defect reduction by recombination is encouraged. Ultimately, the concen-

tration of vacancies can then saturate at a low level. It appears that the presence of Zr can also change defect property inside thermal spike, where direct production of large clusters is suppressed after the locally disordered region anneals. In contrast, for the un-doped GB system, it can be observed the formation and subsequent fast motion of large SFTs. As the imperfect SFTs can possess a high mobility [162], absorption of SFTs at GBs can effectively lower the number of vacancies, which is reflected by the large fluctuation in Figure 3-31. Thus, although the defect concentration for both systems oscillates at similar level, the underlying mechanisms intrinsically differ.

Adding doping atom effectively pins down the motion of GBs, thus grain growth can be greatly reduced. Although Zr atoms are manufactured to concentrate in GB, the diffusion due to ion mixing lowers the content of Zr in the AIF. However, the deficiency of Zr atoms doesn't change amorphous configuration in AIF. Such property is extremely important to maintain the ductile mechanical behavior contributed by the AIF for dislocation absorption [158]. Meanwhile, the planar interface shows stiffness in response to damage cascades. The nearby dispersed Zr atoms create a strain field from atomic mismatch anchor AIF motion, which can explain why the interface are stiffer and experience much less local morphological distortion compared with un-doped GB system.

3.5 Summary

With the algorithm to appropriately introduce random numerous damage cascades into the simulation cell, one can achieve experimental dose level and obtain reasonable comparison with experiments. It should be emphasized that the dose rate is orders of magnitude higher than that in experiments. The applicability of using such technique to simulate the dynamic radiation process should be limited to a temperature regime where radiation is the dominant driving force to actuate microstructure evolution and long-range thermal diffusion of atoms is negligible. However, the fundamental mechanisms of defects interaction and local structure evolution should stand valid regardless. In the Ni-Fe alloy study, experimentally consistent results are acquired on the radiation resistance with compositional dependence. The heterogeneous diffusion and thermodynamic mixing energy can explains well the observation. Regarding NC Cu, multiple aspects including GB-mediated SFT annihilation, grain size effect, grain growth, and grain stabilization via interface complexion are examined. Extending from these studies, other material systems such as high entropy alloys with combinatorial elements, and material designs such as nanolaminate, nano-dispersoids, and interface engineering can also be investigated to optimize material parameters for experimental testing.

It is worth emphasis that the neglect of long-term dynamics can become a concern in comparing with experiments, in scenarios where it plays a major role in dictating microstructure evolution such as high temperature and low dose rate. To alleviate this concern, there are multiple potential ways to go beyond the MD scale, such as accelerated MD, and mesoscale methods (Figure 4-1). These longer scale methods such as rate theory and kinetic Monte Carlo usually need much constitutive information from lower length scale simulations to describe the interaction mechanisms and rates; hence, the practice of deducing high fidelity models based on these techniques is sometimes subject to criticism due to the lack of enough understanding of the physical processes. However, these physics-based computation models with careful calibration have the potential to predict material behavior under different

radiation conditions. In the next chapter, the "multiscale" concept in combining multiple scale-specific methods to keep up with experimental conditions is demonstrated with specific examples of ion irradiation.

Chapter 4

Multiscale modeling of radiation-induced defect evolution

Although atomistic simulations as demonstrated in previous chapter can provide detailed information of radiation process on the order of nano-seconds, observations of microstructure are usually orders of magnitude higher in both time and spatial domain. Extrapolation from atomistic methods may be misleading without the long term defect dynamics. To resolve the time limitation, serious efforts have been put into developing accelerated molecular dynamics methods such as temperature accelerated dynamics [163], parallel replica dynamics [164], and hyperdynamics [165]. However, the description of large system is well beyond the capability of MD simulations. Therefore, the multiscale framework which combines multiple scale-specific computation methods is natural for consideration, so as to characterize physical processes over a wide range of time and length scale, and ultimately render a direct comparison against experiments. This chapter will elaborate the multiscale concept by studying defect evolution in self-ion irradiated tungsten and iron.

4.1 Defect evolution in tungsten: deviation from power law

Declaration: This section mainly cites from my published work in [166], with permission from the publisher.

4.1.1 Introduction

Tungsten has been chosen as one of the most suitable armor materials for fusion reactors, as plasma-facing materials will be subject to extreme conditions during operation. The divertor in particular will be exposed to simultaneous, heavy neutron irradiation and intense heat fluxes of up to 10 MW/m^2 [167]. Defects accumulated during the exposure to neutron irradiation are known to degrade key material properties, such as ductility and thermal conductivity [168]. Studies on radiation-induced defect cluster creation and evolution are key to providing fundamental explanations and predictions of thermomechanical property evolution, which will drastically impact the service lifetime of the components. It is therefore crucial to understand and be able to predict the long timescale evolution of microstructural change from the perspective of defect creation, interaction, and evolution.

Experimental research on radiation induced microstructural evolution is still limited, especially when fusion-relevant conditions are considered. Due to the extreme environment to be present in fusion reactors, fission neutrons and ion irradiation are commonly used as surrogates to study the radiation damage by fusion neutrons (typically at an energy of 14 MeV from deuterium-tritium fusion). However, due to the significant difference in the energy spectra of primary-knock-on atoms (PKA), the validity of using results from fission neutrons or ion beams to approximate fusion neutrons is still a matter of debate. Nevertheless, a number of previous studies have shed light on the mechanisms of radiation damage recovery. Residual electrical resistivity has been measured during the recovery process of radiation damage, to identify which defects were responsible and how quickly they moved [169]. The physical mechanisms

116

governing damage recovery and evolution still remain controversial, as the microstructural changes responsible for damage cannot yet be fully characterized. Recent direct observations of defect creation in tungsten in the transmission electron microscope (TEM) with automated image processing to detect cluster size distributions [170] have given indications of the longer-term evolution of defect clusters produced by radiation damage cascades. More recent experiments on annealing of polycrystalline and single-crystal tungsten present a better picture of defect evolution [171, 172] and links with material property changes [173].

This work combines multiple simulation methods, including binary collision approximation (BCA), molecular dynamics (MD), and rate theory (RT) in the form of cluster dynamics (CD), to model radiation damage in tungsten. The tungsten self-ion irradiation experiment at 30 K by Yi et al. [170] is chosen as an ideal test case for current CD code, as its relatively low helium generation rate (from its (n,α) cross section) makes for a relatively simple validation case. In addition, these simulations can provide insights on the evolution processes of defects, and additional sensitivity studies would help identify the important factors that contribute to the final experimental observations. In contrast with the notion that MD results can represent the long time scale observations due to the low temperature and a power law distribution of defect size was generated [174], current results show a clear deviation, especially for large defect sizes. It agrees well with the observations in the experiment [170], parameterized only by the types and sizes of mobile self-interstitial atom (SIA) clusters. This implies that the mobility of small SIA clusters in irradiated tungsten can be significant enough to explain experimental results, even at cryogenic temperatures. The influence of dose, dose rate, and PKA energy spectrum are also analyzed.

4.1.2 Methods

The SRIM code [18] is widely used to study ion beam implantation, and to compute radiation damage exposure in dpa using the BCA. A recent study [19] recommends that the Kinchin-Pease (K-P) option of SRIM should be selected for accuracy. In this work, 150 keV and 400 keV tungsten self-irradiation were simulated in SRIM using

Quick (K-P) mode with 100,000 ions, a displacement threshold energy of 80 eV [175] and a surface binding energy of 11.75 eV [176]. This resulted in PKA energy distributions for each ion irradiation condition, from which PKA energies were sampled in the subsequent MD simulations of damage cascades in tungsten. PKA energies were binned into energy groups of $[10^{1.9}, 10^{2.1}, \cdots, 10^{5.9}]$ eV.

For these simulations, two EAM potentials from [177] and [178], both of which are splined to the ZBL potential [69] for short range interactions were examined. The system is first equilibrated for ~ 20 ps at 30 K before introducing each PKA. Damage cascades are initiated by assigning a velocity to the center atom with a random direction. Each PKA energy studied consists of 10-20 independent simulations with different initial directions, with the full PKA energy range from 100 eV to 250 keV studied using the binning method described above. Note that this energy is a reduced form of particle kinetic energy, where electronic loss is excluded. Each cascade is simulated in the NVE ensemble cooled to 30 K by applying the Berendsen thermostat on boundary layers. The cascade process lasts for $\sim$50ps using an adaptive time step which allows a maximum one-step displacement of 0.01 Å. The simulation box is chosen for each PKA energy in order to ensure the whole damage cascade lies well within the periodic boundary. The subsequent point defect production from each simulation is analyzed using the Wigner-Seitz occupancy criterion. To identify defect clusters, the third nearest neighbor (NN3) and the fourth nearest-neighbor (NN4) distances are used to identify SIA and vacancy clusters, respectively [23].

Direct point defect and cluster production terms from each MD-simulated damage cascade are averaged across all directions and aggregated with weights according to the PKA energy spectrum from the SRIM simulations. In this way, the final distribution of clusters from self-ion irradiation at 150 keV and 400 keV is acquired. This quantity is used as the input to rate theory simulations as direct defect production terms, with pre-defined defect interaction coefficients from atomistic calculations [22]. The evolution of defect clusters can be described in terms of an evolving size distribution, with negative sizes representing vacancy clusters and positive sizes representing SIA clusters. The general description for the evolution of mobile species concen-

trations can be written as follows [30] assuming diffusion-limited reactions between defects:

$$\frac{dC_m}{dt} = \sum_n J_{m-n,m} - \sum_n J_{m,m+n} + \nabla \cdot (D_m \nabla C_m)$$
$$- \sum_t \sum_{s \in N(t)} k_{t,s,m}^2 D_m (C_m - C_{t,s,m}^m) + G_m \quad (4.1)$$

where C_m is the concentration of size m clusters of either vacancy or SIA type, G_m is its source term from the MD simulations, and D_m is its diffusion coefficient. Summation over all defect types and sizes is performed by automatically creating one equation for each cluster size and type, with the cross-terms (those with subscript n) providing the coupling between cluster sizes. Microstructural damage sinks such as dislocations in current study are identified by their type t; $N(t)$ are the subsets of type t sink; $k_{t,s,m}^2$ is the sink strength for cluster size m; $C_{t,s,m}^m$ is the concentration of species in the matrix close to sink s, approximated as C_m^{eq}, the thermal equilibrium concentration. $J_{m,m+n}$ is the net flux of point defects between clusters of size m and $m+n$, and $J_{m-n,m}$ is the net point defect flux between clusters of size m and $m-n$.

$$J_{m,m+n} = \beta_{m,n} C_m C_n - \alpha_{m+n,n} C_{n+m} \quad (4.2)$$

$$J_{m-n,m} = \beta_{m-n,n} C_{m-n} C_n - \alpha_{m,n} C_m \quad (4.3)$$

Here, $\beta_{m,n}$ is the absorption rate and $\alpha_{m+n,n} C_{n+m}$ is the emission rate of clusters of size n from clusters of size $m+n$, both of which can be calculated either by using parameters from lower length scale simulations or from empirical expressions.

Assuming that only very small clusters are mobile, such that $-m_v \leq n \leq m_i$, then the generalized equation for immobile clusters reads as follows:

$$\frac{dC_n}{dt} = \sum_{m=-m_v}^{m_i} (\beta_{n-m,m} C_{n-m} C_m - \alpha_{n,m} C_n)$$
$$- \sum_{m=-m_v}^{m_i} (\beta_{n,m} C_n C_m - \alpha_{n+m,m} C_{n+m}) \quad (4.4)$$
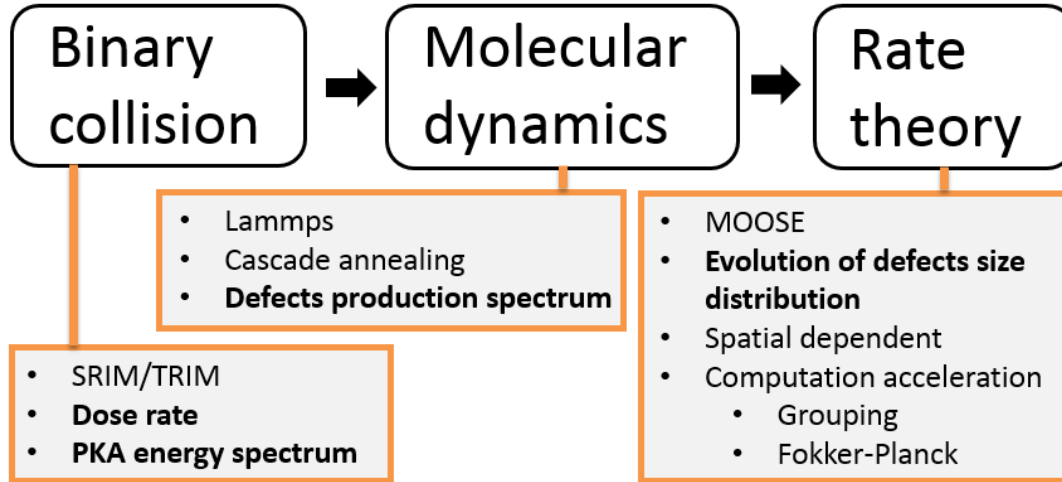
Figure 4-1: Multiscale simulation methodology used to study radiation defect size evolution. Key results extracted in each stage are marked in bold.

A calculation framework is built in MOOSE [179] to solve this very large number of equations, which represent the evolution of different defect species and sizes during tungsten self-ion irradiation. The functionality of the MOOSE custom "Action" object enables a relatively smooth approach to building a system with thousands of similar, fully coupled partial differential equations (PDEs) and ordinary differential equations (ODEs). Meanwhile, to improve the efficiency of the calculations, the grouping method developed by Golubov et al. [180] is implemented to group large clusters of the same type. A group width of 5×10^{-11} m in r-space as described in [181] has been applied. The solving process utilizes an adaptive timestepping scheme with timestep ranging from 1×10^{-9} to 0.01 s. A graphical summary of this full multiscale simulation framework is shown in Figure 4-1.

The key elements in studying the evolution of the defect size distribution are the choices of kinetic and thermodynamic parameters. Quantities such as migration energies, attempt frequencies, binding energies, and capture radii are taken to be consistent with previous studies of tungsten [22, 24]. Table 4.1 and 4.2 summarize the relevant parameters used in this study. The capillary approximation of binding energies is used for large clusters over a size of seven defects. Note that vacancy clusters are assumed to be spherical, while SIA clusters are assumed to be in the form of dislocation loops. In many CD studies, all diffusion is assumed to be isotropic.

However, it is generally accepted that 1D movement is preferred for most SIA-type defects with occasional rotation, i.e. a mix of 1D and 3D diffusion. SIA clusters in W may be regarded as a bundle of crowdions, which collectively have a similar migration barrier as a single one [182]. The rotation barrier of the [111] crowdion in tungsten has been calculated at about 0.4 eV by Derlet et al. [183]. Considering the low temperature constraint (30 K), SIAs and SIA clusters would mostly move in 1D. Therefore, the current CD implementation utilizes 3D kinetics for vacancy-type defects and 1D migration for SIA-type defects based on Kohnert and Wirth's work [184], which considers the effect of dimensionality in a CD model of Fe.

Item	value	comment
SIA (cluster) migration energy (eV)	0.013	1D
Vacancy migration energy (eV)	1.66	3D
SIA (cluster) migration attempt frequency (s^{-1})	$\nu_0 n^{-0.5}$	$\nu_0 = 6 \times 10^{12} s^{-1}$, n: defect size
Vacancy migration attempt frequency (s^{-1})	ν_0	$\nu_0 = 6 \times 10^{12} s^{-1}$
Mobile vacancy clusters	N/A	Immobile
SIA (cluster) bias factor	1.15	N/A
Vacancy (cluster) bias factor	1.0	N/A
Dislocation density $(\#/m^2)$	1.0×10^{12}	N/A
Atomic volume (m^3)	1.58×10^{-29}	N/A
Dislocation capture radius (nm)	0.65	Assumption
Point defect reaction distance (nm)	0.65	Assumption

Table 4.1: Parameters used in cluster dynamics (PART I).

SIA binding energies (eV)		Vacancy binding energies (eV)	
Size (n)	$E_{SIA}^b(n)$	Size (n)	$E_v^b(n)$
2	2.12	2	-0.1
3	3.02	3	0.04
4	3.60	4	0.64
5	3.98	5	0.72
6	4.27	6	0.89
7	5.39	7	0.72
>7	Capillary approximation [a]	>7	Capillary approximation [a]

a. $E^b(n) = (E^b(2) - E^{for}(1))\frac{n^{2/3} - (n-1)^{2/3}}{2^{2/3} - 1} + E^{for}(1)$
with formation energy $E^{for}(SIA) = 9.96\,eV$ and $E^{for}(V) = 3.23\,eV$

Table 4.2: Binding energies used in cluster dynamics (PART II).

Diffusivities are calculated according to an Arrhenius law, i.e. $D = D_0 \exp(-\frac{E_m}{k_B T})$ where D_0 is a prefactor depending on the attempt frequency and E_m is the migration energy, both of which are based on Table 4.1. The absorption rate between 3D

diffusing species is determined by $\beta_{m,n} = 4\pi(r_m + r_n)Z_{m,n}(D_m + D_n)$ where r_m and r_n are approximated by the capture radii, and $Z_{m,n}$ is a bias factor accounting for the strain field. For 1D diffusing species, the formalism described in detail by Kohnert and Wirth [184] is employed. Specifically, the interaction rates between 1D diffusing defects and other types is primarily determined by the cross-sections, which are readily categorized. It is assumed that the reactions between defects take place spontaneously whenever the two involved entities come closer than a specified reaction distance. Only emission of point defects is considered from clusters, and this rate is written as $\alpha_{m,n} = \frac{\beta_{m-n,n}}{\Omega}\exp(-\frac{E_b}{k_B T})$ where Ω is the atomic volume, and E_b is the binding energy of a point defect to a cluster of size m. As a simplification, the spatial dependence of defect production is not considered.

All related data files used to create the results and figures in this study can be found on our GitHub repository [185].

4.1.3 Results

PKA energy spectra for 150 keV and 400 keV tungsten self-ion irradiation, obtained from SRIM simulations, are plotted in Figure 4-2. The trend is as expected, with more energetic incoming particles extending the PKA spectrum to a higher energy regime. These PKA energies used for binning are then adopted in the MD simulations as initial PKA energies, to study the detailed behavior of point defect production in tungsten as a function of PKA energy. The final cluster size distribution is calculated as a weighted average with respect to each PKA spectrum. Figure 4-3 shows the number of point defects created versus E_{PKA}. Note that energy in the spectrum (E_{PKA}) is different from the MD damage energy (E_D) due to ignoring electronic stopping in the MD simulations. The partition of kinetic energy using this assumption is calculated according to the Lindhard method [1]. Wigner-Seitz cluster analysis on both 150 keV and 400 keV self-irradiation annealed cases reveals that slightly more vacancies are found in clustered states compared to interstitials with the clustering criteria. The proportion in Figure 4-4 is calculated by $\frac{F(n)}{\sum nF(n)}$ where n is defect size and $F(n)$ is the frequency of occurrences.
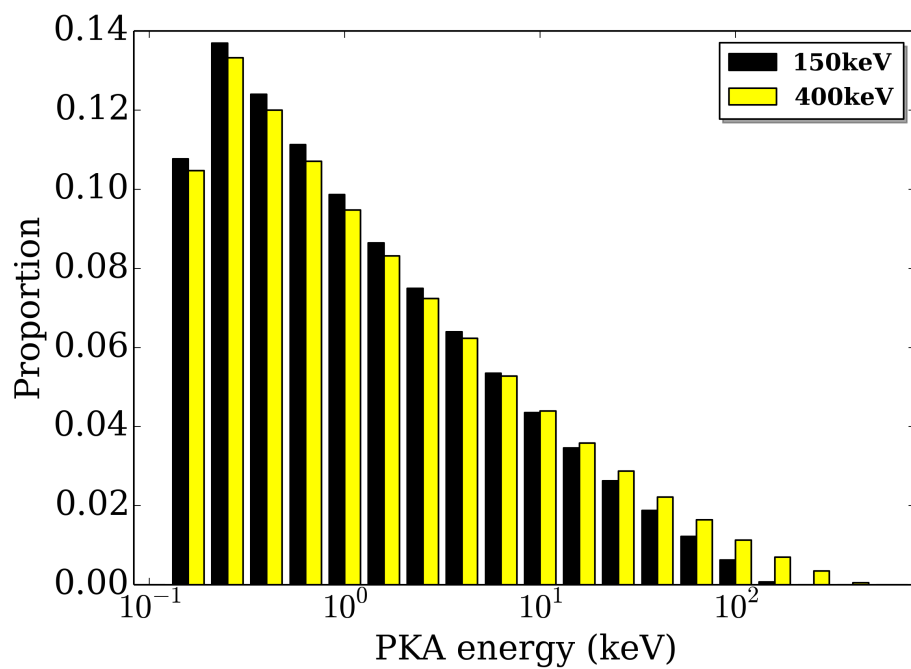
Figure 4-2: PKA spectra calculated from SRIM, for tungsten self-ion irradiation at 150 keV (black) and 400 keV (yellow)
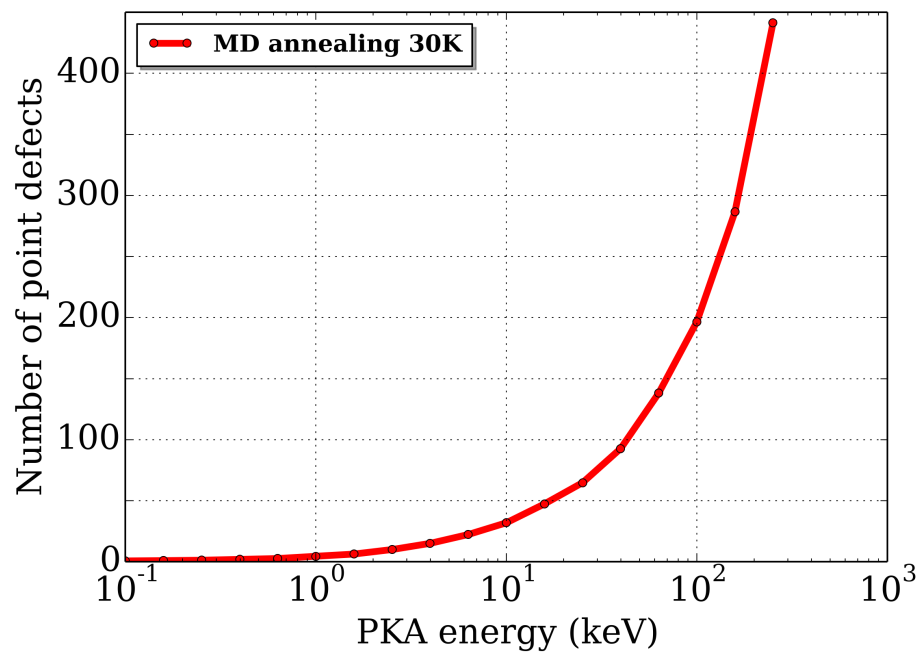
Figure 4-3: Number of defects created at various PKA energies in MD simulations
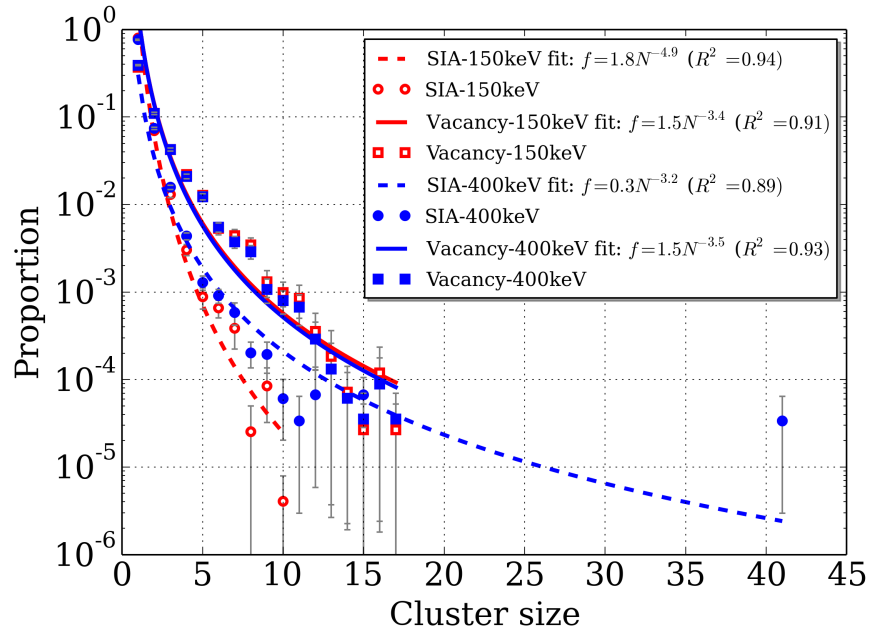
Figure 4-4: Defect cluster size distribution at 30 K during the primary stage of tungsten self-irradiation. For each case, a power law fitting is provided along with the corresponding R^2 value.

The MOOSE-based CD framework described in Equations 4.1-4.4, with parameters from Tables 4.1-4.2, is then used to perform the long timescale evolution of these created defects, the direct production of which (the source term G_m) in Equation 4.1 is calculated by multiplying the total defect creation with the size distributions from Figure 4-4. By solving this system of coupled ODEs, the time-dependent concentrations of all species of interest can be extracted. First, three sensitivity studies are presented to ensure that the framework produces expected results as functions of SIA cluster mobility, dose rate, and incoming ion energy. It has been found that at low temperatures, the rates of SIA cluster diffusion and absorption are the main communication mechanisms along the cluster size distribution. One would also expect that an increased dose rate leads to less severe microstructural change given the same dose and other parameters [186]. In addition, a larger incoming ion energy is expected to produce denser damage cascades, resulting in fewer point defects and more clustered vacancies and SIAs when normalized to the incoming ion energy [187]. Next, the total dose during 150 keV self-ion irradiation is varied to study the kinetics of evolution

of a stable cluster size distribution. Finally, the experimental parameters from the experiment of Yi et al. [170] are used in current CD framework to produce a direct comparison with the results of Sand et al. [174] and Yi et al. [170].

4.1.3.1 Effect of SIA cluster mobility

Figure 4-5 shows the defect size distribution after irradiation with 150 keV ions for one second, by varying the largest SIA cluster size (Ni_{max}) allowed to be mobile. As expected, the profile shifts preferentially to larger sizes with increasing Ni_{max}, with a peak large size evident when rather large SIA clusters are allowed to be mobile. Since more and more defect clusters are mobile, they can interact with each other more efficiently and agglomerate more easily into larger clusters. Comparing the calculated distributions in Figure 4-5 with in situ TEM observations [170], a similar trend is observed, which implies that only small SIA clusters are mobile. Even though there are recent MD studies of single large and highly mobile SIA clusters in tungsten [182], experimental results like those of Yi et al. consistently show a distribution of defects corresponding to smaller mobile SIA cluster sizes. The slope of the power law region in the data of Yi et al. best matches the simulations when the largest mobile SIA cluster is of size six, so this value is used in future parts of this study.

4.1.3.2 Effect of dose rate

The dose rate can be calculated from the experimental parameters of Yi et al., including dose and time duration. In the case of 150 keV self-ion irradiation, the dose rate was approximately 0.0125 dpa/s in the peak damage area. Two other dose rates of 0.025 and 0.05 dpa/s with the same MD-generated defect production spectrum are also included to explore the underlying trend of defect distribution vs. dose rate. It should be pointed out that the total dose is kept constant at 0.014 dpa. Figure 4-6 demonstrates that a higher dose rate leads to a slower shift of the profile to large cluster sizes, which would be expected given less time between overlapping damage cascades. This corresponds to a stronger, but still slow, driving force for radiation defects finding an equilibrium distribution. The results imply that more defects get
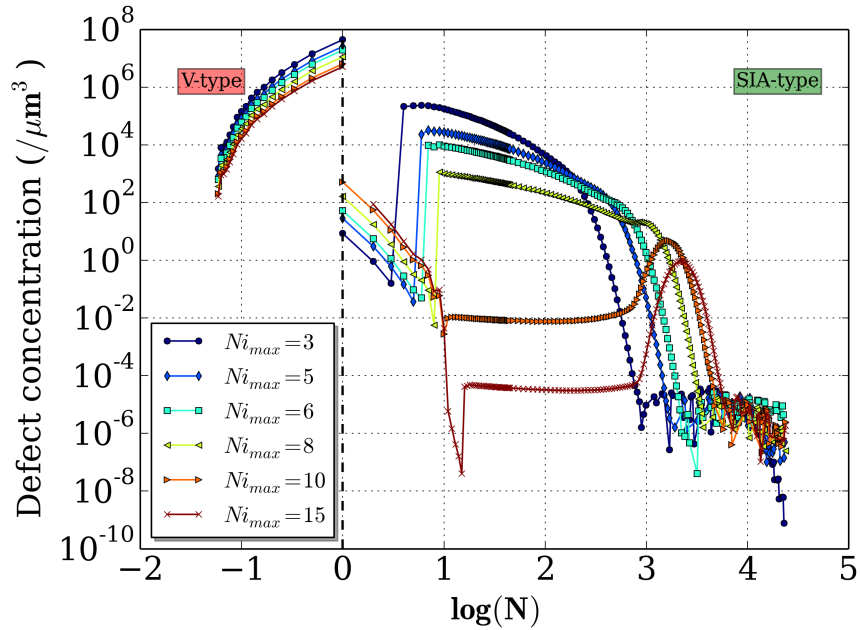
Figure 4-5: Defect size distribution with different mobility constraints on the largest mobile SIA cluster (Ni_{max}), after one second of 150 keV tungsten self-ion irradiation

annihilated in a short time due to the more intense production of defects, and hence imposing more of a time constraint for them to diffuse away from each other. It is important to point out that only the magnitude of the defect size distribution is lowered, while the slope at all points remains relatively unchanged.

4.1.3.3 Effect of ion energy

A key difference between 150 and 400 keV self-ion irradiation lies in the PKA energy spectrum (see Figure 4-2), resulting in a different defect production distribution (Figure 4-4). Note that to isolate the influence of the primary damage residual defects, the dose rate and total dose are kept equivalent for both simulations at 0.0125 dpa/s and 0.014 dpa, respectively. Figure 4-7 shows that the 400 keV case evolves more slowly than the other. This is due to a larger fraction of point defects in the high energy scenario, which less effectively combine to form large clusters.

126
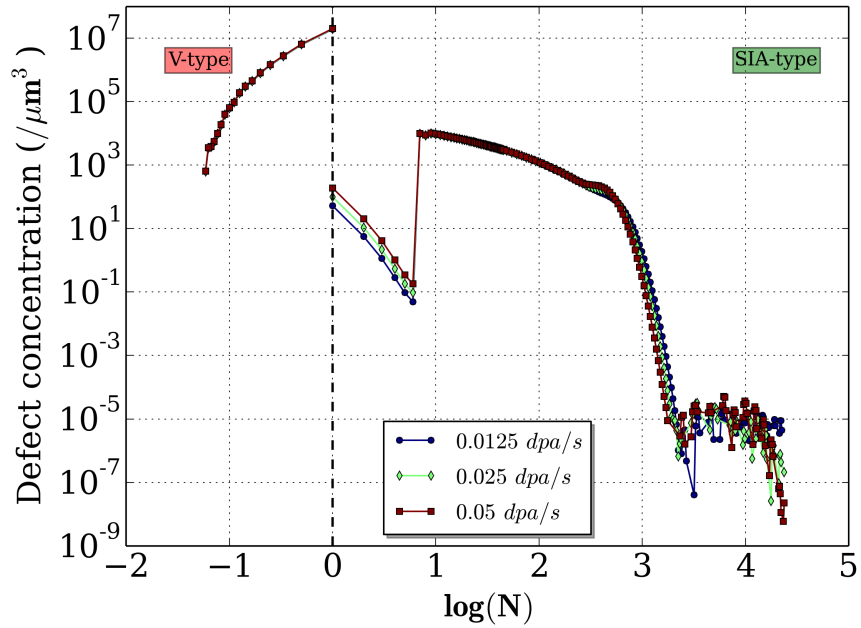
Figure 4-6: Final defect size distribution in self-ion irradiated tungsten, with three different dose rates applied to the same dose (with $Ni_{max} = 6$)
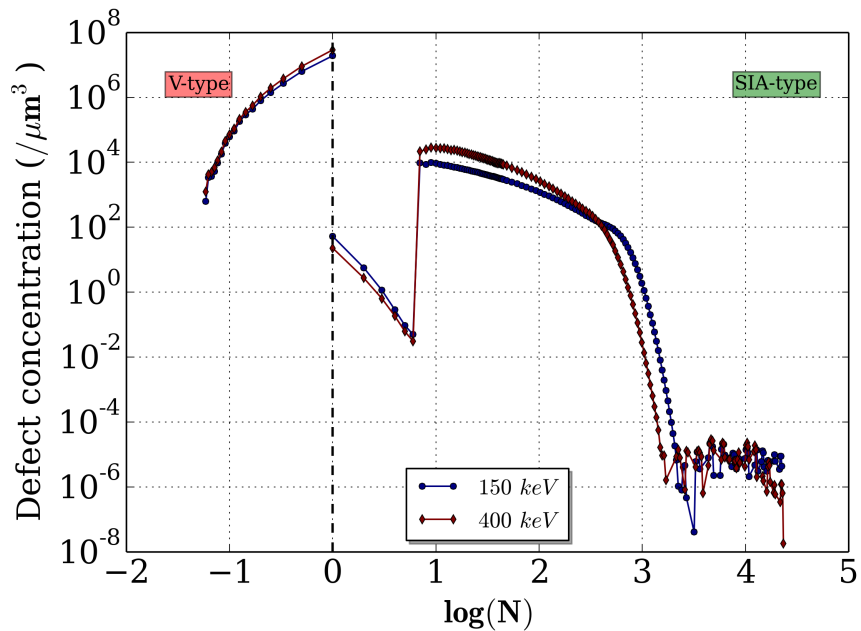
Figure 4-7: Defect size distribution in self-ion irradiated tungsten to 0.014 dpa, with incoming ion energies of 150 keV and 400 keV applied at the same dose rate ($Ni_{max} = 6$)

4.1.3.4   Effect of total dose

Various order of magnitude doses are compared using the 150 keV self-ion irradiation condition with a dose rate of 0.0125 dpa/s. The results are plotted in Figure 4-8a, indicating an increase in total defect number density and augmented agglomeration of small clusters into larger ones at higher doses. A plateau develops in the plot of cluster density with increasing dose (Figure 4-8b), which implies a temporary, metastable balance between the direct production of small defect clusters and the decrease in the total concentration of larger ones due to agglomeration with mobile SIA clusters. Notable is that the slope of the defect size distribution does not change for medium sized clusters after 10^{-4} dpa in Figure 4-8a, though small clusters continue to decrease resulting in more larger clusters. This is also consistent with our knowledge of defect cluster size evolution. Thus all four sensitivity studies yield relatively expected results, so the experimental case can be more confidently analyzed.

4.1.3.5   Effect of defect production rate

It should be noted that the choice of interatomic potential used in MD simulations in order to characterize primary damage can change the values for the defect production term in the CD model. The reason is that the description of atom interaction varies. To evaluate the sensitivity of the system evolution to defect production, a repeat of calculation are performed, with defect size distribution from another potential [178]. The results are presented in Figure 4-9. Similar pattern is acquired with an off-the-shelf power-law fitting by Sand et al. [188].

Although the choice of potential used in MD simulations may change the exact production rate of defect clusters, the mobility of large SIA clusters would not be significant enough to noticeably affect the observations. In this way, these BCA-MD-CD simulations generally agree with experimental results of defect cluster size distributions as measured in the TEM, irrespective of the choice of a suitably accurate interatomic potential in the MD simulations.
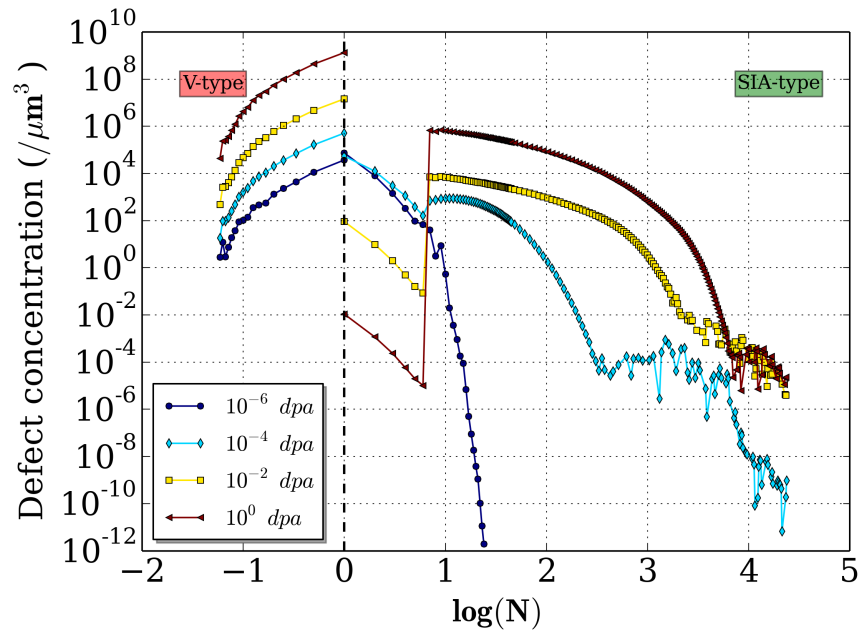
(a) Final defect size distribution with different doses at the same dose rate
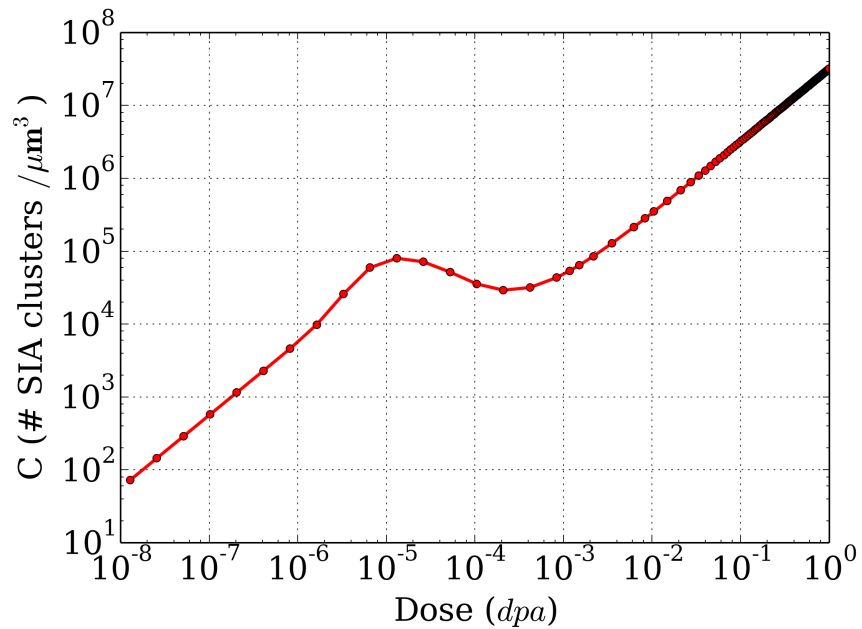
(b) SIA cluster density vs. irradiation dose

Figure 4-8: Effect of total dose on the defect cluster size distribution in self-ion irradiated tungsten, at a dose rate of 0.0125 dpa/s and a maximum mobile SIA cluster size of $Ni_{max} = 6$)
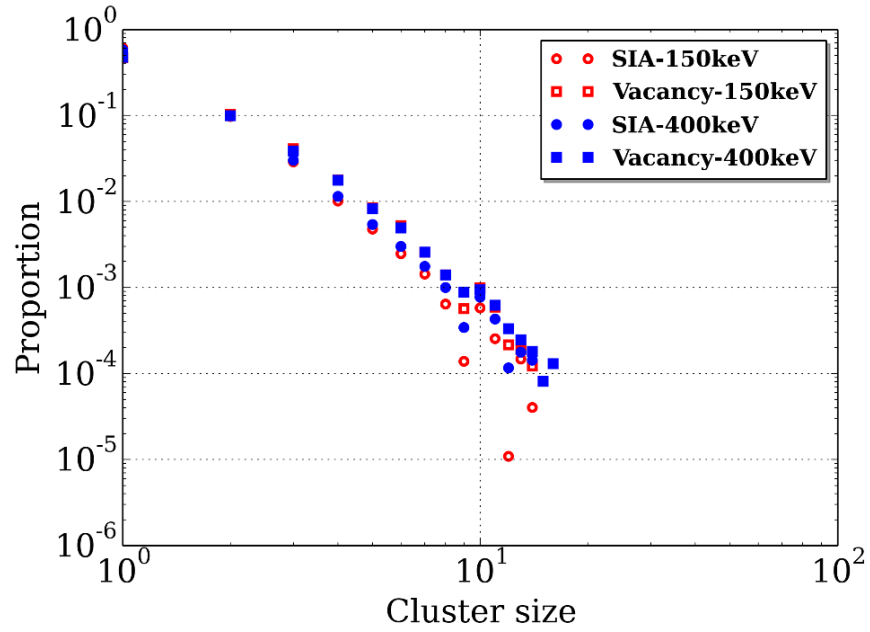
(a) MD simulations on defect cluster size distribution at 30 K during the primary damage stage of tungsten self-irradiation with another potential [178].
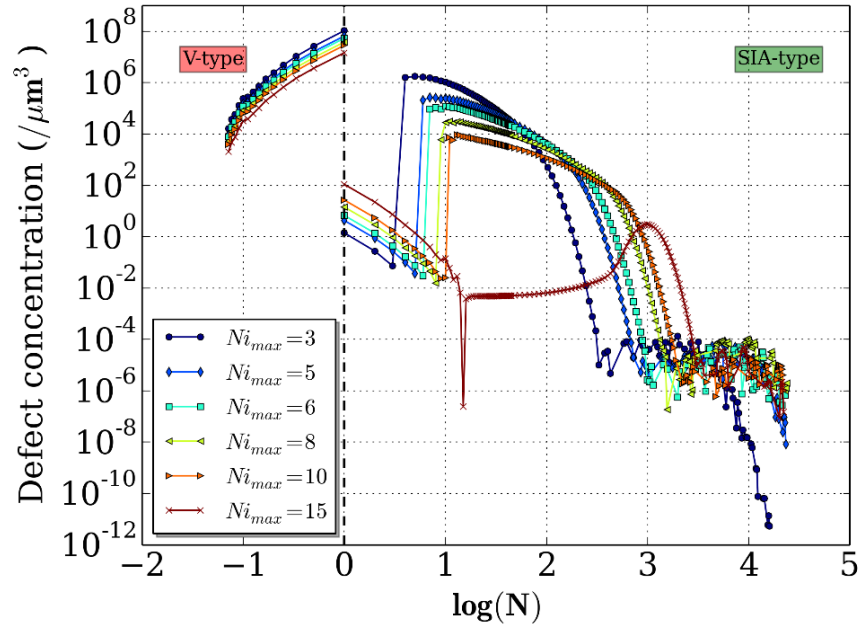
(b) Defect size distribution with different mobility constraints on the largest mobile SIA cluster. Defect production term is based on Figure 4-9a.

Figure 4-9: Effect of defect production term in CD model

4.1.3.6 Experimental comparison

These simulations model the experiments of ultra-high purity tungsten by low-dose, high-energy self-ion irradiation at 30 K performed by Yi et al. [170]. It was expected that such a low temperature offers a description of primary damage caused by individual collision cascade events, and provides direct evidence of a power law size distribution of nanoscale defects formed in high-energy cascades. However, by further examining the experimental results, the size distribution exhibits a clear deviation from the power law at longer times, which suggests that other underlying kinetics become significant even at this low temperature. Note that even with a time duration of ~ 1 s and a low temperature (30 K), SIAs and SIA clusters are still highly mobile due to extremely low migration energy barriers (~ 0.01eV). By contrast, since vacancy clusters possess high migration barriers and low attempt frequencies, only the monovacancy is considered to be mobile in the model.

Figure 4-10 shows the results of CD simulations of self-ion irradiation in tungsten, overlaid with the experimental results of [170] and the MD simulations by Sand et al. [174]. To maintain consistent units, the original figure is re-plotted after a first order approximation of defect concentration with an operation shown in Eq. 4.5. The difference between current CD predictions and the original MD simulations results from the longer timescale evolution of the defect size distribution. Sand et al.'s results highlight a size-scaling pattern in the initial stage of radiation damage (the defect production term), while longer timescale evolution may be necessary to compare against experimental data and explain the deviation from a power law. The measured defect size distribution matches very well with the CD simulations in this study. This implies that additional SIA kinetics play an important role in defect evolution beyond the MD timescale, even at such a low temperature.

$$\frac{(\text{Fluence} \sim 1.25 \times 10^{16}\, W^+/m^2) \times (\text{Frequency per ion})}{(\text{Damage depth} \sim 10\, nm)} \qquad (4.5)$$
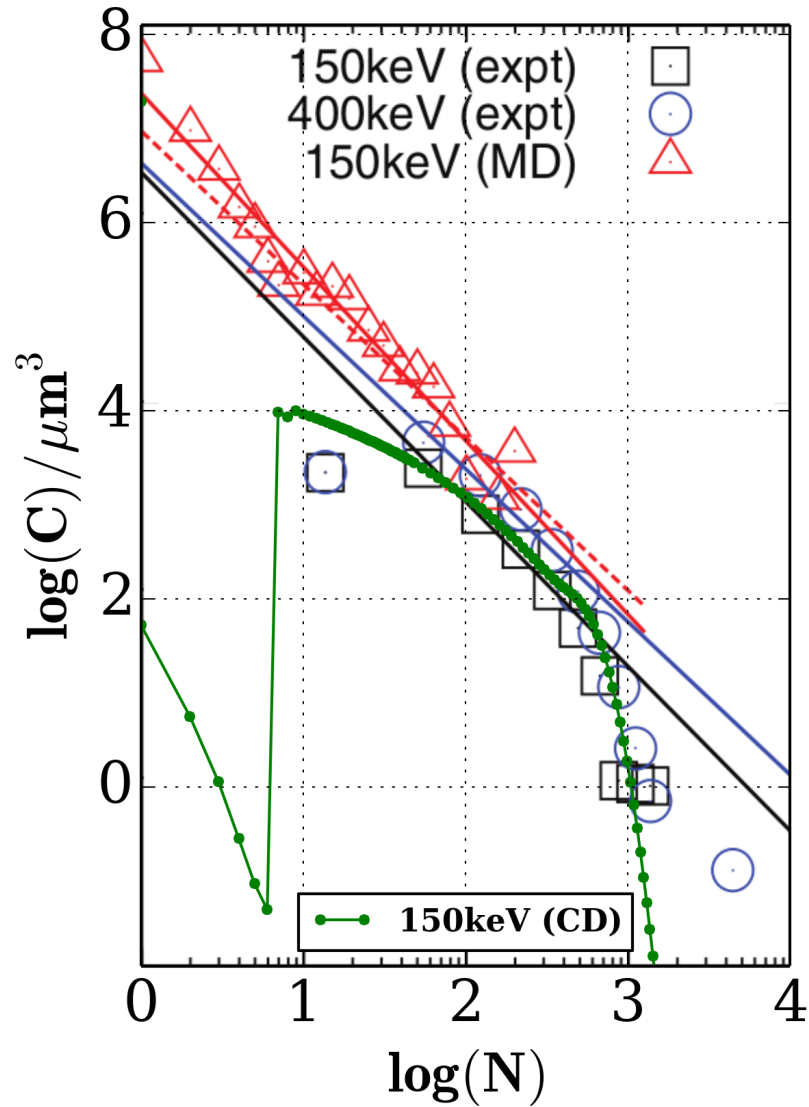
Figure 4-10: Defect cluster concentration as generated by MD simulations [174], rate theory calculations (this work), and experimental measurements [170].

4.1.4 Discussion

Because defect clusters usually become increasingly stable with size, and multiple self-interstitial atom (SIA) cluster sizes are mobile, one would not expect a true power law to evolve in this case, but rather a truncated version with dips from the expected power law behavior on both the large and the small ends of the cluster size distribution. Indeed this is precisely what was observed by Yi et al. [170]. This study uses a combination of simulation techniques to reach experimental timescales to reproduce the Yi et al. data regarding the defect size distribution.

Typical parameters in self-ion irradiation have been explored to extract insights regarding defect evolution behavior, including the mobility of SIA clusters (Figure 4-5), dose rate (Figure 4-6), incoming particle energy (Figure 4-7), and total dose (Figure 4-8). A number of conclusions can be drawn from the simulation results: 1) The SIA cluster mobility is very important in determining the final defect size distribution. An upper limit to the mobility of SIA clusters of size six yields results very close to experimental measurements (Figure 4-10). 2) A higher dose rate limits the defects' ability to cluster into larger groups, since more annihilation of SIAs and vacancies is anticipated with less relaxation time between damage cascades. 3) Different ion energies result in different defect cluster production terms: for the higher energy case (400 keV), the amount of small clusters is greater than that of the lower energy case (150 keV). A direct explanation is that the fraction of point defects production is higher in 400 keV irradiation. 4) More clusters are expected with increasing dose, and a plateau in the total number of clusters develops across a range of doses.

The only fitting factor remaining in this study is the cutoff size chosen for the largest mobile SIA clusters (Ni_{max}). The very fact using that this cutoff delivers good agreement with experimental results indicates that the mobility of large clusters may be constrained in the system. Here one can draw inspiration from studies on the mobility of SIA clusters [189] and the drastic effect of carbon atoms (on the scale of ppm) on raising the migration barriers of point defects in Fe [190], and solute-defect

interactions in W [191, 192]. These studies lead us to believe that although some SIA clusters composed of crowdions are highly mobile, and undergo 1D motion on their glide prisms in MD simulations, SIA cluster motion in general depends significantly on cluster size, shape, and other extrinsic factors such as trapping by solute atoms and sources of internal stress, including surrounding defects and sinks. Due to the insufficient number of atomistic studies on this subject, more careful investigation on the mobility of SIA clusters is needed to confirm the explanations.

Note that MD simulations of primary radiation damage can have quite different results depending on the choice of interatomic potentials, especially for tungsten as shown by Sand et al. [193]. Compared with the current work, Sand et al.'s MD results based on Derlet et al.'s potential [183] show the production of large clusters [188, 193] with sizes around 100-200, as also indicated in Figure 4-10. It could be due to the intrinsic emphasis of the potentials, for example, Derlet et al. [183] used the family of short-range FS-type potentials to find new parametrizations for W, and applied the potential to study the thermally activated migration of SIAs in W. Meanwhile, Marinica [178] developed the EAM potential for studying radiation defects and dislocations in W. Thus, it is not feasible for us to identify the exact reason that causes the discrepancy at this time. Since the probability of capturing large clusters is rare in such simulations, it is worthy to note that in the limited number of independent simulations, it is likely that the possibility of production of large clusters is neglected. However, with various source terms, either from aforementioned potentials [177, 178] or off-the-shelf power-law fitting [188], similar evolution results can be achieved with a fitting parameter of Ni_{max}. This implies that although the exact value of Ni_{max} may change with different potentials, such a cutoff still exists in order to obtain reasonable agreement with experiments. Therefore, the mobility of large clusters may not be significant enough to matter in this case.

The CD simulations agree generally well with the available experimental observations. The MD studies of Sand et al. up to nanosecond timescales also achieve good agreement with the middle of the experimental defect cluster size distribution, while longer timescale methods such as CD may be necessary to accommodate observed

features for smaller and larger cluster sizes. The deviation in the first experimental data point with the CD results can be explained by the infeasibility of identifying such small defects, as pointed out by Yi et al. [170]. For the largest cluster size, the stated concentration represents very few observed clusters of this size, therefore CD results are not expected to provide a perfect match with low statistics.

Finally, a more recent study by the originators of the experimental data also demonstrates excellent agreement between simulations and experiments of self-ion irradiated tungsten, by considering the additional changes to the defect size distribution from sub-cascade splitting [194]. Both studies recreate the experimental deviations from a power law size distribution, calling into question which, if any, explanation is correct. The key difference in the two explanations is long timescale microstructural evolution. In the work of Sand et al., one would expect a relatively time-invariant shape in the defect size distribution, as sub-cascade splitting occurs on the order of picoseconds to nanoseconds. In this study, the shape of the defect size distribution continues to evolve with time, as evidenced by Figure 4-8a. In Figure 4-8a, one can see that the magnitude of the defect size distribution increases continuously with increasing dose, after changing shape at very low doses. More experiments of self-ion irradiated tungsten, performed under the same conditions at different order of magnitude doses, will likely resolve this question. In other words, this represents an under-constrained validation problem, where the addition of one experimental variable, in this case time evolution of defect populations, will determine which explanation (primary radiation damage and/or kinetic evolution of smaller clusters) is principally responsible for the observed defect distribution in self-ion irradiation tungsten. Should irradiations to longer times show little to no deviation from the one-second irradiation, then the explanation of direct production in primary radiation damage will be shown to be correct. However, should the defect size distribution significantly change with continued irradiation, then cluster dynamics will have been shown to be the right tool to model this situation. Then, validation with multiple experiments can help inform the most appropriate choice of interatomic potential using shorter irradiations, as well as any hard cutoff in the largest mobile SIA cluster

size using longer irradiations.

4.1.5   Conclusion

The application of multiple simulation methods (binary collision, molecular dynamics, and rate theory) has proven to be effective in studying the long timescale evolution of radiation-induced defects in self-ion irradiated pure tungsten. Good agreement has been achieved between the defect cluster size distribution found in experiments and CD simulations, while only using the largest mobile interstitial cluster size as a fitting parameter. The deviation from power law scaling found in MD simulations can be understood from the more rapid motion of small SIA clusters. The effectiveness of the code developed in this study demonstrates its potential to be used in similar irradiation cases, and the capability to incorporate spatial dependence in future results. This in particular will allow for the explicit study of depth-dependent defects resulting from ion irradiation. The next logical extension of this CD framework is to include the effect of gas atoms such as helium, following the work of Xu et al. [195], Golubov et al. [196], and Marian and Hoang [197], so that more realistic and varied cases may be studied.

4.2 Spatial dependent defect evolution in Fe

Ion irradiation has been commonly used as a surrogate to neutron to interrogate material response within a short time span. By contrast, ion irradiation with directional particle beam leads to defect production with significant spatial dependence from the primary damage state. This feature brings about spatial dependent microstructure evolution. This section progresses on top of the classical mean-field rate theory as presented in Section 4.1, and use cluster dynamics to explicitly tackle the spatial and temporal defect evolution in self-ion irradiated Fe.

4.2.1 Introduction

The spatial and temporal variation of radiation damage leads to non-uniform evolution of microstructure, such as swelling, hardening and segregation. Atomistically, spatial arrangement of displaced atoms is crucial in determining the defect production efficiency or evolution pattern. Computationally, on top of MD simulations of the damage cascade, KMC is able to resolve the 3D spatial correlation of objects in the system including point defects, clusters, and impurities. On the other hand, using the theory of chemical reaction kinetics, the evolution can be modeled in continuous space by constructing a set of differential equations to describe the chemical concentrations of all defect species in the system. Ignoring the stochastic nature of the system, chemical master equations (MEs) are a mesoscropic description of kinetics with rate coefficients from transition state theory. Although on the atomistic level, the time evolution of a system can be well-characterized by molecular dynamics and Monte Carlo simulations, the tracking of whole system evolution can become computationally prohibitive. Therefore, the application of MEs gains popularity in recent years. The classical MEs assumes 1) the system evolves deterministically, i.e. the volume is large enough such that the atomistic fluctuation can be safely ignored; 2) the system the well-mixed via diffusion or constant stirring [26]. The development of formulation based on the point defect/cluster dynamics has been useful in explaining multiple phenomena where the role of spatial dependence with the experimental set-

ting is not dominant, such as bubble coarsening [198], irradiation growth [199], and electron/neutron irradiation [200].

Although classical rate theory assumes the concentration of species is homogeneous, the spatially dependent factors such as the production of defects, inhomogeneous microstructure, and surface effects, necessitates an appropriate treatment of spatial dependence in MEs. Typical examples are heavy ion implantations and thin film experiments. Figure 4-11 highlights the features of material response considering heavy ion implantation and surface effects in thin film, respectively. As current implementation of CD is based on finite element method, any spatial-varying quantities and diffusion process can be conveniently incorporated. The model is adapted to describe the cluster evolution in pure iron subject to self-ion irradiation. By extracting the final distribution of defect clusters and calibrating against experimental observations [201], some key understandings can be inferred and predictions can be made for the response due to long term irradiation.
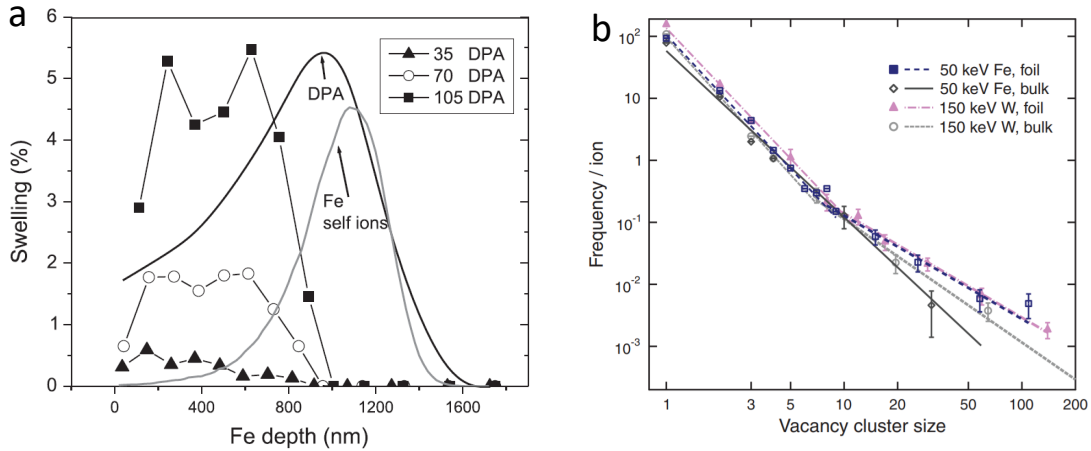
Figure 4-11: (a) Depth dependent of void swelling curve and distribution of deposited Fe ions in pure Fe with 3.5 MeV self-ions to various peak damage level [201]; (b) Distinctions between distributions of vacancy clusters from MD damage cascade simulations in bulk and thin foil (Fe and W, with PKA energy at 50 and 150 keV) [188].

4.2.2   Methods

The same implementation and formulation of coefficients of the CD model as introduced in the tungsten study (Section 4.1) is utilized. However, here we emphasize the

spatially dependent defect production in the self-ion irradiation of Fe. To precisely generate the source term for all defect clusters, the following scheme is employed (Figure 4-12): (i) use SRIM to generate vacancy production and ion deposition for the prescribed 100 bins across the 1D implantation range; (ii) extract PKA energy spectra from SRIM output for each bin; (iii) calculate overall cluster size distribution for each bin, by aggregating PKA spectrum and cluster distribution from MD simulations of PKAs at various energies in discretization; (iv) use the source term for defect clusters into CD model and evolve the system using parameters consistent with the experiments. It is worthy to note that such spatial dependence can not resolve the spatial correlation between defects, thus it has been controversial on the importance of such issue in influencing long term defect evolution. Argument goes to that whether KMC is necessary to anneal the defective systems generated from MD simulations to dilute the correlations before CD calculation is performed. In this study, such issue is neglected for simplicity, which may call for further confirmation.
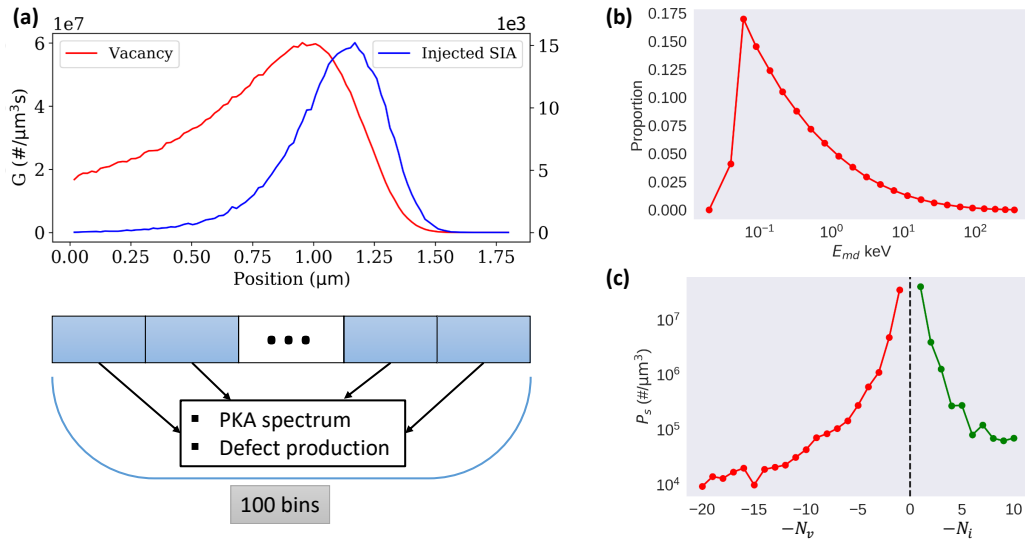
Figure 4-12: (a) shows the vacancy production and injected ion deposition rates based on the output from SRIM simulations with 10,000 ions and experimental conditions in [201]. For each bin across the depth (100 bins in total), PKA spectrum and consequent defect size distribution from the primary damage stage can be acquired by incorporating MD simulations of cascades. (b-c) Example of the PKA spectrum and the defect size distribution in the peak damage bin (around 0.9 μm).

To acquire cluster size distribution for each bin, use bin i with defect production

rate N_i as an example,

$$h(s) = \frac{\int_E g(s; E) N(E) f(E) dE}{\int_E N(E) f(E) dE} \qquad (4.6)$$

where $h(s)$ is probability of a defect in cluster size s, $f(E)dE$ is the probability of a PKA with energy in $[E, E + dE]$, $g(s; E)$ is the probability of a defect in cluster size s resulting from PKA with energy E, and $N(E)$ is the total point defect production from PKA with energy E. Note that the following normality conditions are satisfied.

$$\sum_s h(s) = 1 \qquad (4.7)$$

$$\sum_s g(s; E) = 1 \qquad (4.8)$$

$$\int f(E) dE = 1 \qquad (4.9)$$

Therefore, the production rate of cluster size s at bin i, denoted as $P_i(s)$,

$$P_i(s) = \frac{N_i h(s)}{s} \qquad (4.10)$$

If $g(s; E)$ is approximately PKA energy independent as proposed by Souidi et al. in iron [202], then it follows that,

$$g(s; E) = g(s) \qquad (4.11)$$

$$h(s) = g(s) \qquad (4.12)$$

MD cascade annealing simulations using PKA energies across energy spectrum have been performed and the defect size distribution is calculated based on Eq. (4.6)-(4.10). Figure 4-12(c) demonstrates an example, by setting the maximum vacancy and interstitial clusters to 20 and 10, respectively. Notice that larger sizes exist with statistical fluctuation, but are neglected as rare events. In the CD model, diffusion across the bins is considered for mobile species with pre-calculated coefficients based on Arrhenius law. The physical parameters are listed in Table 4.3-4.4, with capillary

140

approximation for the binding energies of large cluster sizes. The maximum size of mobile vacancy cluster is 2, and interstitial cluster is 4. The migration dimensionality is 3D for both types. Boundary values for all defect species are assumed at thermal equilibrium, and are mostly approximated to be zero.

Item	value	comment
Defect production efficiency	0.25	Assumption
SIA (cluster) migration energy (eV) (1,2,3,4)	0.34,0.42,0.43,0.43	3D
Vacancy (cluster) migration energy (eV) (1,2)	0.67,0.62	3D
Diffusion pre-factor ($\mu m^2/s$)	8.2×10^{-7}	N/A
SIA (cluster) bias factor	1.15	N/A
Vacancy (cluster) bias factor	1.0	N/A
Dislocation density ($/m^2$)	1.0×10^{14}	N/A
Atomic volume (m^3)	1.165×10^{-29}	N/A
Defect reaction distance (nm)	0.66	Assumption

Table 4.3: Parameters used in cluster dynamics for Fe (PART I) [30,203].

SIA binding energies (eV)		Vacancy binding energies (eV)	
Size (n)	$E^b_{SIA}(n)$	Size (n)	$E^b_v(n)$
2	0.8	2	0.3
3	0.92	3	0.37
4	1.64	4	0.62
>4	Capillary approximation [a]	>4	Capillary approximation [a]
a. $E^b(n) = (E^b(2) - E^{for}(1))\frac{n^{2/3}-(n-1)^{2/3}}{2^{2/3}-1} + E^{for}(1)$			
with formation energy $E^{for}(SIA) = 3.77\,eV$ and $E^{for}(V) = 2.07\,eV$			

Table 4.4: Binding energies used in cluster dynamics for Fe (PART II) [30,203].

4.2.3 Results

4.2.3.1 Defect evolution

Calculations utilize the same irradiation setting as in the experiment, i.e. 3.5 MeV Fe^{++} self-ion irradiation in pure Fe, at 450 °C, peak damage rate at 7×10^{-4} dpa/s. Figure 4-13 plots the defect size distribution at the peak damage region (around 900 nm) at various doses. It can be seen that the high mobility of small interstitial clusters ($n < 5$) quickly leads to the quasi-equilibrium distribution for interstitial clusters, which builds increasing density at smaller sizes ($n \leq 100$) as the dose increases. It implies that the large clusters have reach a balance between growth from interstitial

clustering and shrinkage from vacancy recombination. On the other hand, the distribution of vacancy clusters keep evolving: the second peak appears from around 1 dpa and then gradually moves to large sizes. The dip at $n \sim 100$ marks a void nucleation barrier, and the left peak indicates void growth. For these mobile defects, the decline of their concentrations is expected due to the active reaction network.
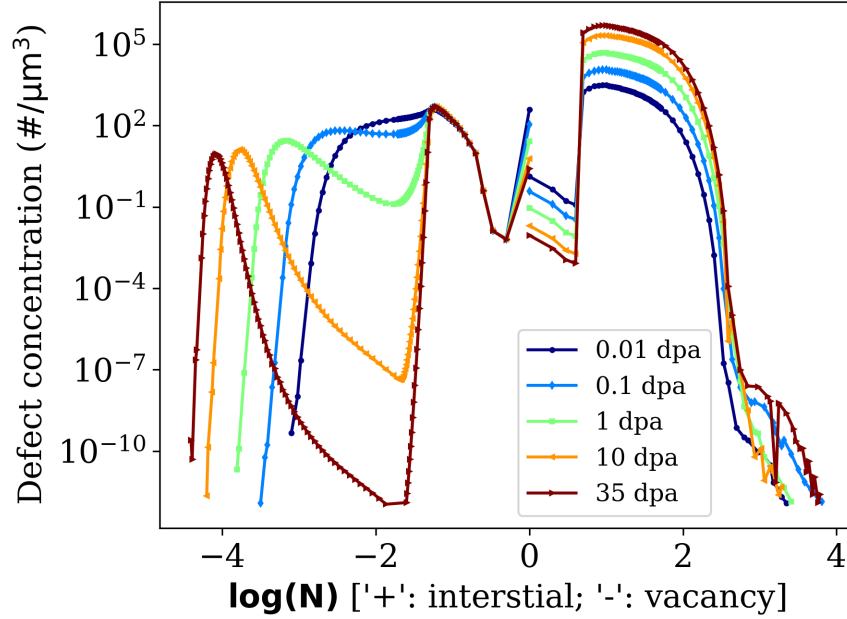
Figure 4-13: Calculated defect size distribution in the peak damage region at various doses with dose rate at 7×10^{-4} dpa/s. "-" denotes vacancy type and "+" for interstitial type clusters. The appearance of double peaks in vacancy cluster distribution indicates the nuclear barrier of void growth.

4.2.3.2 Dose rate dependence

The dose rate effect can be easily examined by scaling the defect production rate. Figure 4-14 shows the results by setting the dose rate one magnitude higher than that in Figure 4-13. The interstitial cluster distribution demonstrates similar results in terms of shape and quantity. Therefore, the increase in defect production doesn't influence the quick build-up of the quasi-equilibrium distribution. The additional interstitial-type defects can be effectively removed by vacancy clusters and dislocations. In comparison, the evolution of vacancy cluster distribution slows down. The

second peak starts to form from 1 dpa and the concentrations of mid-sizes ($n \sim 100$) gradually slump. Such phenomenon can be understood from the defect dynamics. Due to the high defect production rate, two consequences are expected: i) less time is allowed for vacancy clusters to grow, and defect recombination is enhanced. ii) once the void nucleation barrier is passed, the growth of vacancy clusters becomes very efficient with higher quantity than the low dose rate case.
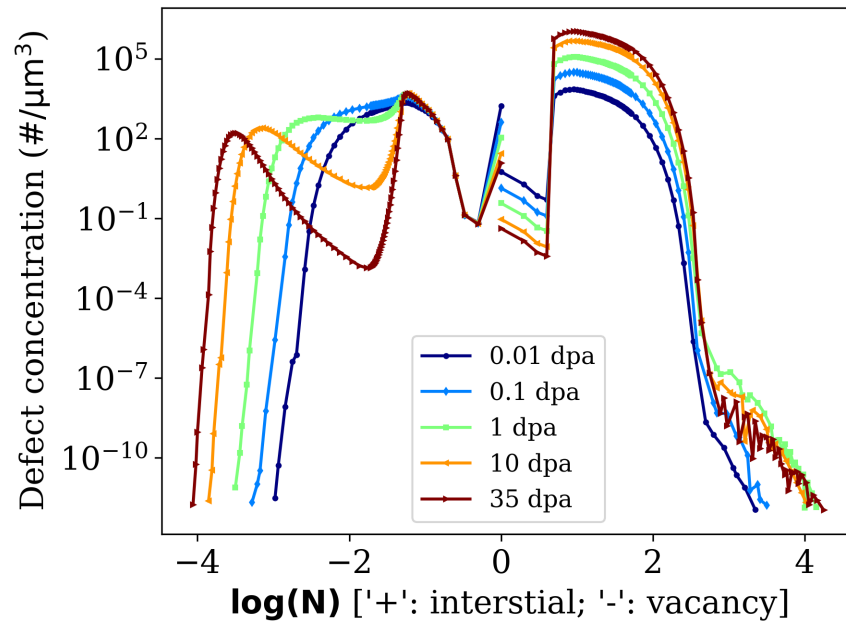
Figure 4-14: Calculated defect size distribution in the peak damage region at various doses with dose rate at 7×10^{-3} dpa/s. "-" denotes vacancy type and "+" for interstitial type clusters. The appearance of double peaks in vacancy cluster distribution indicates the nuclear barrier of void growth.

4.2.3.3 Comparison with experiment

Figure 4-15(c) compares the calculated void swelling with the experimental results at three different doses. It can be seen that the profile, although on the same magnitude with the measurement, fails to capture the suppression of void swelling near the peak damage region. The injected interstitial may enhance local defect recombination and reduce the driving force to form voids [201]. The inconsistent simulation results are because the injected interstitials amount to a little part ($\sim 10^{-4}$) of the calculated

defect size distribution for interstitials and even the statistical variation can submerge this negligible effect from the injected interstitials. The calculation results call the model feasibility into question for high dose rate ion irradiation scenarios where effects including injected interstitials, overlapping damage cascades, and interaction between the cascade and pre-existing defects may play a significant role in dictating microstructure evolution.
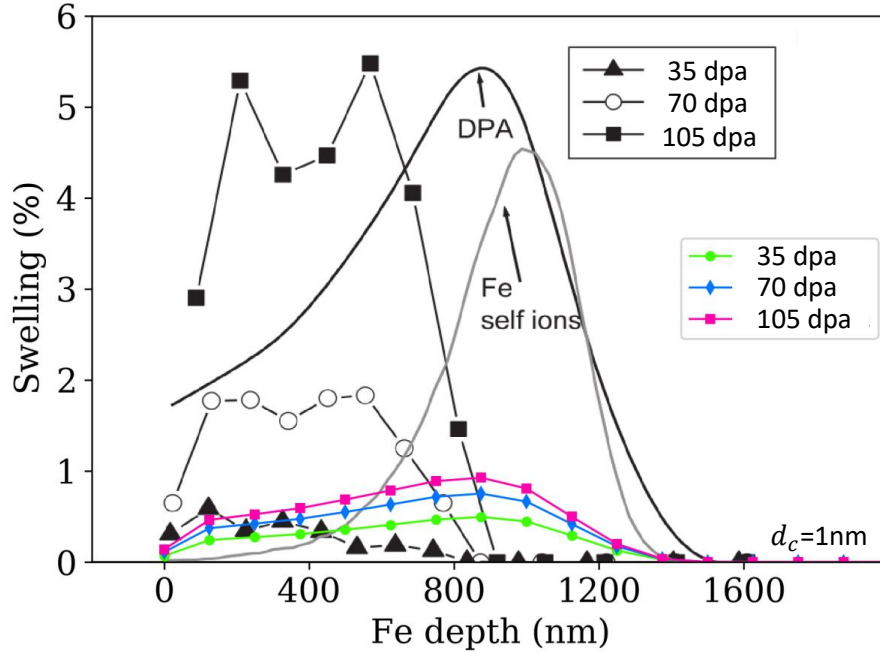
Figure 4-15: Comparison of the void swelling curves from calculation and experiment. d_c denotes the cutoff minimum size used in aggregating defect size distribution into swelling percentage in order to mimic TEM resolution in the experiment [201].

4.2.4 Discussion

Application of multiscale methods to describe the spatial dependence resultant from surface effect, defect production, and heterogeneity of microstructure provides high resolution in examining material long term behavior with various convolving factors. This physics-based technique renders an efficient approach to computational material design by extrapolating well-calibrated robust models to the domain beyond experimental parameter space. The results can effectively both guide and complement experiments.

In this work, the self-ion irradiation in pure Fe is examined by considering the spatial dependent defect production. Information passing along the multiscale methods, i.e. BCA-MD-CD, enables system evolution on the experimental scale. The extraction of defect size distribution reflects void nucleation and growth, nevertheless, the calculated void swelling curve cannot reproduce the experimental measurements. It may be due to omission of important process such as interaction between cascades and pre-existing defects which would modify the effective defect production term in the CD model. This can possibly be solved by tweaking the efficiency of defect production along the depth to account this effect. Increasing the dose rate, equivalent to raising the beam current density, allows less time for vacancy clustering, which leads to slow evolution of vacancy cluster distribution.

Generally, CD modeling can flexibly treat the chemical rate based phenomenon, such as growth of dislocation and void. The results can be linked to the quantities describing mechanical property and void swelling. With the inclusion of spatial dependence extended from classical mean-field homogeneous assumption, one can study ion implantations, thin film irradiation, and inhomogeneous microstructure specimens. Good agreement has been achieved in various studies [28, 31, 32, 204]. However, blindly applying this scheme can generate contradictory results. A common but controversial practice would be to use some metric such as experimental observations to calibrate the choice of model inputs, which naturally contributes to the final agreement. For example, Michaut et al. [205] utilized CD to examine the effect of injected interstitials on loop and cavity microstructures, and agreement with experimental data can be achieved by tweaking defect source terms and fraction of freely migrating interstitials. As a parameter-rich modeling problem, the tunning of parameters can be exponentially computation intensive and fade the physical understanding. On the other hand, various assumptions are necessary to construct the formulation for interaction between objects, such as binding energy and sink strength. These assumptions, although admitting physical understanding of the process, are an idealization of defect property. In fact, the behavior of a defect may well be influenced by the local environment such as stress. Moreover, a single size of defect can

145

bear different configurations under the highly non-equilibrium radiation condition, thus migration characteristics [25] and interaction strength may vary significantly, which means that a representation only with the size information could neglect some key underlying processes in understanding the problem. Such complexity can hardly be resolved due to the intractable configuration evolution of defects in the massive reaction network. Meanwhile, some other settings may be subject to skepticism. For example, carbon-vacancy binding can increase the migration barrier [204]; cutoff of defect source term neglects the rare events of large defect production from primary damage stage; the maximum mobile defect clusters may exclude even larger ones with high mobility. All these issues raise concern to the model robustness. A future exploration of the applicable scenarios is needed. Furthermore, if we consider a complex system with more defect sinks such as precipitates, interfaces and surface effects, a simple CD model as demonstrated here is not capable to describe realistic conditions.

4.3 Summary

In this chapter, a multiscale framework composed of atomistic methods and cluster dynamics is constructed to describe defect evolution up to the experimental level. In the case of self-ion irradiated tungsten at 30 K, the system evolution beyond damage cascades can well explain the deviation from power law in the interstitial size distribution. To incorporate the spatial dependent defect production in ion irradiation, the self-ion irradiated iron is considered, by dividing the 1D domain into a number of bins. The defect production from primary damage state is obtained for each bin. By evolving the system to the desired dose, the spatial varying defect species concentration can then be combined and transformed into void swelling. The calculated swelling curve is comparable with experimental measurement but misses a key feature of swelling suppression at the peak damage region. Such misfit underlies some potential issues such as volume relaxation of the size representation, and necessary change for the defect production term due to interaction of cascades and pre-existing defects. Overall, this combination of methods can be capable of predicting defect evolution with careful calibration against experiments.

It should be emphasized that in realistic systems, the multiscale framework can get rather complicated. First, the size representation is limited due to the degeneracy of multiple defect configurations, which may embrace very distinct properties. Second, the parameter for interaction, such as changeable diffusion dimensionality of defects and localized diffusion barriers can be intractable in simulations. Finally, additional dynamics may play an important role in modifying defect evolution. Examples are the segregation of constitute atoms, dislocation dynamics, and variable defect sink properties. These complexities can potentially be lumped together by developing reduced-order models, or with even more simplification, applying data-driven approach without probing deep into physics. In the next chapter, such data-driven idea is elaborated by a specific application in void swelling.

Chapter 5

Data-driven prediction in nuclear materials

Physics-based computation techniques provide sound details towards certain physical processes such as defect cluster nucleation and growth (e.g. Section 4.1), but the complexity quickly builds up considering additional coupled processes such as constitute atom migration, phase instability, and dislocation dynamics. Meanwhile, the multiscale nature of these coupled processes poses a gruesome barrier to describe material behavior with high fidelity. Recently, with the advancement of machine learning techniques based on increasing amount of data, new insights can be gained without probing deep into the physics. This section uses one example of void swelling to demonstrate the idea. Such problem has been around the nuclear community for over tens of years, but still remains to be better understood due to its complexity from a number of confounding factors in real materials systems.

5.1 Predict the onset of void swelling

5.1.1 Introduction

Void swelling, which causes significant mechanical property degradation and dimensional changes, has long been reported in structural materials of nuclear reactors

[206, 207]. Swelling with respect to radiation dose can be divided in two stages: transient and steady-state [1], while the intercept value of the linear, steady-state swelling rate is termed the "incubation dose" (onset of void swelling). It has been found that the incubation dose of specific materials can be influenced by both internal and external factors such as crystal structure, solutes, microstructure, temperature, dose rate, irradiation type, and stress state [1]. This causes the incubation dose to vary significantly from nearly zero to over 400 dpa.

The conventional development of radiation-tolerant materials relies heavily on trial and error. Optimization with the goal of increasing the incubation dose can be made by empirically tuning the material's thermo-mechanical treatment and chemical composition [1]. However, this process is very costly and time-consuming due to the requirements of careful sample preparation, specific radiation conditions, resource-intensive post-irradiation examination (PIE), safety concerns from radioactivity, and the need for repeatability. Computational efforts are aimed to bridge this gap, as well as provide a more fundamental understanding of the origins of void swelling. Simulations should ideally capture all governing physical processes on multiple length and time scales, which include defect production, diffusion, annihilation, absorption, trapping, and coalescence. The simulation of radiation damage has never been a trivial task, and high uncertainties can arise when linking multiscale methods together to describe a material's macroscale response [208]. Realistic scenarios such as the presence of gas atoms [209] and minor alloying elements [210] further complicate the accurate description of radiation-induced microstructural evolution. Due to their intrinsic complexities, numerical studies excluding some important processes such as dislocation dynamics and defect-solute binding can still be time-consuming [211]. On the other hand, simulation parameter calibration is usually performed to match experimental observations [204], which decreases the predictive ability of simulation results. Therefore, both experimental measurements and computational efforts are often incapable of satisfying the practical requirement to efficiently assess the onset of void swelling for a particular material, thus hastening the development of radiation-resistant nuclear materials.

Recently, the increased utilization of machine learning (ML) has benefited material science research in many successful applications such as predicting glass transition temperatures in polymers [212], rapid material discovery with failed experiments [213], and structural optimization [214]. Given enough data, ML may also prove effective in computational modeling [215] and design of nuclear materials. Some initial efforts on using artificial neural networks to predict embrittlement and harening of reactor pressure vessel [216, 217], and Charpy transition temperature of martensitic steel [218] have demonstrated quite promising results. ML could therefore possibly accelerate the screening of new materials for specific property like increased void swelling incubation dose. It should be noted that the success of ML is contingent upon access to enough data. Fortunately, over the last few decades, numerous results on testing different materials under various experimental conditions have been accumulated on void swelling, but are unfortunately dispersed in various publications and technical reports. These experimental efforts, when combined in a ML framework, can synergistically generate significant insights towards radiation-resistant material design.

ML learns the hidden relationships embedded in data by minimizing a "cost function." By training a model with a portion of the available data, and evaluating its performance with the rest, ML can effectively uncover the underlying rules that facilitate prediction in the huge, unexplored parameter space. Figure 5-1 depicts the common steps in the application of ML, which include problem identification, data preparation, modeling, evaluation, and deployment (left panel of Figure 5-1). To illustrate the process in the context of radiation damage (right panel of Figure 5-1), two aspects are specifically sought: i) prediction of radiation effects (e.g. incubation dose for void swelling), and ii) discovery of new materials with superior radiation performance. As the quantity and quality data is the foundation of any successful ML application, data preparation including collection, pre-processing, and feature engineering usually takes most of the effort in the process. By contrast, model training is already well-integrated into many calculation packages, such as $scikit-learn$ for general methods [219] and $tensorflow$ specializing in neural networks [220]. These are readily applied to specific problems, which usually fall into two categories: super-

vised or unsupervised, where the former has a well-defined target to predict, and the latter draws inferences from datasets without labeled responses. Evaluation is mostly incorporated into the modeling process, and provides guidance to model selection based on defined metrics such as classification accuracy and mean squared error. Rounds of iterative refinement may be necessary to achieve better performance. Finally, the learned model can be validated with previously unseen data. If the model is non-parameteric, which requires the usage of training data in deployment, the model would need to be continuously updated with newly available data, and become computationally expensive with increasing amounts of data. On the other hand, if the model can be summarized in a parametric form, its off-line application is compactly transferable across platforms and requires no access to used data until the model goes stale and needs re-training.
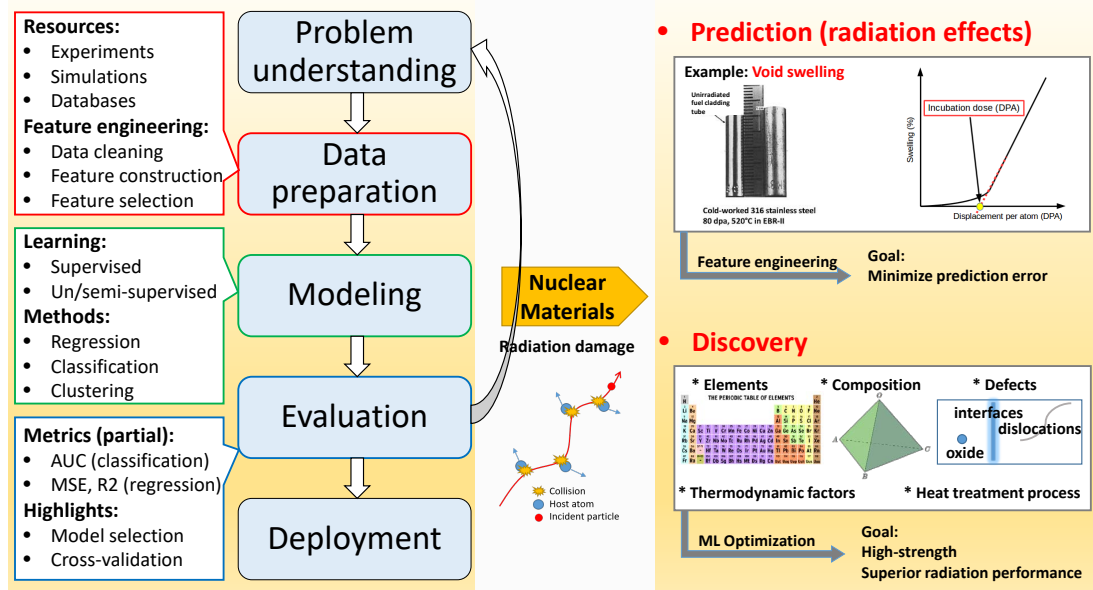
Figure 5-1: Application of machine learning (left half) to nuclear materials (right half) for i) prediction of radiation effects (e.g. incubation dose for void swelling [221] in metals), and ii) discovery of new materials with superior radiation performance. Insights can be gained from the identification of meaningful features, such as chemical composition and microstructure, and patterns in the increasing amount of experimental data. (AUC: area under the curve; MSE: mean squared error; R2: R-squared).

This work explores the capability of ML to predict the onset of void welling using material and environmental parameters such as chemical composition, temperature,

microstructure, and type of radiation. By manually collecting experimental data from a large number of publications, ML is shown to be effective in predicting the incubation dose of void swelling. The identification of controlling factors in the learned model not only generates results consistent with the established understanding of key parameters, but also provides additional, meaningful insights into radiation-resistant material design.

5.1.2 Methods

In this supervised regression ML problem, the investigation starts with data collection and feature engineering, then applies three types of learning techniques, i.e. linear regression (LR), tree-based ensemble methods, and artificial neural networks (NN), and finally interprets the associations inferred from the models.

5.1.2.1 Dataset

Studies on this topic often contain profiles of void swelling with respect to radiation dose, corresponding to the specific experiment performed. With such profiles, one can extract the value of the incubation dose by extrapolation of the linear, steady-state void swelling regime to the horizontal axis as indicated by Figure 5-1 in the upper-right panel. The aim of data collection is to capture all these features along with other potentially influential variables. TABLE 5.1 provides a subset of the data used, which contains 28 raw features and 305 samples from surveying different resources and filtering records. Nevertheless, there are still some unknown entries due to qualitative, literal descriptions and technical measurement limitations. Not all parameters are measured, are documented, and/or receive attention in each study. For example, many earlier experiments omitted the measurement of dislocation density, which later proved influential. Instead, more natural language descriptions such as "annealed," "20% cold worked," and "quenched" are commonly used. These expressions to some extent imply order-of-magnitude dislocation densities following thermo-mechanical treatment. With proper language processing by referring to more recent measure-

153

ments with the same terminology, these values are estimated to fully populate the dataset. Data and corresponding references [90, 222–255] are available at [256] for those who are interested.

Material	Crystal structure	Chemical composition	Dose rate (dpa/s)	Temperature (K)	Irradiation type	Dislocation density (m^{-2})	Pre-injected helium (appm)	Incubation dose (dpa)
316 steel	FCC	...	8.0x10^{-3}	753.5	Electron	6.1656x10^{14}	0	18.5
Fe-15Cr-16Ni	FCC	...	1.7x10^{-6}	673.5	Neutron	N/A	0	27.1

Table 5.1: Representative subset of the dataset used in this study, showing two of the 305 records. Chemical composition is a placeholder for 21 elements: Fe, Cr, Mn, Si, Co, Mo, Ni, C, Ti, N, B, P, S, Nb, Cu, Ta, Al, V, Mg, W, Zr.

Feature	Mean	Min	Max	Feature	Mean	Min	Max
Fe(wt%)	63.04537	0	97	Nb(wt%)	0.01718	0	0.92
Cr(wt%)	15.52098	0	24.7	Cu(wt%)	0.013836	0	0.54
Mn(wt%)	0.852059	0	20	Ta(wt%)	0.006098	0	0.36
Si(wt%)	0.291846	0	1.5	Al(wt%)	0.334885	0	100
Co(wt%)	0.003564	0	0.04	V(wt%)	0.039525	0	2
Mo(wt%)	0.890525	0	2.95	Mg(wt%)	0.036131	0	1.63
Ni(wt%)	18.73234	0	100	W(wt%)	0.065639	0	2.4
C(wt%)	0.05848	0	1	Zr(wt%)	0.002492	0	0.1
Ti(wt%)	0.076557	0	2.2	Dose rate[dpa/s]	0.001551	8.90x10^{-9}	0.06
N(wt%)	0.008082	0	0.3	Temperature[K]	773.0538	393.5	1013.5
B(wt%)	0.000276	0	0.004	Dislocation density (m^{-2})	6.92x10^{14}	3x10^{13}	3.85x10^{15}
P(wt%)	0.006497	0	0.155	Pre-injected He (appm)	2.691803	0	100
S(wt%)	0.001062	0	0.03	Incubation dose[dpa]	43.61691	0	492

Table 5.2: Summary of numerical variables in the dataset.

In the dataset, all features except the radiation type and crystal structure are numerical, with last column "incubation dose" being the target variable. The numerical variables are summarized in Table 5.2. To incorporate non-numerical values into the model, "one hot encoding" is used which introduces additional binary features to distinguish each category. After filling in all the missing entries based on physical descriptions, normalization is performed on each column so that large quantities do not dominate the learning process. The final dataset is of dimension 305×30 including

the target column.

5.1.2.2   Regression models

The application of these regression models is based on the $scikit-learn$ 0.19.1 python package. The prediction performance is quantified using the mean squared error (MSE). After random shuffle of the whole dataset, the first 80% of the dataset is reserved for training, and the remainder for testing. As each method contains certain tunable parameters which influence predictive performance, k-fold cross-validation is used for parameter selection. In other words, for any specific set of parameters, the training set is first randomly split into k groups; then a total of k passes are made, each of which uses one group for cross validation and the remaining $k-1$ groups for training. Finally, the average performance is reported for comparison. This technique can enable us to make full use of the small dataset and avoid a "lucky-split," where a particular split of the full dataset just happens to give an anomalously good prediction during cross validation.

1. Linear regression

   The simplest model is a linear combination of the D input features in $\mathbf{x}$ with weighting coefficients $\mathbf{w}$:

   $$y(\mathbf{x}, \mathbf{w}) = w_0 + w_1 x_1 + \cdots + w_D x_D = w_0 + \mathbf{w}^T \mathbf{x}$$

   where $\mathbf{x} = (x_1, \cdots, x_D)^T$ and $\mathbf{w} = (w_1, \cdots, w_D)^T$. This class of models can be extended by considering a linear combination of non-linear functions of the features. In order to control overfitting, a regularization term $E(\mathbf{w})$ is added to the error function, thus the total error to be minimized takes the form:

   $$\frac{1}{2N} \sum_{n=1}^{N} (t_n - \mathbf{w}^T \mathbf{x} - w_0)^2 + \lambda E(\mathbf{w})$$

   where N is the number of data points, t_n is the real target value, and λ is the regularization coefficient that controls the relative importance between the data

dependent error and the regularization level. Two common forms of $E(\mathbf{w})$ i.e. Ridge ($\frac{1}{2}\mathbf{w}^T\mathbf{w}$) and Lasso ($\sum_{n=1}^{D}|w_n|$) are mixed with a tunable parameter to control the contribution of each while minimizing the total error function. For this study, the ratio between the two forms are optimized.

2. Ensemble methods

Ensemble methods are based on the notion that prediction can be improved by a combination of a number of base learners [257]. Forests of randomized trees and boosting are two main types of techniques that belong to the genre. The former contains a number of decision trees built with different sub-samples of the training data drawn with replacement, and uses averaging to control overfitting and improve prediction. The tree is constructed by splitting the nodes among a random subset of the features. Based on the difference in the splitting rule, two algorithms including random forests (RF) [258] and extremely randomized trees (ET) [259] are used. Due to the randomness, the bias of the forest is slightly higher than a single tree, but the variance decreases by averaging, which generates an overall better model.

By contrast, boosting differs from the forests of randomized trees in that the weak learners (e.g. shallow decision trees) are trained in sequence rather than parallel. Each learner is trained using a weighted form of the data, where the weighting coefficient associated with each datum depends on the performance of previous learners. Specifically, points which are incorrectly classified in a previous step gain increased weights in the current round. In this way, each subsequent learner is thereby forced to emphasize the data missed by the previous learners. Gradient boosting (GB) is a generalization of boosting to arbitrary, differentiable loss functions [260], which has proven effective in both regression and classification problems.

For this regression problem, the main parameters for optimization are the number of decision trees and tree-depth. Meanwhile, all these ensemble methods can generate an estimate of feature importance towards the accuracy of predictions,

which can be readily used for feature selection and model interpretation.

3. Artificial neural network

   The artificial neural network is a powerful and versatile method inspired by biological neural networks for learning complex problems, and the theoretical framework is thoroughly described by Bishop [261]. It is a framework with three type of layers: input, hidden, and output layers, each containing a number of neurons connected with those in neighboring layers. The edges between neurons are associated with weights, which are updated through back-propagation as the learning proceeds. Typically, the hidden layers can be constructed in a multiple layer approach with varying neuron numbers to optimize during network construction. The input to each neuron is then a linear, weighted summation of the outputs of neurons in the previous layer, while the output is the result of a non-linear activation function operating on the sum. Depending on the problem, the output layer can be a scalar value or a multi-output vector.

   In this application, the input layer uses the features, while the hidden layers contain two layers with 100 and 50 neurons, respectively. Parameter optimization is focused on the activation function, and on early stopping which controls overfitting. The output layer has a single neuron yielding the prediction. Overall, the network tries to minimize the total mean squared error. Information transmits forward from the input layer to the last layer, and the ultimate output is simply a weighted aggregation of the last hidden layer with no activation applied in the output layer.

5.1.2.3   Parameter searching

ML models often carry a number of parameters that can influence the performance of the model and/or control the level of overfitting. In this study, a few such important parameters are optimized such as the regularization level in the LR method, the number of trees in the ensemble methods, and the activation function in NN, while leaving more parameters such as learning rate as the default values in the

$scikit - learn$ 0.19.1 package. Determination of these varying parameters is based on the grid search cross-validation using the k-fold technique. The search examines all combinations of proposed values, evaluates the average predictive performance on the out-of-sample data group for each setting, and reports the optimal choice. Therefore, computation time increases exponentially with more parameters considered. Since the dataset at hand is relatively small with many features, it is found that different training-test dataset splits can result in different optimal parameter selection. To accommodate this inconsistency, we can run multiple splits and record the most frequent parameter combination provided by the grid search, which is finally used in the deployment of models on the test set. In this way, it is most likely to avoid misleading parameter optimization due to data sampling. TABLE 5.3 lists the optimized settings in this study, with the notation conforming to the python package.

Model	Linear regression	Neural network		Gradient boosting		Extra Trees		Random forests	
scikit-learn 0.19.1 Function	linear_model .ElasticNet	neural_network.MLPRegressor		ensemble.GradientBoostingRegressor		ensemble.ExtraTreesRegressor		ensemble.RandomForestRegressor	
Parameter	l1_ratio	activation	early_stopping	n_estimators	max_depth	n_estimators	max_depth	n_estimators	max_depth
Value	0.0	relu	False	500	5	800	7	50	7

Table 5.3: Optimized parameters for different methods in scikit-learn 0.19.1.

5.1.3 Results

5.1.3.1 Data exploration

Before modeling, it is useful to check the correlation $\rho(u, v)$ between all pairs of numerical variables, defined as:

$$\rho(u, v) = \frac{(u - \bar{u})^T (v - \bar{v})}{\sqrt{[(u - \bar{u})^T (u - \bar{u})][(v - \bar{v})^T (v - \bar{v})]}}$$

where u and v each denote a feature column, and $\bar{u}$ and $\bar{v}$ are their mean values. Figure 5-2(a) depicts the correlation matrix, which measures the linear dependence of pairs of variables. It can be seen that no single variable is a sufficiently good predictor of the target, demonstrating that more complex modeling is necessary to capture

their underlying relationships. Features are not linearly dependent, although high correlations are found for a few compositional elements such as V, N, and P, which implies their relative concentrations are fairly stable across the dataset. In Figure 5-2(b), the dataset is categorized by irradiation type, which can induce physically different radiation damage processes and microstructure evolution due to differing damage efficiencies [1]. To balance the relatively small dataset as well as capture the main distinctions among various types of radiation (neutrons, ions, and electrons), ion species such as "Fe^{++}", "Ni^{++}", and "C^{++}" are combined into a new category called "Ion." Therefore, the three types of radiation, i.e. "Neutron," "Electron," and "Ion" tag the data points. Figure 5-2(c) shows the distribution of the target variable in the dataset. It can be seen that the many fewer points exist for high incubation doses (> 200 dpa), which can deteriorate model prediction capability due to the scarcity of data points residing in the dimension space.
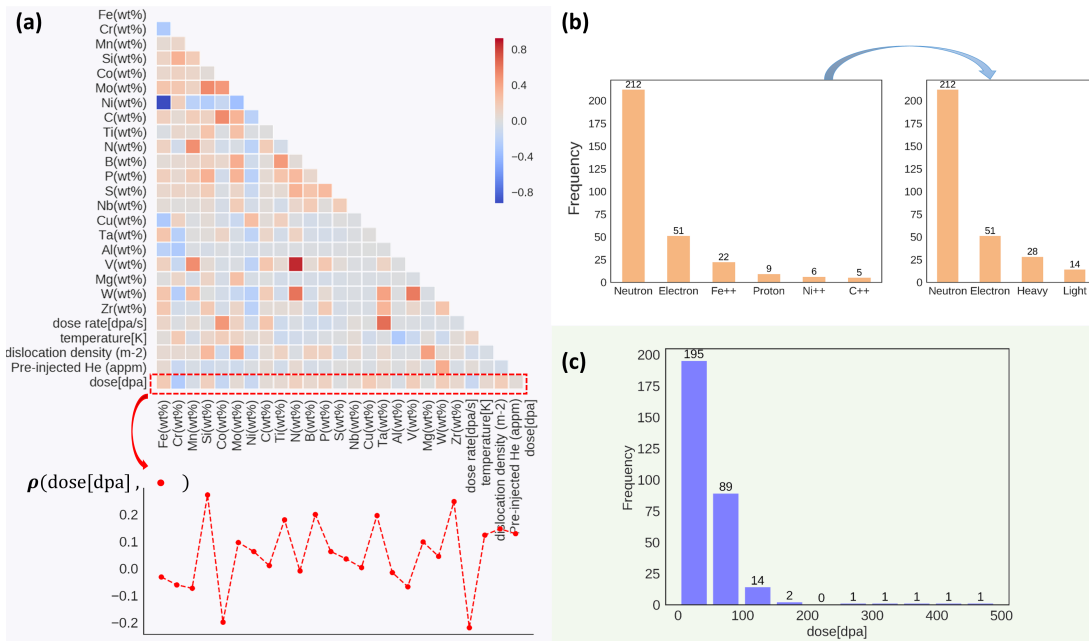
Figure 5-2: (a) Plot of correlation matrix $\rho(\cdot, \cdot)$ for each pair of variables denoted in the figure. Note that no significant linear dependence exists between variables, especially between the target variable (incubation dose) and all features. (b) Categorization of data by irradiation type: combining the original ion species "Fe^{++}" and "Ni^{++}" into "Heavy", and "C^{++}" and "Proton" into "Light" ion irradiation to make the dataset more balanced. (c) Distribution of the target variable (void swelling incubation dose) in the dataset.

5.1.3.2 Performance comparison

The predictive capability can now be compared across all applied regression models. Figure 5-3 demonstrates the results for the test data in a single training-test dataset split. Ideally, the prediction and real test values would align diagonally with high correlation. The LR performs poorly for both low and high incubation doses, meaning that a linear combination of the given features cannot characterize their association. By contrast, NN and the three ensemble methods give reasonably accurate predictions even of high quantities ($\gtrsim$ 100 dpa), despite their relative scarcity in the dataset. Among these well-performing models, the GB method appears most promising with a prediction slope close to unity and the highest correlation.
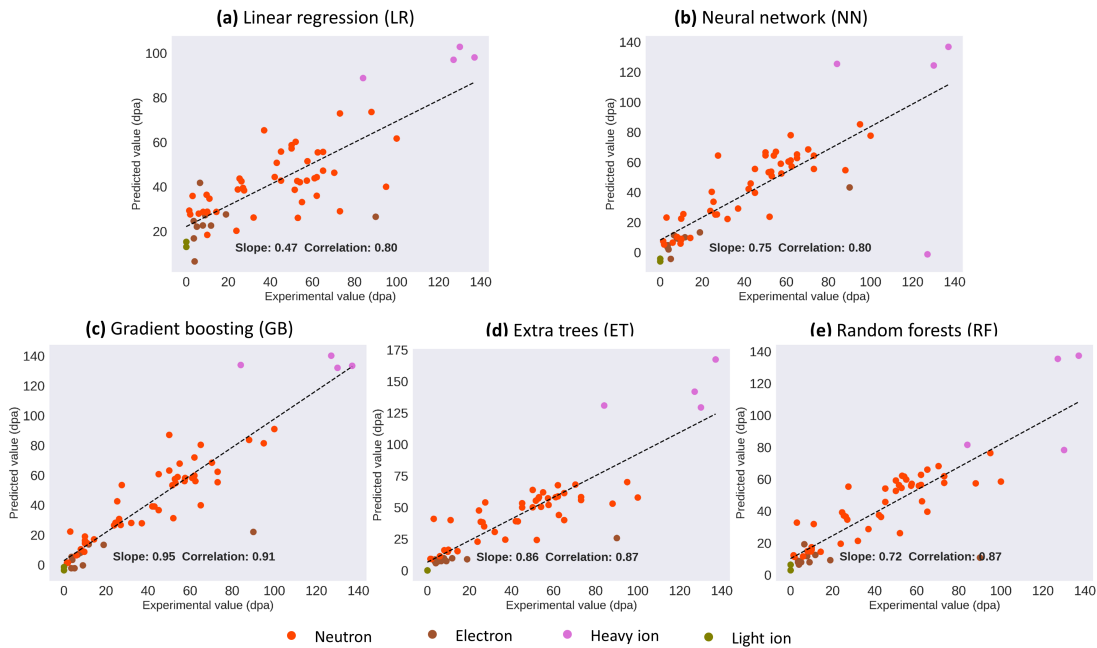
Figure 5-3: (a)-(e) Predicted versus experimental values of incubation dose using different machine learning models. The points are colored by the irradiation type. The GB method performed the best, with good predictions and high correlation.

The combination of a small dataset and the overfitting problem in ML methods can undermine its effectiveness in handling new data. To resolve such concerns due to how the dataset is split, the entire dataset is split into training and test set in different ways, leading to a distribution of predictive performance to demonstrate the robustness of these methods. Figure 5-4 shows box-plots of the mean squared error for

both training (a) and test sets (b). In the training stage, all methods except LR have very small errors and narrow distributions, indicating relative uniformity of training performance. The inset depicts a histogram of the error for GB method, whose small value indicates that the model fits the data very well. The error becomes much larger on the test set, which is evidence of overfitting. Among these methods, GB, RF, ET, and NN tend to predict the incubation dose very well, while the NN contains a few rather large outliers, indicating sensitivity to dataset split. In spite of overfitting, the GB method exhibits good performance with the majority of errors clustered around small values regardless of how the dataset is split, as confirmed by the distribution in the inset.
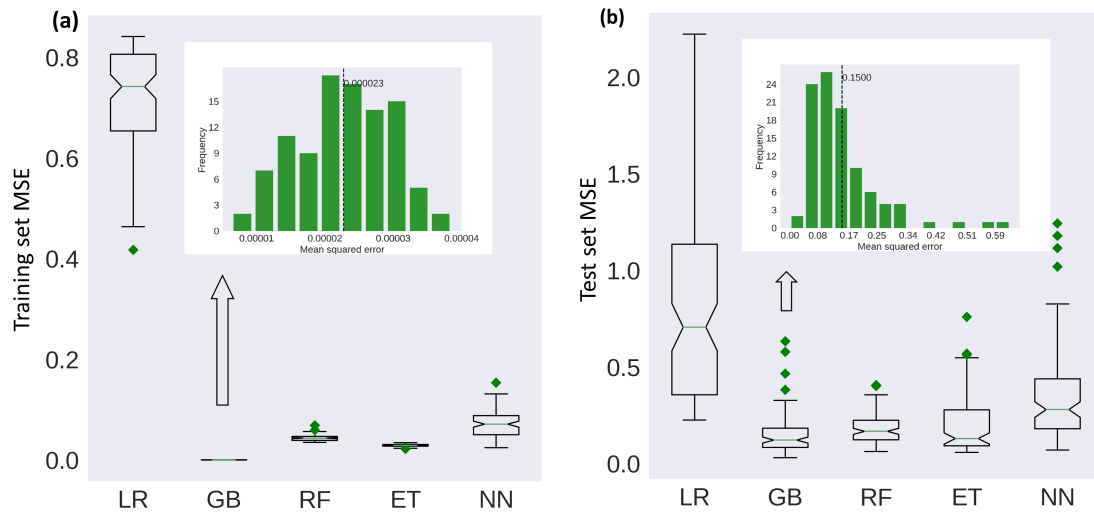
Figure 5-4: Box-plots of the MSE for training (a) and test (b) sets using different machine learning models. Insets plot the error distribution from the GB method. The difference in vertical scale between training (a) and testing stages (b) indicates overfitting. Note that the error is calculated with the normalized dataset.

5.1.3.3   Model interpretation

Fitting of these models can shed light on the controlling factors in predicting incubation dose. LR was excluded due to its poor performance, while NN was excluded due to a lack of interpretability resulting from the interaction of neurons and the activation function. Decision-tree based ensemble methods, on the other hand, can provide intuitive insights toward the problem via feature importance, which is ranked

with respect to the predictability of the target variable. Features which tend to be at the top of the trees impart greater weights in prediction, hence more important. Figure 5-5(a) compares the relative importance of the features as ranked by the GB method, with the top ten shown corresponding to the dataset split used in Figure 5-3. Features such as temperature, Cr, Fe, dose rate, Ni, C, pre-injected He, and dislocation density turn out to be significant in prediction. This finding is consistent with some established understanding in the void swelling behavior of alloys. Meanwhile, this relative ranking provides a quantitative estimate of which parameters are more dominant.

To check the sensitivity of the feature ranking to dataset split, 50 different split schemes are used to check the top ranked features in Figure 5-5(a) and the results are shown in (b)-(i). Despite slight variations in the ranking for these features, they remain fairly stable. Temperature maintains its highest priority; dose rate, Fe, and Cr appear the second tier; dislocation density, C, Ni, and N reside in the third tier. Such stability in ranking provides important information in understanding and predicting incubation dose under different conditions.
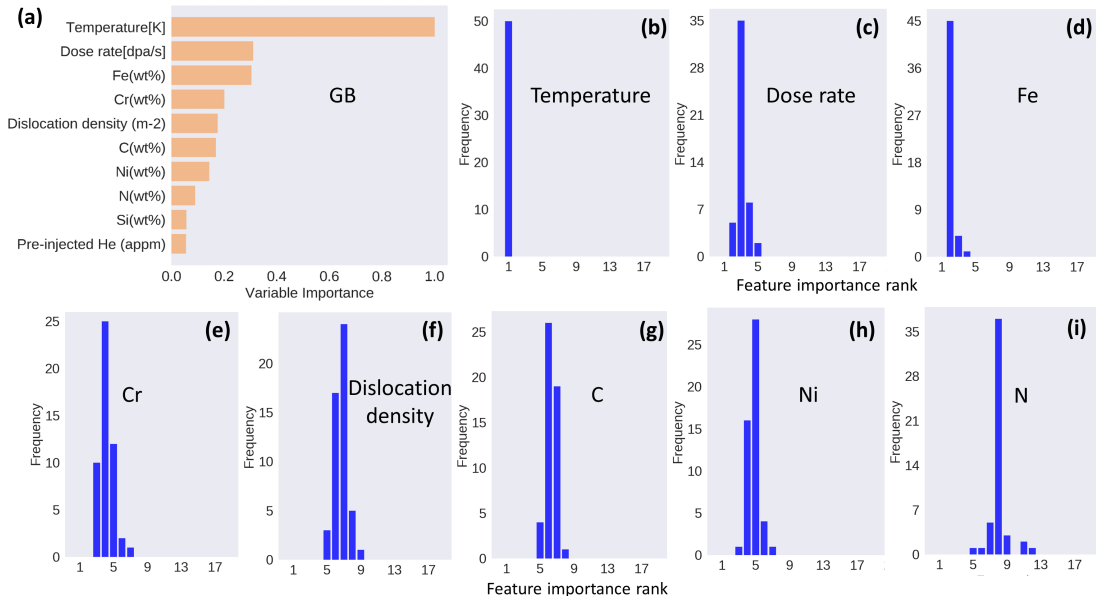
Figure 5-5: (a) Top ten important features in predicting void swelling using the GB method on a single dataset split; (b)-(i) Distribution of rank for the top ranked features from (a) using 50 different dataset splits.

5.1.4 Discussion

A sufficient volume of high quality data is the basis for ML. Based on the definition of incubation dose and potentially influential features, more than three hundred data points are collected by mining published literature. However, more data are expected to exist in technical reports and proprietary documents, often unindexed sources of data, although many earlier experiments may be unusable due to seriously incomplete information. This work as a proof-of-concept is meant to demonstrate the capability of ML to solve a complex nuclear materials problem with a limited amount of data typical in our field of study. The availability of additional data in the future will undoubtedly help to improve the models. An imminent plan is to construct an open-source data repository on void swelling for precisely this purpose, where users can download an existing data resource, upload a figure or study, register its source to exclude duplicates, and enter values or descriptions for available parameters. This will hopefully become a growing effort to accumulate more relevant data into a robust and predictive online ML tool to predict the incubation dose of a new material, in new conditions.

The simplest attempt with penalized linear regression showed that no single feature is a satisfying predictor based on correlation analysis, and that the data can not be well-described by a simple linear combination of features. It implies that non-linearity should be incorporated to perform robust predictions. One can solve this using at least two approaches, switching to other methods to consider non-linearity, or augmenting the linear model with non-linear transformation of its features. The latter method may render the model non-interpretable due to the versatility of potential transformation functions, thus the first proposal is admitted. Ensemble methods and neural networks are shown to provide excellent predictive capabilities despite overfitting. One of the ensemble methods, gradient boosting, appears stable regardless of dataset split. Its high fidelity enables us to use the model with confidence to identify the most contributing factors in predicting the onset of void swelling. The quantitative description of the relative importance of material and environmen-

tal parameters effectively capture the conventional understanding of factors affecting incubation dose. It has been well established that radiation-induced void formation strongly depends on alloy composition. The compositional sensitivity of steels can be ascribed to two categories, base or major solute atoms (Fe, Ni, Cr) and minor alloying elements (Si, C, Ti, P, Mo, etc.) [262]. Fundamentally, the incubation stage is closely related with the defect dynamics under the influence of biased defect sinks such as dislocations and grain boundaries. It can be also significantly modified by temperature, which effectively modifies the dominant defect reaction regimes responsible for the nucleation and growth of stable voids under irradiation [1]. Meanwhile, defect trapping by some elements such as Cr, V, Ni, and C, and precipitates can promote defect recombination and strongly influence the swelling behavior [248].

Since the subjective bias in model selection is alleviated by comparing different types of models with parameter optimization, the remaining error in the prediction of void swelling incubation dose can be mostly attributed to two reasons. Firstly, the dataset is limited in descriptive features such as He/dpa ratio, precipitates, ion injection, stress state, and grain size; and a lack of critical features that contribute to incubation dose can skew the prediction. For example, injected-interstitials in ion irradiation can suppress local swelling behavior [248]; and fine grains can delay swelling by providing large areas of defect sinks in the form of grain boundaries [249]. Secondly, the dataset is limited in size, a common issue in experimental studies. The trained models tend to overfit the training data, and generalization to test data produces much larger error even with controls on overfitting. On one hand, the dataset can be complemented by more active efforts in mining existing studies. On the other hand, as microstructures of candidate materials for advanced nuclear energy systems become increasingly complex, addition of more data on new high-performance material designs such as oxide-dispersion strengthened alloys [131], high entropy alloys [263], and nanostructured alloys [264] will become appropriate after incorporating additional features on proper representation of microstructural characteristics.

In summary, this study serves as a proof-of-concept that parameters including chemical composition, thermo-mechanical treatment, and experimental conditions

can provide a reasonable prediction of void swelling incubation dose, even though the dataset size is limited due to the inherent difficulties in conducting experiments. The identification of controlling factors in the learned model (GB) not only generates results consistent with the established understanding of key parameters, but also provides additional, meaningful insights into radiation-resistant material design.

5.2 Summary

Machine learning provides a viable avenue to extracting insights from data. The study introduced here serves as a proof-of-concept that this technique can prove useful for nuclear materials research. Although this application does not probe into the physical processes of radiation damage, it demonstrates high potential in predicting incubation dose based on previous and ongoing research efforts. From an engineering perspective, it is promising to extend this methodology to the prediction of other radiation effects, such as the ductile-brittle transition temperature (DBTT) [218] and phase stability.

It is worth mentioning that depending on the specifics of problem, physics can be appropriately incorporated. It can be in the form of presumably influential features, or aggregated feature based on other variables, or part of a physics-based framework which efficiency fulfills information query to accelerate computation, or controlling terms for learning the equation underlying the dataset. The realization is very much problem specific, and given the availability of data, the integration of ML and nuclear materials can be extremely rewarding.

Chapter 6

Summary

6.1   Thesis overview

Modeling and simulation is an integral part to the study of nuclear materials subject to harsh environments in both current and proposed future nuclear energy systems. Especially, radiation brings out a number of unique materials degradation modes such as void swelling and phase instability. This thesis work orients around the radiation damage in materials, and studies some specific problems from three perspectives: atomistic understanding of radiation resistance (Sections 3.1, 3.2, 3.3, and 3.4), multiscale description of microstructure evolution (Sections 4.1 and 4.2), and phenomenological prediction of radiation effects with machine learning (Section 5). Specifically, Sections 3.1 and 3.2 elaborates the radiation process and damage resistance mechanisms in single-phase concentrated solid solution alloys and nanocrystalline metals, where composition varying Ni-Fe alloys and Cu were used as the model materials, respectively. Following the issue of radiation-enhance grain growth of nanocrystalline material, Section 3.3 focus on resolving the grain boundary migration and grain growth behavior. To mitigate the issue of grain growth which effectively degrades the mechanical property, nanocrystalline metals can be manufactured with interface engineering, one of which is to recast the grain boundaries into amorphous intergranular film. Such design can not only significantly increase the ductility of nanocrystalline metals, but also pin down the interface migration. To assess its radiation performance,

topics including ion-mixing, defect property, and interface evolution are analyzed in Section 3.4. To break the limitation of atomistic simulations, multiscale framework is then built to study the long-therm radiation-induced defect evolution. Particularly, the meso-scale cluster dynamics model is implemented with a finite element solver to bridge the atomistic details to experimental observations using TEM (transmission electron microscopy). With this framework, Section 4.1 explains the deviation from pow law for the experimentally measured defect size distribution in self-ion irradiated tungsten. To resolve spatial dependent defect production as commonly seen in ion irradiation, Section 4.2 focuses on modeling the void swelling profile with respect to the self-ion irradiation range. These multiscale studies still consider very simply cases like pure metal, but in real applications, many more physical processes might need to be considered in order to describe experiments well, such as dislocation evolution, solute migration, and concurrent phase changes. Therefore, a potential shortcut may be taken via data-driven approach. Section 5, as proof-of-concept, demonstrates the feasibility of using machine learning to predict radiation effects, specifically, the onset of void swelling in irradiated metals. After manually collecting more than 300 data points, the models have delivered promising results. However, additional efforts are still necessary to collect more high quality data, and construction of public platform to crowdsource nuclear materials experimental studies will significantly contribute to the whole research domain.

The computational work can not only reveal the fundamental mechanisms in radiation-induced processes that are unaccessible in experimental measurement, but also be capable of predicting material behavior on the experimental scale. These initial work builds the foundation of ultimate plan to coordinate atomistic, multiscale and data-driven approaches, and complement with targeted experimental testing to reach a synergy between modeling and experimentation in tackling the challenge of accelerating the development and qualification of advanced materials.

6.2 Thesis contributions

Orienting radiation damage in materials, this thesis work has the following main contributions:

- Radiation process in Ni_xFe_{1-x} ($x \in [0, 90\%]$) is elaborated atomistically with increasing dose up to dpa level; the radiation resistance can well be explained by the heterogeneous diffusion of point defects inferred from the distributions of defect migration barrier; thermodynamic mixing energy strongly correlates with the radiation performance of the alloys with different compositions, which can potentially serve as a design guidance to optimize this type of alloys.

- Radiation process in nanocrystalline Cu is examined atomistically using a bi-crystal model with dose up to dpa level; the main mechanism responsible for the high radiation resistance provided by grain boundaries (GB) is found to be GB-biased SFT migration and absorption; GBs are observed to be very resilient and can self-heal after distortion induced by interaction with SFTs; decreasing the grain size to small values ($\lesssim 10$ nm) can significantly decrease the saturated defect density in the bulk.

- The atomistic process of radiation-enhanced grain growth in nanocrytalline Cu using a bi-crystal model is followed with increasing dose; a 3-stage mechanism is proposed to describe the grain growth behavior including: random work migration of GBs due to disturbance of damage cascades when two GBs are farther apart; biased and approaching migration of GBs due to SFTs simultaneous attraction as distance between GBs shrinks; curvature-driven fast boundary migration as GBs adjoin.

- Interface engineered nanocrystalline Cu by doping Zr atoms, which transform GBs into amorphous intergranular films, is assessed under irradiation using atomistic simulations; the ion-mixing can be well-characterized by superposition of solution to diffusion equation; the defect clusters remain small due to reduced clustering and solute-mediated defect annihilation; the interfaces are effectively anchored by the Zr atoms.

- A multiscale framework containing binary collision approximation, molecular dynamics simulation of damage cascades and cluster dynamics of long term evolution is built to break the scale limit of atomistic simulations; its application to self-irradiation tungsten at 30 K successfully explain the deviation from power law distribution of the measured defect size distribution, by considering the long-time evolution induced by the mobile interstitial and interstitial clusters, which is well beyond the scale of damage cascades over picoseconds; the framework has also been demonstrated to describe spatial dependent microstructure evolution in ion irradiated pure iron.

- Data-driven approach using machine learning has been explored in the context of nuclear materials; a specific application in applying different ML models to predict the onset of void swelling has generated promising results for predicting the out-of-sample data points; this work demonstrates the feasibility of ML in radiation effect prediction based on macro quantities such as chemical compositions and environmental parameters; this work marks the initiation of future plan in kickstarting nuclear materials genome project to reuse the existent experimental data and guide more informative material optimization for nuclear applications.

6.3   Outlook

Although computational and theoretical understanding have received great success in nuclear materials study, especially the various computation techniques specializing over different range of time and length scales, there are still some key problems that need to be reconciled including computation acceleration, uncertainty propagation, fundamental understanding, and material optimization.

- Computation acceleration
  The computational cost becomes the bottleneck in describing some important processes expected during radiation damage study. For example, MD is commonly used to characterize the primary damage stage of cascading process. The

length and time scale is mostly caped at nano to micro scale due to computation constraint. Since MD admits the least assumptions towards defect interactions given a high-quality empirical inter-atomic potential, the extension of longer scale is very much valued. In fact, a number of efforts have been paid on this aspect to break the timescale limit, such as temperature accelerated dynamics [163], parallel replica dynamics [164], and hyperdynamics [165]. However, radiation-enhanced microstructure evolution indispensably require the description on experimental measurement scale (micron to millimeter). The notion of multiscale modeling is thus pursued to resolve this conundrum, but such scheme is still exposed to inefficiency issue. For example, KMC is frequently utilized to explicitly describe defect reactions and deal with the spatial correlation of defects. Nevertheless, the system can become computation prohibitive with increasing pool of events to sample from and small barrier operations which prevent efficient advancement of simulation time. Better representation of the problem [265] is promising to improve the KMC models. Meanwhile, modern data-driven approach using machine learning could potential become useful in accelerating these methods by querying local structure information [266]. Finally, the practice of coupling multiple/multiscale simulation techniques to characterize the complex physical process may open door to the construction of simpler models, e.g. reduced order model to effectively lower the complexity of conventional physics-based simulations [267] and enable efficient exploration of parameter space for material optimization.

- Uncertainty propagation
A critical question in linking multiscale techniques lies in the propagation of uncertainty. It should be realized that in either the atomistic simulations of damage cascades or the calculation of defect diffusion properties, there is always uncertainty attached. One should be cautious about the modeling procedure; although the simulations may build on top of deterministic description as seen in the chemical reaction kinetics, the parameters bearing uncertainty could in-

troduce significant deviation in the long run. For example, MD simulations can give a distribution of defect migration energy depending on the local environment [4], hence a single value to generalize the energy barrier may be crude. Figure 6-1 also demonstrates the idea by calculating the formation and migration energies of vacancy in $Fe_{10}Ni_{72}Cr_{18}$ (simplified model for Alloy 600, which is a solid solution strengthened alloy used for applications that require corrosion and high temperature resistance). A proper sensitivity and uncertainty analysis is important but commonly neglected in the material simulations.

(a)   (b)
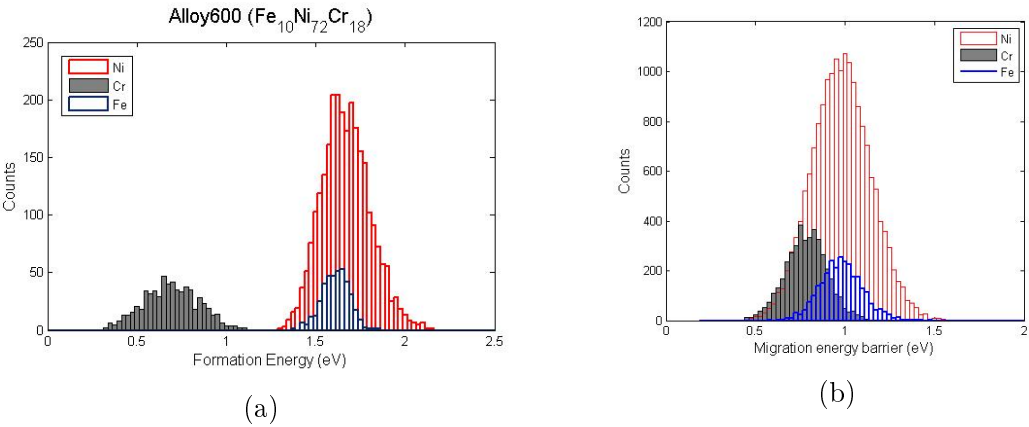
Figure 6-1: Distribution of vacancy formation energy (a) and migration energy (b) in Alloy 600 ($Fe_{10}Ni_{72}Cr_{18}$). Courtesy of Dr. P.H. Cao from MIT.

- Fundamental understanding

  Theoretical framework is closely attached to the fundamental understanding of the mechanisms, such as the formalism of dislocation sink strength, precipitates effect, and solute dragging. With the prosperity of new material designs such as high entropy alloys and nanoengineered metals, which are potential candidates for future nuclear energy system, the mechanisms that dictate microstructure evolution are of utmost importance to evaluate material performance under extreme environments. For instance, oxide-dispersion-strengthened (ODS) alloys with nano-cluters embedded in the steel matrix have received much attention in recent years due to its exceptional radiation-resistant and high temperature mechanical properties. However, a comprehensive examination regarding these

nanoclusters such as number density, coherency, stability, and evolution is still badly needed. Many of the fundamental issues can resort to atomistic simulations. However, it should be noted that although atomistic simulations can reveal some fundamental processes of defect migration and interactions, efforts are still in demand to incorporate them into the theoretical description. For example, the interstitial-loaded grain boundaries are found to emit interstitials to annihilate nearby vacancies [21]; the loss of inclusion coherency due to dislocation loop punching [268]; defective SFTs in Cu are much more mobile than standard ones [162].

- Material optimization

  One ultimate goal of computational materials study is to predict material behavior, optimize existing materials, and discover new materials. Recent years, experimental studies generate many fascinating results with superior properties by tweaking the composition and microstructure to the nanometer scale, such as high entropy alloys, interface engineering and nanostructures. These designs have delivered exceptional properties from the reported experimental results, based on some general principle. For example, nanostructured materials have good mechanical strength based on the Hall-Patch equation, and also admit high radiation resistance due to abundant defect sinks. However, to unlock the full potential of these designs, computational studies can not only help understand the underlying the mechanisms, but also serve to complement the limited number of experiments by exploring the parameter space beyond the testings. Making use of the predictability of computational models, candidate samples can then manufactured for the targeted experiments, hence enable a far more efficient process of super material discovery. For example, in the ODS alloys, evaluation of many parameters are in imminent need to be assessed to achieve even better performance, such as the nanooxide density, size, and coherency with matrix. In the case of high entropy alloys, high dimension optimization on the composition can efficiently help identify potential optima than traditional

trial and error.

- Data reuse

  Materials testing for nuclear applications often subjects to high inefficiency and cost due to the demanding experimental conditions. However, experiments are the prerequisite of industrial applications. The accumulated results over the years of nuclear materials study can be rejuvenated upon the advancement of artificial intelligence. The synergy among all relevant data may reveal the embedded relations among involved variables in the connecting material properties with responses like radiation effects. Machine learning has achieved great success in materials design as introduced in Section 5, therefore, the innovative integration of ML and nuclear materials can kickstart more active research in such inter-disciplinary domain. To facilitate further development, a nuclear materials genome project consisting of databases on experimental studies and high-fidelity calculations, and ML models exploring the embedded pattern can be extremely valuable to whole research domain. Meanwhile, collaborative efforts can significantly contribute to the construction of platform to enable public access to retrieve and contribute data resources. Additionally, more effective data collection may be pursued via natural language processing to automate literature scrapping.

These imminent problems motivates the future research plan to coordinate atomistic, multiscale and data-driven techniques. This thesis work builds the foundation of more extensive and in-depth study on relevant problems. For example, the study of Ni_xFe_{1-x} as presented in Section 3.1 suggests that the thermodynamic mixing energy correlate very well with radiation resistance which can potential guide the alloy optimization. To validate this claim, more elemental cases are required to be examined. As another example in the multiscale framework, the spatial dependent microstructure evolution needs to considered for realistic description of experiments such as the migration of constitute alloying elements and phase transformation. A last example is to describe the dynamic evolution process using machine learning

174

informed prediction, which can largely reduce the computation cost. Tackling these problems extended from this thesis research is aimed to broaden the understanding of materials behavior and accelerate the qualification of advanced materials for nuclear applications.

Bibliography

[1] G. S. Was, *Fundamentals of radiation materials science: metals and alloys.* Springer, 2016.

[2] Wikipedia contributors, "Generation IV reactor — Wikipedia, the free encyclopedia," 2018. [Online; `https://en.wikipedia.org/w/index.php?title=Generation_IV_reactor&oldid=844037826`].

[3] G. Odette, M. Alinger, and B. Wirth, "Recent developments in irradiation-resistant steels," *Annual Review Materials Research*, vol. 38, pp. 471–503, 2008.

[4] M. Jin, P. Cao, and M. P. Short, "Thermodynamic mixing energy and heterogeneous diffusion uncover the mechanisms of radiation damage reduction in single-phase ni-fe alloys," *Acta Materialia*, vol. 147, pp. 16–23, 2018.

[5] A. Misra, M. Demkowicz, X. Zhang, and R. Hoagland, "The radiation damage tolerance of ultra-high strength nanolayered composites," *Jom*, vol. 59, no. 9, pp. 62–65, 2007.

[6] J. E. Ludy and T. J. Rupert, "Amorphous intergranular films act as ultra-efficient point defect sinks during collision cascades," *Scripta Materialia*, vol. 110, pp. 37–40, 2016.

[7] M. P. Short and S. Yip, "Materials aging at the mesoscale: Kinetics of thermal, stress, radiation activations," *Current Opinion in Solid State and Materials Science*, vol. 19, no. 4, pp. 245–252, 2015.

[8] M. Short, D. Gaston, C. Stanek, and S. Yip, "A perspective on coupled multiscale simulation and validation in nuclear materials," *MRS Bulletin*, vol. 39, no. 1, pp. 71–77, 2014.

[9] S. Zinkle and G. Was, "Materials challenges in nuclear energy," *Acta Materialia*, vol. 61, no. 3, pp. 735 – 758, 2013.

[10] H. Heinisch, M. Hamilton, W. Sommer, and P. Ferguson, "Tensile property changes of metals irradiated to low doses with fission, fusion and spallation neutrons," *Journal of Nuclear Materials*, vol. 191-194, Part B, pp. 1177–1182, Sept. 1992.

[11] M. Norgett, M. Robinson, and I. Torrens, "A proposed method of calculating displacement dose rates," *Nuclear Engineering and Design*, vol. 33, no. 1, pp. 50–54, 1975.

[12] C. Woo and B. Singh, "Production bias due to clustering of point defects in irradiation-induced cascades," *Philosophical Magazine A*, vol. 65, no. 4, pp. 889–912, 1992.

[13] G. Was and T. Allen, "Radiation-induced segregation in multicomponent alloys: Effect of particle type," *Materials Characterization*, vol. 32, no. 4, pp. 239 – 255, 1994.

[14] G. Gupta, Z. Jiao, A. Ham, J. Busby, and G. Was, "Microstructural evolution of proton irradiated T91," *Journal of Nuclear Materials*, vol. 351, no. 1–3, pp. 162–173, 2006.

[15] G. Was and T. Allen, "Intercomparison of microchemical evolution under various types of particle irradiation," *Journal of Nuclear Materials*, vol. 205, pp. 332 – 338, 1993.

[16] E. Getto, K. Sun, A. Monterrosa, Z. Jiao, M. Hackett, and G. Was, "Void swelling and microstructure evolution at very high damage level in self-ion irradiated ferritic-martensitic steels," *Journal of Nuclear Materials*, vol. 480, pp. 159–176, 2016.

[17] A. Kozlov, V. Panchenko, K. Kozlov, I. Russkikh, and A. V. Kozlov, "Evolution of radiation defects in nickel under low-temperature neutron irradiation," *The Physics of Metals and Metallography*, vol. 115, no. 1, pp. 39–45, 2014.

[18] J. F. Ziegler, M. D. Ziegler, and J. P. Biersack, "SRIM–the stopping and range of ions in matter (2010)," *Nuclear Instruments and Methods in Physics Research Section B: Beam Interactions with Materials and Atoms*, vol. 268, no. 11-12, pp. 1818–1823, 2010.

[19] R. E. Stoller, M. B. Toloczko, G. S. Was, A. G. Certain, S. Dwaraknath, and F. A. Garner, "On the use of srim for computing radiation damage exposure," *Nuclear instruments and methods in physics research section B: beam interactions with materials and atoms*, vol. 310, pp. 75–80, 2013.

[20] W. Setyawan, G. Nandipati, K. J. Roche, H. L. Heinisch, B. D. Wirth, and R. J. Kurtz, "Displacement cascades and defects annealing in tungsten, part i: Defect database from molecular dynamics simulations," *Journal of Nuclear Materials*, vol. 462, pp. 329–337, 2015.

[21] X.-M. Bai, A. F. Voter, R. G. Hoagland, M. Nastasi, and B. P. Uberuaga, "Efficient annealing of radiation damage near grain boundaries via interstitial emission," *Science*, vol. 327, no. 5973, pp. 1631–1634, 2010.

[22] C. S. Becquart, C. Domain, U. Sarkar, A. Debacker, and M. Hou, "Microstructural evolution of irradiated tungsten: Ab initio parameterisation of an okmc model," *Journal of Nuclear Materials*, vol. 403, no. 1, pp. 75–88, 2010.

[23] G. Nandipati, W. Setyawan, H. L. Heinisch, K. J. Roche, R. J. Kurtz, and B. D. Wirth, "Displacement cascades and defect annealing in tungsten, part ii: Object kinetic monte carlo simulation of tungsten cascade aging," *Journal of Nuclear Materials*, vol. 462, pp. 338–344, 2015.

[24] G. Nandipati, W. Setyawan, H. L. Heinisch, K. J. Roche, R. J. Kurtz, and B. D. Wirth, "Displacement cascades and defect annealing in tungsten, part iii: The sensitivity of cascade annealing in tungsten to the values of kinetic parameters," *Journal of Nuclear Materials*, vol. 462, pp. 345–353, 2015.

[25] C.-C. Fu, J. D. Torre, F. Willaime, J.-L. Bocquet, and A. Barbu, "Multiscale modelling of defect kinetics in irradiated iron," *Nature Materials*, vol. 4, pp. 68–74, Jan. 2005.

[26] R. Grima, "An effective rate equation approach to reaction kinetics in small volumes: Theory and application to biochemical reactions in nonequilibrium steady-state conditions," *The Journal of Chemical Physics*, vol. 133, no. 3, p. 07B604, 2010.

[27] J. Marian and V. V. Bulatov, "Stochastic cluster dynamics method for simulations of multispecies irradiation damage accumulation," *Journal of Nuclear Materials*, vol. 415, no. 1, pp. 84 – 95, 2011.

[28] F. Christien and A. Barbu, "Cluster dynamics modelling of irradiation growth of zirconium single crystals," *Journal of Nuclear Materials*, vol. 393, no. 1, pp. 153 – 161, 2009.

[29] R. Stoller, S. Golubov, C. Domain, and C. Becquart, "Mean field rate theory and object kinetic monte carlo: A comparison of kinetic models," *Journal of Nuclear Materials*, vol. 382, no. 2–3, pp. 77–90, 2008.

[30] T. Jourdan, G. Bencteux, and G. Adjanor, "Efficient simulation of kinetics of radiation induced defects: A cluster dynamics approach," *Journal of Nuclear Materials*, vol. 444, no. 1, pp. 298–313, 2014.

[31] D. Xu, B. D. Wirth, M. Li, and M. A. Kirk, "Combining in situ transmission electron microscopy irradiation experiments with cluster dynamics modeling to study nanoscale defect agglomeration in structural metals," *Acta Materialia*, vol. 60, no. 10, pp. 4286–4302, 2012.

[32] E. Meslin, A. Barbu, L. Boulanger, B. Radiguet, P. Pareige, K. Arakawa, and C. Fu, "Cluster-dynamics modelling of defects in α-iron under cascade damage conditions," *Journal of Nuclear Materials*, vol. 382, no. 2-3, pp. 190–196, 2008.

[33] E. Lee and L. Mansur, "A mechanism of swelling suppression in phosphorous-modified fe-ni-cr alloys," *Journal of Nuclear Materials*, vol. 141, pp. 695–702, 1986.

[34] E. Little, "Development of radiation resistant materials for advanced nuclear power plant," *Materials science and technology*, vol. 22, no. 5, pp. 491–518, 2006.

[35] S. Ukai, M. Harada, H. Okada, M. Inoue, S. Nomura, S. Shikakura, K. Asabe, T. Nishida, and M. Fujiwara, "Alloying design of oxide dispersion strengthened ferritic steel for long life fbrs core materials," *Journal of Nuclear Materials*, vol. 204, pp. 65–73, 1993.

[36] R. Klueh, P. Maziasz, I. Kim, L. Heatherly, D. Hoelzer, N. Hashimoto, E. Kenik, and K. Miyahara, "Tensile and creep properties of an oxide dispersion-strengthened ferritic steel," *Journal of Nuclear Materials*, vol. 307, pp. 773–777, 2002.

[37] T. R. Allen, J. Gan, J. I. Cole, M. K. Miller, J. T. Busby, S. Shutthanandan, and S. Thevuthasan, "Radiation response of a 9 chromium oxide dispersion strengthened steel to heavy ion irradiation," *Journal of Nuclear Materials*, vol. 375, no. 1, pp. 26–37, 2008.

[38] S. Ukai and M. Fujiwara, "Perspective of ods alloys application in nuclear environments," *Journal of Nuclear Materials*, vol. 307, pp. 749–757, 2002.

[39] A. Hirata, T. Fujita, Y. Wen, J. Schneibel, C. T. Liu, and M. Chen, "Atomic structure of nanoclusters in oxide-dispersion-strengthened steels," *Nature Materials*, vol. 10, no. 12, p. 922, 2011.

[40] X. Zhang, K. Hattar, Y. Chen, L. Shao, J. Li, C. Sun, K. Yu, N. Li, M. L. Taheri, H. Wang, *et al.*, "Radiation damage in nanostructured materials," *Progress in Materials Science*, 2018.

[41] C. Sun, D. Bufford, Y. Chen, M. Kirk, Y. Wang, M. Li, H. Wang, S. Maloy, and X. Zhang, "In situ study of defect migration kinetics in nanoporous ag with enhanced radiation tolerance," *Scientific Reports*, vol. 4, p. 3737, 2014.

[42] Y. Zhang, K. Jin, H. Xue, C. Lu, R. J. Olsen, L. K. Beland, M. W. Ullah, S. Zhao, H. Bei, D. S. Aidhy, and et al., "Influence of chemical disorder on energy dissipation and defect evolution in advanced alloys," *Journal of Materials Research*, vol. 31, no. 16, pp. 2363–2375, 2016.

[43] M. W. Ullah, H. Xue, G. Velisa, K. Jin, H. Bei, W. J. Weber, and Y. Zhang, "Effects of chemical alternation on damage accumulation in concentrated solid-solution alloys," *Sci. Rep.*, vol. 7, 2017.

[44] F. Granberg, K. Nordlund, M. W. Ullah, K. Jin, C. Lu, H. Bei, L. Wang, F. Djurabekova, W. Weber, and Y. Zhang, "Mechanism of radiation damage reduction in equiatomic multicomponent single phase alloys," *Physical Review Letters*, vol. 116, no. 13, p. 135504, 2016.

[45] M. W. Ullah, D. S. Aidhy, Y. Zhang, and W. J. Weber, "Damage accumulation in ion-irradiated Ni-based concentrated solid-solution alloys," *Acta Materialia*, vol. 109, pp. 17–22, 2016.

[46] C. Lu, L. Niu, N. Chen, K. Jin, T. Yang, P. Xiu, Y. Zhang, F. Gao, H. Bei, S. Shi, *et al.*, "Enhancing radiation tolerance by controlling defect mobility and migration pathways in multicomponent single-phase alloys," *Nature Communication*, vol. 7, p. 13564, 2016.

[47] J. Brodrick, D. Hepburn, and G. Ackland, "Mechanism for radiation damage resistance in yttrium oxide dispersion strengthened steels," *Journal of Nuclear Materials*, vol. 445, no. 1, pp. 291 – 297, 2014.

[48] C. Sun, S. Zheng, C. C. Wei, Y. Wu, L. Shao, Y. Yang, K. T. Hartwig, S. A. Maloy, S. J. Zinkle, T. R. Allen, H. Wang, and X. Zhang, "Superior radiation-resistant nanoengineered austenitic 304L stainless steel for applications in extreme radiation environments," *Scientific Report*, vol. 5, p. 7801, 2015.

[49] I. Beyerlein, A. Caro, M. Demkowicz, N. Mara, A. Misra, and B. Uberuaga, "Radiation damage tolerant nanomaterials," *Materials today*, vol. 16, no. 11, pp. 443–449, 2013.

[50] B. Cantor, I. Chang, P. Knight, and A. Vincent, "Microstructural development in equiatomic multicomponent alloys," *Materials Science and Engineering: A*, vol. 375, pp. 213 – 218, 2004.

[51] Y. Zhang, T. T. Zuo, Z. Tang, M. C. Gao, K. A. Dahmen, P. K. Liaw, and Z. P. Lu, "Microstructures and properties of high-entropy alloys," *Progress in Materials Science*, vol. 61, pp. 1 – 93, 2014.

[52] J.-W. Yeh, S.-K. Chen, S.-J. Lin, J.-Y. Gan, T.-S. Chin, T.-T. Shun, C.-H. Tsau, and S.-Y. Chang, "Nanostructured high-entropy alloys with multiple principal elements: Novel alloy design concepts and outcomes," *Advanced Engineering Materials*, vol. 6, no. 5, pp. 299–303, 2004.

[53] G. Salishchev, M. Tikhonovsky, D. Shaysultanov, N. Stepanov, A. Kuznetsov, I. Kolodiy, A. Tortika, and O. Senkov, "Effect of Mn and V on structure and mechanical properties of high-entropy alloys based on CoCrFeNi system," *Journal of Alloys and Compounds*, vol. 591, pp. 11 – 21, 2014.

[54] H. Zhang, Y. He, and Y. Pan, "Enhanced hardness and fracture toughness of the laser-solidified $FeCoNiCrCuTiMoAlSiB_{0.5}$ high-entropy alloy by martensite strengthening," *Scripta Materialia*, vol. 69, no. 4, pp. 342 – 345, 2013.

[55] Y. Qiu, M. A. Gibson, H. L. Fraser, and N. Birbilis, "Corrosion characteristics of high entropy alloys," *Materals Science and Technology*, vol. 31, no. 10, pp. 1235–1243, 2015.

[56] L. Wang, S. Zinkle, R. Dodd, and G. Kulcinski, "Effects of preinjected helium in heavy-ion irradiated nickel and nickel-copper alloys," *Metal. Trans. A*, vol. 21, no. 7, pp. 1847–1851, 1990.

[57] Y. Zhang, G. M. Stocks, K. Jin, C. Lu, H. Bei, B. C. Sales, L. Wang, L. K. Béland, R. E. Stoller, G. D. Samolyuk, *et al.*, "Influence of chemical disorder on energy dissipation and defect evolution in concentrated solid solution alloys," *Nature Communication*, vol. 6, p. 8736, 2015.

[58] K. Jin, W. Guo, C. Lu, M. W. Ullah, Y. Zhang, W. J. Weber, L. Wang, J. D. Poplawsky, and H. Bei, "Effects of Fe concentration on the ion-irradiation induced defect evolution and hardening in Ni-Fe solid solution alloys," *Acta Materialia*, vol. 121, pp. 365–373, 2016.

[59] G. Henkelman, B. P. Uberuaga, and H. Jónsson, "A climbing image nudged elastic band method for finding saddle points and minimum energy paths," *Journal of Chemical Physics*, vol. 113, no. 22, pp. 9901–9904, 2000.

[60] G. Bonny, N. Castin, and D. Terentyev, "Interatomic potential for studying ageing under irradiation in stainless steels: the FeNiCr model alloy," *Modelling and Simulation in Materials Science and Engineering*, vol. 21, no. 8, p. 085004, 2013.

[61] G. Bonny, D. Terentyev, R. Pasianot, S. Poncé, and A. Bakaev, "Interatomic potential to study plasticity in stainless steels: the FeNiCr model alloy," *Modelling and Simulation in Materials Science and Engineering*, vol. 19, no. 8, p. 085008, 2011.

[62] G. Velişa, M. W. Ullah, H. Xue, K. Jin, M. L. Crespillo, H. Bei, W. J. Weber, and Y. Zhang, "Irradiation-induced damage evolution in concentrated Ni-based alloys," *Acta Materialia*, 2017.

[63] S. Rao, C. Varvenne, C. Woodward, T. Parthasarathy, D. Miracle, O. Senkov, and W. Curtin, "Atomistic simulations of dislocations in a model bcc multicomponent concentrated solid solution alloy," *Acta Materialia*, vol. 125, pp. 311–320, 2017.

[64] S. Zhao, G. M. Stocks, and Y. Zhang, "Defect energetics of concentrated solid-solution alloys from ab initio calculations: $Ni_{0.5}Co_{0.5}$, $Ni_{0.5}Fe_{0.5}$, $Ni_{0.8}Fe_{0.2}$ and $Ni_{0.8}Cr_{0.2}$," *Physical Chemistry Chemical Physics*, vol. 18, no. 34, pp. 24043–24056, 2016.

[65] J. Cowley, "An approximate theory of order in alloys," *Physics Review*, vol. 77, no. 5, p. 669, 1950.

[66] H. B. Lee, F. B. Prinz, and W. Cai, "Atomistic simulations of surface segregation of defects in solid oxide electrolytes," *Acta Materialia*, vol. 58, no. 6, pp. 2197–2206, 2010.

[67] B. Sadigh, P. Erhart, A. Stukowski, A. Caro, E. Martinez, and L. Zepeda-Ruiz, "Scalable parallel monte carlo algorithm for atomistic simulations of precipitation in alloys," *Physics Review B*, vol. 85, no. 18, p. 184203, 2012.

[68] S. Plimpton, P. Crozier, and A. Thompson, "Lammps-large-scale atomic/molecular massively parallel simulator," *Journal of Computational Physics*, vol. 18, 2007.

[69] J. F. Ziegler, J. P. Biersack, and U. Littmark, *The Stopping and Range of Ions in Solids*. Pergamon Press, 1985.

[70] K. Nordlund, M. Ghaly, R. Averback, M. Caturla, T. D. de La Rubia, and J. Tarus, "Defect production in collision cascades in elemental semiconductors and fcc metals," *Physics Review B*, vol. 57, no. 13, p. 7556, 1998.

[71] L. K. Béland, C. Lu, Y. N. Osetskiy, G. D. Samolyuk, A. Caro, L. Wang, and R. E. Stoller, "Features of primary damage by high energy displacement cascades in concentrated ni-based alloys," *Journal of Applied Physics*, vol. 119, no. 8, p. 085901, 2016.

[72] S. Nosé, "A molecular dynamics method for simulations in the canonical ensemble," *Molecular Physics*, vol. 52, no. 2, pp. 255–268, 1984.

[73] W. G. Hoover, "Canonical dynamics: Equilibrium phase-space distributions," *Physics Review A*, vol. 31, pp. 1695–1697, 1985.

[74] A. Stukowski, "Structure identification methods for atomistic simulations of crystalline materials," *Modelling and Simulation in Materials Science and Engineering*, vol. 20, no. 4, p. 045021, 2012.

[75] K. J. Laidler and M. C. King, "Development of transition-state theory," *Journal of Physical Chemistry*, vol. 87, no. 15, pp. 2657–2664, 1983.

[76] J. Greeley, I. E. L. Stephens, A. S. Bondarenko, T. P. Johansson, H. A. Hansen, T. F. Jaramillo, J. Rossmeisl, I. Chorkendorff, and J. K. Nørskov, "Alloys of platinum and early transition metals as oxygen reduction electrocatalysts," *Nature Chemistry*, vol. 1, pp. 552–556, 2009.

[77] U. G. Vej-Hansen, J. Rossmeisl, I. E. L. Stephens, and J. Schiotz, "Correlation between diffusion barriers and alloying energy in binary alloys," *Physical Chemistry Chemical Physics*, vol. 18, pp. 3302–3307, 2016.

[78] M. Mantina, Y. Wang, L. Chen, Z. Liu, and C. Wolverton, "First principles impurity diffusion coefficients," *Acta Materialia*, vol. 57, no. 14, pp. 4102 – 4108, 2009.

[79] M. Jin, P. Cao, S. Yip, and M. P. Short, "Radiation damage reduction by grain-boundary biased defect migration in nanocrystalline cu," *Acta Materialia*, vol. 155, pp. 410 – 417, 2018.

[80] T. D. Shen, S. Feng, M. Tang, J. A. Valdez, Y. Wang, and K. E. Sickafus, "Enhanced radiation tolerance in nanocrystalline MgGa2O4," *Applied Physics Letters*, vol. 90, no. 26, p. 263115, 2007.

[81] M. Demkowicz, R. Hoagland, and J. Hirth, "Interface structure and radiation damage resistance in cu-nb multilayer nanocomposites," *Physical Review Letters*, vol. 100, no. 13, p. 136102, 2008.

[82] E. M. Bringa, J. Monk, A. Caro, A. Misra, L. Zepeda-Ruiz, M. Duchaineau, F. Abraham, M. Nastasi, S. Picraux, Y. Wang, *et al.*, "Are nanoporous materials radiation resistant?," *Nano letters*, vol. 12, no. 7, pp. 3351–3355, 2011.

[83] G. Watkins and K. Brower, "Epr observation of the isolated interstitial carbon atom in silicon," *Physical Review Letters*, vol. 36, no. 22, p. 1329, 1976.

[84] K. Arakawa, K. Ono, M. Isshiki, K. Mimura, M. Uchikoshi, and H. Mori, "Observation of the one-dimensional diffusion of nanometer-sized dislocation loops," *Science*, vol. 318, no. 5852, pp. 956–959, 2007.

[85] C. Dai, P. Saidi, Z. Yao, and M. R. Daymond, "Atomistic simulations of ni segregation to irradiation induced dislocation loops in zr-ni alloys," *Acta Materialia*, vol. 140, pp. 56–66, 2017.

[86] W. Xu, Y. Zhang, G. Cheng, W. Jian, P. C. Millett, C. C. Koch, S. N. Mathaudhu, and Y. Zhu, "In-situ atomic-scale observation of irradiation-induced void formation," *Nature communications*, vol. 4, p. 2288, 2013.

[87] K. Yu, Y. Liu, C. Sun, H. Wang, L. Shao, E. Fu, and X. Zhang, "Radiation damage in helium ion irradiated nanocrystalline fe," *Journal of Nuclear Materials*, vol. 425, no. 1, pp. 140–146, 2012.

[88] D. Kiener, P. Hosemann, S. Maloy, and A. Minor, "In situ nano-compression testing of irradiated copper," *Nature Materials*, vol. 10, no. 8, p. 608, 2011.

[89] R. Barnes, "Embrittlement of stainless steels and nickel-based alloys at high temperature induced by neutron radiation," *Nature*, vol. 206, no. 4991, pp. 1307–1310, 1965.

[90] F. Garner, M. Toloczko, and B. Sencer, "Comparison of swelling and irradiation creep behavior of fcc-austenitic and bcc-ferritic/martensitic alloys at high neutron exposure," *Journal of Nuclear Materials*, vol. 276, no. 1-3, pp. 123–142, 2000.

[91] N. Li, K. Hattar, and A. Misra, "In situ probing of the evolution of irradiation-induced defects in copper," *Journal of Nuclear Materials*, vol. 439, no. 1, pp. 185–191, 2013.

[92] K. Yu, D. Bufford, F. Khatkhatay, H. Wang, M. Kirk, and X. Zhang, "In situ studies of irradiation-induced twin boundary migration in nanotwinned ag," *Scripta Materialia*, vol. 69, no. 5, pp. 385–388, 2013.

[93] J. Li, K. Yu, Y. Chen, M. Song, H. Wang, M. Kirk, M. Li, and X. Zhang, "In situ study of defect migration kinetics and self-healing of twin boundaries in heavy ion irradiated nanotwinned metals," *Nano letters*, vol. 15, no. 5, pp. 2922–2927, 2015.

[94] Y. Chen, J. Li, K. Yu, H. Wang, M. Kirk, M. Li, and X. Zhang, "In situ studies on radiation tolerance of nanotwinned cu," *Acta Materialia*, vol. 111, pp. 148–156, 2016.

[95] N. Li, J. Wang, Y. Wang, Y. Serruys, M. Nastasi, and A. Misra, "Incoherent twin boundary migration induced by ion irradiation in cu," *Journal of Applied Physics*, vol. 113, no. 2, p. 023508, 2013.

[96] Y. Chimi, A. Iwase, N. Ishikawa, M. Kobiyama, T. Inami, and S. Okuda, "Accumulation and recovery of defects in ion-irradiated nanocrystalline gold," *Journal of Nuclear Materials*, vol. 297, no. 3, pp. 355–357, 2001.

[97] K. Yu, D. Bufford, C. Sun, Y. Liu, H. Wang, M. Kirk, M. Li, and X. Zhang, "Removal of stacking-fault tetrahedra by twin boundaries in nanotwinned metals," *Nature Communication*, vol. 4, p. 1377, 2013.

[98] M. Samaras, P. Derlet, H. Van Swygenhoven, and M. Victoria, "Computer simulation of displacement cascades in nanocrystalline ni," *Physical Review Letters*, vol. 88, no. 12, p. 125505, 2002.

[99] M. Samaras, P. Derlet, H. Van Swygenhoven, and M. Victoria, "Atomic scale modelling of the primary damage state of irradiated fcc and bcc nanocrystalline metals," *Journal of Nuclear Materials*, vol. 351, no. 1, pp. 47–55, 2006.

[100] X.-M. Bai, L. J. Vernon, R. G. Hoagland, A. F. Voter, M. Nastasi, and B. P. Uberuaga, "Role of atomic structure on grain boundary-defect interactions in cu," *Physics Review B*, vol. 85, no. 21, p. 214103, 2012.

[101] M. J. Demkowicz, O. Anderoglu, X. Zhang, and A. Misra, "The influence of Σ3 twin boundaries on the formation of radiation-induced defect clusters in nanotwinned cu," *Journal of Materials Research*, vol. 26, no. 14, pp. 1666–1675, 2011.

[102] X.-M. Bai and B. P. Uberuaga, "The influence of grain boundaries on radiation-induced point defect production in materials: a review of atomistic studies," *Jom*, vol. 65, no. 3, pp. 360–373, 2013.

[103] D. Chen, J. Wang, T. Chen, and L. Shao, "Defect annihilation at grain boundaries in α-Fe," *Scientific Reports*, vol. 3, p. 1450, 2013.

[104] R. Schäublin, Z. Yao, N. Baluc, and M. Victoria, "Irradiation-induced stacking fault tetrahedra in fcc metals," *Philosophical Magazine*, vol. 85, no. 4-7, pp. 769–777, 2005.

[105] M. Niewczas and R. Hoagland, "Molecular dynamic studies of the interaction of a/6< 112> shockley dislocations with stacking fault tetrahedra in copper. part ii: Intersection of stacking fault tetrahedra by moving twin boundaries," *Philosophical Magazine*, vol. 89, no. 8, pp. 727–746, 2009.

[106] E. Martínez, B. P. Uberuaga, and I. J. Beyerlein, "Interaction of small mobile stacking fault tetrahedra with free surfaces, dislocations, and interfaces in cu and cu-nb," *Physics Review B*, vol. 93, no. 5, p. 054105, 2016.

[107] L. Zhang, C. Lu, K. Tieu, and Y. Shibuta, "Dynamic interaction between grain boundary and stacking fault tetrahedron," *Scripta Materialia*, vol. 144, pp. 78–83, 2018.

[108] Y. Mishin, M. Mehl, D. Papaconstantopoulos, A. Voter, and J. Kress, "Structural stability and lattice defects in copper: Ab initio, tight-binding, and embedded-atom calculations," *Physics Review B*, vol. 63, no. 22, p. 224106, 2001.

[109] J. Rittner and D. Seidman, "< 110> symmetric tilt grain-boundary structures in fcc metals with low stacking-fault energies," *Physics Review B*, vol. 54, no. 10, p. 6999, 1996.

[110] T. Frolov, D. L. Olmsted, M. Asta, and Y. Mishin, "Structural phase transformations in metallic grain boundaries," *Nature Communication*, vol. 4, p. 1899, 2013.

[111] L. Zhang, C. Lu, and K. Tieu, "Atomistic simulation of tensile deformation behavior of $\Sigma 5$ tilt grain boundaries in copper bicrystal," *Scientific Reports*, vol. 4, 2014.

[112] F. Aurenhammer, "Voronoi diagramsâĂŤa survey of a fundamental geometric data structure," *ACM Computing Surveys (CSUR)*, vol. 23, no. 3, pp. 345–405, 1991.

[113] S. Plimpton, "Fast parallel algorithms for short-range molecular dynamics," *Journal of Computational Physics*, vol. 117, no. 1, pp. 1–19, 1995.

[114] M. W. Ullah, Y. Zhang, N. Sellami, A. Debelle, H. Bei, and W. J. Weber, "Evolution of irradiation-induced strain in an equiatomic nife alloy," *Scripta Materialia*, vol. 140, pp. 35–39, 2017.

[115] A. Stukowski, "Visualization and analysis of atomistic simulation data with ovito–the open visualization tool," *Modelling and Simulation in Materials Science and Engineering*, vol. 18, no. 1, p. 015012, 2009.

[116] "Data repository for nanocrystalline cu radiation manuscript, available at," 2018. https://doi.org/10.5281/zenodo.1239133.

[117] D. L. Olmsted, S. M. Foiles, and E. A. Holm, "Survey of computed grain boundary properties in face-centered cubic metals: I. grain boundary energy," *Acta Materialia*, vol. 57, no. 13, pp. 3694–3703, 2009.

[118] B. Uberuaga, R. Hoagland, A. Voter, and S. Valone, "Direct transformation of vacancy voids to stacking fault tetrahedra," *Physical Review Letters*, vol. 99, no. 13, p. 135501, 2007.

[119] J. Hirth and J. Lothe, "Theory of dislocations, 2nd," *Ed.: John Willey & Sons*, 1982.

[120] M. Sabochick and S. Yip, "Migration energy calculations for small vacancy clusters in copper," *Journal of Physics F: Metal Physics*, vol. 18, no. 8, p. 1689, 1988.

[121] E. Martínez and B. P. Uberuaga, "Mobility and coalescence of stacking fault tetrahedra in Cu," *Scientific Reports*, vol. 5, 2015.

[122] A. Vattré, T. Jourdan, H. Ding, M.-C. Marinica, and M. Demkowicz, "Non-random walk diffusion enhances the sink strength of semicoherent interfaces," *Nature Communication*, vol. 7, p. 10424, 2016.

[123] M. Rose, A. Balogh, and H. Hahn, "Instability of irradiation induced defects in nanostructured materials," *Nuclear Instruments and Methods in Physics Research Section B: Beam Interactions with Materials and Atoms*, vol. 127, pp. 119–122, 1997.

[124] M. A. Tschopp, K. Solanki, F. Gao, X. Sun, M. A. Khaleel, and M. Horstemeyer, "Probing grain boundary sink strength at the nanoscale: Energetics and length scales of vacancy and interstitial absorption by grain boundaries in α-fe," *Physics Review B*, vol. 85, no. 6, p. 064108, 2012.

[125] W. Han, M. Demkowicz, E. Fu, Y. Wang, and A. Misra, "Effect of grain boundary character on sink efficiency," *Acta Materialia*, vol. 60, no. 18, pp. 6341–6351, 2012.

[126] B. P. Uberuaga, L. J. Vernon, E. Martinez, and A. F. Voter, "The relationship between grain boundary structure, defect mobility, and grain boundary sink efficiency," *Scientific Reports*, vol. 5, 2015.

[127] A. Khalajhedayati, Z. Pan, and T. J. Rupert, "Manipulating the interfacial structure of nanomaterials to achieve a unique combination of strength and ductility," *Nature communications*, vol. 7, p. 10802, 2016.

[128] D. Kaoumi, A. Motta, and R. Birtcher, "A thermal spike model of grain growth under irradiation," *Journal of Applied Physics*, vol. 104, no. 7, p. 073525, 2008.

[129] K. P. So, D. Chen, A. Kushima, M. Li, S. Kim, Y. Yang, Z. Wang, J. G. Park, Y. H. Lee, R. I. Gonzalez, M. Kiwi, E. M. Bringa, L. Shao, and J. Li, "Dispersion of carbon nanotubes in aluminum improves radiation resistance," *Nano Energy*, vol. 22, no. Supplement C, pp. 319 – 327, 2016.

[130] W. Han, M. J. Demkowicz, N. A. Mara, E. Fu, S. Sinha, A. D. Rollett, Y. Wang, J. S. Carpenter, I. J. Beyerlein, and A. Misra, "Design of radiation tolerant materials via interface engineering," *Advanced materials*, vol. 25, no. 48, pp. 6975–6979, 2013.

[131] R. Klueh, J. Shingledecker, R. Swindeman, and D. Hoelzer, "Oxide dispersion-strengthened steels: A comparison of some commercial and experimental alloys," *Journal of Nuclear Materials*, vol. 341, no. 2, pp. 103–114, 2005.

[132] M. Jin, P. Cao, and M. P. Short, "Mechanisms of grain boundary migration and growth in nanocrystalline metals under irradiation," *Scripta Materialia*, vol. 163, pp. 66–70, 2019.

[133] N. Petch, "The cleavage strength of polycrystals," *Journal of the Iron and Steel Institute*, vol. 174, pp. 25–28, 1953.

[134] G. Gottstein and L. S. Shvindlerman, *Grain boundary migration in metals: thermodynamics, kinetics, applications.* CRC press, 2009.

[135] T. Rupert, D. Gianola, Y. Gan, and K. Hemker, "Experimental observations of stress-driven grain boundary migration," *Science*, vol. 326, no. 5960, pp. 1686–1690, 2009.

[136] H. Zhang, M. Upmanyu, and D. Srolovitz, "Curvature driven grain boundary migration in aluminum: molecular dynamics simulations," *Acta Materialia*, vol. 53, no. 1, pp. 79–86, 2005.

[137] M. Tonks, P. Millett, W. Cai, and D. Wolf, "Analysis of the elastic strain energy driving force for grain boundary migration using phase field simulation," *Scripta Materialia*, vol. 63, no. 11, pp. 1049–1052, 2010.

[138] J. C. Liu, M. Nastasi, and J. Mayer, "Ion irradiation induced grain growth in pd polycrystalline thin films," *Journal of Applied Physics*, vol. 62, no. 2, pp. 423–428, 1987.

[139] J. C. Liu and J. Mayer, "Ion irradiation induced grain growth in ni polycrystalline thin films," *Nuclear Instruments and Methods in Physics Research Section B: Beam Interactions with Materials and Atoms*, vol. 19, pp. 538–542, 1987.

[140] D. E. Alexander and G. S. Was, "Thermal-spike treatment of ion-induced grain growth: Theory and experimental comparison," *Physical Review B*, vol. 47, no. 6, p. 2983, 1993.

[141] W. Voegeli, K. Albe, and H. Hahn, "Simulation of grain growth in nanocrystalline nickel induced by ion irradiation," *Nuclear Instruments and Methods in Physics Research Section B: Beam Interactions with Materials and Atoms*, vol. 202, pp. 230–235, 2003.

[142] D. Kaoumi, A. Motta, and R. Birtcher, "Grain growth in nanocrystalline metal thin films under in situ ion-beam irradiation," in *Effects of Radiation on Materials: 23rd International Symposium*, ASTM International, 2008.

[143] J. W. Cahn, Y. Mishin, and A. Suzuki, "Coupling grain boundary motion to shear deformation," *Acta Materialia*, vol. 54, no. 19, pp. 4953–4975, 2006.

[144] H. Zhang, M. Mendelev, and D. Srolovitz, "Computer simulation of the elastically driven migration of a flat grain boundary," *Acta Materialia*, vol. 52, no. 9, pp. 2569–2576, 2004.

[145] W. Yu and M. Demkowicz, "Non-coherent cu grain boundaries driven by continuous vacancy loading," *Journal of Materials Science*, vol. 50, no. 11, pp. 4047–4065, 2015.

[146] Z. T. Trautt, M. Upmanyu, and A. Karma, "Interface mobility from interface random walk," *Science*, vol. 314, no. 5799, pp. 632–635, 2006.

[147] R. W. Balluffi, S. Allen, and W. C. Carter, *Kinetics of materials*. John Wiley & Sons, 2005.

[148] S. P. Hau-Riege and C. V. Thompson, "In situ transmission electron microscope studies of the kinetics of abnormal grain growth in electroplated copper films," *Applied Physics Letters*, vol. 76, no. 3, pp. 309–311, 2000.

[149] K. Hattar, D. Follstaedt, J. Knapp, and I. Robertson, "Defect structures created during abnormal grain growth in pulsed-laser deposited nickel," *Acta Materialia*, vol. 56, no. 4, pp. 794–801, 2008.

[150] D. Srinivasan, R. Corderman, and P. Subramanian, "Strengthening mechanisms (via hardness analysis) in nanocrystalline nicr with nanoscaled Y2O3 and Al2O3 dispersoids," *Materials Science and Engineering: A*, vol. 416, no. 1-2, pp. 211–218, 2006.

[151] D. Kudashov, H. Baum, U. Martin, M. Heilmaier, and H. Oettel, "Microstructure and room temperature hardening of ultra-fine-grained oxide-dispersion strengthened copper prepared by cryomilling," *Materials Science and Engineering: A*, vol. 387, pp. 768–771, 2004.

[152] S. Brandstetter, K. Zhang, A. Escuadro, J. Weertman, and H. Van Swygenhoven, "Grain coarsening during compression of bulk nanocrystalline nickel and copper," *Scripta Materialia*, vol. 58, no. 1, pp. 61–64, 2008.

[153] Y. Zhang, G. J. Tucker, and J. R. Trelewicz, "Stress-assisted grain growth in nanocrystalline metals: Grain boundary mediated mechanisms and stabilization through alloying," *Acta Materialia*, vol. 131, pp. 39–47, 2017.

[154] D. Gianola, B. Mendis, X. Cheng, and K. Hemker, "Grain-size stabilization by impurities and effect on stress-coupled grain growth in nanocrystalline al thin films," *Materials Science and Engineering: A*, vol. 483, pp. 637–640, 2008.

[155] A. R. Kalidindi and C. A. Schuh, "Stability criteria for nanocrystalline alloys," *Acta Materialia*, vol. 132, pp. 128–137, 2017.

[156] N. Zhou, T. Hu, J. Huang, and J. Luo, "Stabilization of nanocrystalline alloys at high temperatures via utilizing high-entropy grain boundary complexions," *Scripta Materialia*, vol. 124, pp. 160–163, 2016.

[157] V. Borovikov, M. I. Mendelev, and A. H. King, "Effects of stable and unstable stacking fault energy on dislocation nucleation in nano-crystalline metals," *Modelling and Simulation in Materials Science and Engineering*, vol. 24, no. 8, p. 085017, 2016.

[158] Y. Wang, J. Li, A. V. Hamza, and T. W. Barbee, "Ductile crystalline–amorphous nanolaminates," *Proceedings of the National Academy of Sciences*, vol. 104, no. 27, pp. 11155–11160, 2007.

[159] Z. Pan and T. J. Rupert, "Amorphous intergranular films as toughening structural features," *Acta Materialia*, vol. 89, pp. 205–214, 2015.

[160] W. Johnson, Y. Cheng, M. Van Rossum, and M. Nicolet, "When is thermodynamics relevant to ion-induced atomic rearrangements in metals?," *Nuclear Instruments and Methods in Physics Research Section B: Beam Interactions with Materials and Atoms*, vol. 7, pp. 657–665, 1985.

[161] T. Workman, Y. Cheng, W. Johnson, and M.-A. Nicolet, "Effect of thermodynamics on ion mixing," *Applied physics letters*, vol. 50, no. 21, pp. 1485–1487, 1987.

[162] E. Martinez and B. P. Uberuaga, "Mobility and coalescence of stacking fault tetrahedra in cu," *Sci. Rep.*, vol. 5, p. 9084, 2015.

[163] M. R. So/rensen and A. F. Voter, "Temperature-accelerated dynamics for simulation of infrequent events," *The Journal of Chemical Physics*, vol. 112, no. 21, pp. 9599–9606, 2000.

[164] A. F. Voter, "Parallel replica method for dynamics of infrequent events," *Physical Review B*, vol. 57, no. 22, p. R13985, 1998.

[165] A. F. Voter, "Hyperdynamics: Accelerated molecular dynamics of infrequent events," *Physical Review Letters*, vol. 78, no. 20, p. 3908, 1997.

[166] M. Jin, C. Permann, and M. P. Short, "Breaking the power law: Multiscale simulations of self-ion irradiated tungsten," *Journal of Nuclear Materials*, vol. 504, pp. 33–40, 2018.

[167] K. Ikeda, "Progress in the iter physics basis," *Nucl. Fusion*, vol. 47, no. 6, 2007.

[168] V. Barabash, G. Federici, M. Rödig, L. Snead, and C. Wu, "Neutron irradiation effects on plasma facing materials," *Journal of Nuclear Materials*, vol. 283–287, Part 1, pp. 138 – 146, 2000.

[169] L. Keys and J. Moteff, "Neutron irradiation and defect recovery of tungsten," *Journal of Nuclear Materials*, vol. 34, no. 3, pp. 260 – 280, 1970.

[170] X. Yi, A. Sand, D. Mason, M. Kirk, S. Roberts, K. Nordlund, and S. Dudarev, "Direct observation of size scaling and elastic interaction between nano-scale defects in collision cascades," *EPL (Europhysics Letters)*, vol. 110, no. 3, p. 36001, 2015.

[171] Y.-W. Kim and J. Galligan, "Radiation damage and stage iii defect annealing in thermal neutron irradiated tungsten," *Acta Metallurgica*, vol. 26, no. 3, pp. 379 – 390, 1978.

[172] O. Ogorodnikova, Y. Gasparyan, V. Efimov, Ł. CiupiÅĎski, and J. Grzonka, "Annealing of radiation-induced damage in tungsten under and after irradiation with 20 mev self-ions," *Journal of Nuclear Materials*, vol. 451, no. 1–3, pp. 379 – 386, 2014.

[173] D. E. J. Armstrong, P. D. Edmondson, and S. G. Roberts, "Effects of sequential tungsten and helium ion implantation on nano-indentation hardness of tungsten," *Applied Physics Letters*, vol. 102, no. 25, p. 251901, 2013.

[174] A. E. Sand, S. L. Dudarev, and K. Nordlund, "High-energy collision cascades in tungsten: Dislocation loops structure and clustering scaling laws," *EPL (Europhysics Letters)*, vol. 103, no. 4, p. 46003, 2013.

[175] N. Juslin and B. Wirth, "Interatomic potentials for simulation of he bubble formation in w," *Journal of Nuclear Materials*, vol. 432, no. 1, pp. 61–66, 2013.

[176] X. Yang and A. Hassanein, "Atomic scale calculations of tungsten surface binding energy and beryllium-induced tungsten sputtering," *Applied Surface Science*, vol. 293, pp. 187–190, 2014.

[177] S. Han, L. A. Zepeda-Ruiz, G. J. Ackland, R. Car, and D. J. Srolovitz, "Interatomic potential for vanadium suitable for radiation damage simulations," *Journal of Applied Physics*, vol. 93, no. 6, pp. 3328–3335, 2003.

[178] M.-C. Marinica, L. Ventelon, M. Gilbert, L. Proville, S. Dudarev, J. Marian, G. Bencteux, and F. Willaime, "Interatomic potentials for modelling radiation defects and dislocations in tungsten," *Journal of Physics: Condensed Matter*, vol. 25, no. 39, p. 395502, 2013.

[179] D. R. Gaston, C. J. Permann, J. W. Peterson, A. E. Slaughter, D. Andrš, Y. Wang, M. P. Short, D. M. Perez, M. R. Tonks, J. Ortensi, *et al.*, "Physics-based multiscale coupling for full core nuclear reactor simulation," *Annals of Nuclear Energy*, vol. 84, pp. 45–54, 2015.

[180] S. Golubov, A. Ovcharenko, A. Barashev, and B. Singh, "Grouping method for the approximate solution of a kinetic equation describing the evolution of point-defect clusters," *Philosophical Magazine A*, vol. 81, no. 3, pp. 643–658, 2001.

[181] A. Ovcharenko, S. Golubov, C. Woo, and H. Huang, "Gmic++: grouping method in c++: an efficient method to solve large number of master equations," *Computer Physics Communications*, vol. 152, no. 2, pp. 208–226, 2003.

[182] W. H. Zhou, C. G. Zhang, Y. G. Li, and Z. Zeng, "Creeping motion of self interstitial atom clusters in tungsten," *Scientific Reports*, vol. 4, 2014.

[183] P. M. Derlet, D. Nguyen-Manh, and S. Dudarev, "Multiscale modeling of crowdion and vacancy defects in body-centered-cubic transition metals," *Physics Review B*, vol. 76, no. 5, p. 054107, 2007.

[184] A. A. Kohnert and B. D. Wirth, "Cluster dynamics models of irradiation damage accumulation in ferritic iron. ii. effects of reaction dimensionality," *Journal of Applied Physics*, vol. 117, no. 15, p. 154306, 2015.

[185] M. Jin, C. Permann, and M. P. Short, "Geminio 2.0 - A MOOSE-based cluster dynamics code." GitHub Repository, DOI: 10.5281/zenodo.495710, 2017. https://github.com/shortlab/geminio.

[186] N. Budylkin, E. Mironova, V. Chernov, V. Krasnoselov, S. Porollo, and F. Garner, "Neutron-induced swelling and embrittlement of pure iron and pure nickel irradiated in the bn-350 and bor-60 fast reactors," *Journal of Nuclear Materials*, vol. 375, no. 3, pp. 359 – 364, 2008.

[187] D. Bacon, F. Gao, and Y. Osetsky, "The primary damage state in fcc, bcc and hcp metals as seen in molecular dynamics simulations," *Journal of Nuclear Materials*, vol. 276, no. 1–3, pp. 1–12, 2000.

[188] A. E. Sand, M. Aliaga, M. J. Caturla, and K. Nordlund, "Surface effects and statistical laws of defects in primary radiation damage: Tungsten vs. iron," *EPL (Europhysics Letters)*, vol. 115, no. 3, p. 36001, 2016.

[189] B. Wirth, G. Odette, D. Maroudas, and G. Lucas, "Dislocation loop structure, energy and mobility of self-interstitial atom clusters in bcc iron," *Journal of Nuclear Materials*, vol. 276, no. 1, pp. 33–40, 2000.

[190] S. Takaki, J. Fuss, H. Kuglers, U. Dedek, and H. Schultz, "The resistivity recovery of high purity and carbon doped iron following low temperature electron irradiation," *Radiation effects*, vol. 79, no. 1-4, pp. 87–122, 1983.

[191] X.-S. Kong, Y.-W. You, C. Song, Q. Fang, J.-L. Chen, G.-N. Luo, and C. Liu, "First principles study of foreign interstitial atom (carbon, nitrogen) interactions with intrinsic defects in tungsten," *Journal of Nuclear Materials*, vol. 430, no. 1, pp. 270–278, 2012.

[192] C. Becquart and C. Domain, "Solute–point defect interactions in bcc systems: Focus on first principles modelling in w and rpv steels," *Current Opinion in Solid State and Materials Science*, vol. 16, no. 3, pp. 115–125, 2012.

[193] A. Sand, S. Dudarev, and K. Nordlund, "High-energy collision cascades in tungsten: Dislocation loops structure and clustering scaling laws," *EPL (Europhysics Letters)*, vol. 103, no. 4, p. 46003, 2013.

[194] A. E. Sand, D. R. Mason, A. D. Backer, X. Yi, S. L. Dudarev, and K. Nordlund, "Cascade fragmentation: deviation from power law in primary radiation damage," *Materials Research Letters*, 2017.

[195] D. Xu, X. Hu, and B. D. Wirth, "A phase-cut method for multi-species kinetics: Sample application to nanoscale defect cluster evolution in alpha iron following helium ion implantation," *Applied Physics Letters*, vol. 102, no. 1, p. 011904, 2013.

[196] S. Golubov, R. Stoller, S. Zinkle, and A. Ovcharenko, "Kinetics of coarsening of helium bubbles during implantation and post-implantation annealing," *Journal of Nuclear Materials*, vol. 361, no. 2–3, pp. 149 – 159, 2007.

[197] J. Marian and T. L. Hoang, "Modeling fast neutron irradiation damage accumulation in tungsten," *Journal of Nuclear Materials*, vol. 429, no. 1–3, pp. 293–297, 2012.

[198] S. Golubov, R. Stoller, S. Zinkle, and A. Ovcharenko, "Kinetics of coarsening of helium bubbles during implantation and post-implantation annealing," *Journal of Nuclear Materials*, vol. 361, no. 2-3, pp. 149–159, 2007.

[199] F. Christien and A. Barbu, "Cluster dynamics modelling of irradiation growth of zirconium single crystals," *Journal of Nuclear Materials*, vol. 393, no. 1, pp. 153–161, 2009.

[200] A. H. Duparc, C. Moingeon, N. Smetniansky-de Grande, and A. Barbu, "Microstructure modelling of ferritic alloys under high flux 1 mev electron irradiations," *Journal of Nuclear Materials*, vol. 302, no. 2-3, pp. 143–155, 2002.

[201] L. Shao, C.-C. Wei, J. Gigax, A. Aitkaliyeva, D. Chen, B. Sencer, and F. Garner, "Effect of defect imbalance on void swelling distributions produced in pure iron irradiated with 3.5 mev self-ions," *Journal of Nuclear Materials*, vol. 453, no. 1-3, pp. 176–181, 2014.

[202] A. Souidi, M. Hou, C. S. Becquart, L. Malerba, C. Domain, and R. E. Stoller, "On the correlation between primary damage and long-term nanostructural evolution in iron under irradiation," *Journal of Nuclear Materials*, vol. 419, no. 1-3, pp. 122–133, 2011.

[203] C. Björkas, K. Nordlund, and M. J. Caturla, "Influence of the picosecond defect distribution on damage accumulation in irradiated α-fe," *Physical Review B*, vol. 85, no. 2, p. 024105, 2012.

[204] M. Short, D. Gaston, M. Jin, L. Shao, and F. Garner, "Modeling injected interstitial effects on void swelling in self-ion irradiation experiments," *Journal of Nuclear Materials*, vol. 471, pp. 200–207, 2016.

[205] B. Michaut, T. Jourdan, J. Malaplate, A. Renault-Laborne, F. Sefta, and B. Décamps, "Cluster dynamics modeling and experimental investigation of the effect of injected interstitials," *Journal of Nuclear Materials*, vol. 496, pp. 166–176, 2017.

[206] G. Lucas, "The evolution of mechanical property change in irradiated austenitic stainless steels," *Journal of Nuclear Materials*, vol. 206, no. 2-3, pp. 287–305, 1993.

[207] K. Murty and I. Charit, "Structural materials for gen-iv nuclear reactors: Challenges and opportunities," *Journal of Nuclear Materials*, vol. 383, no. 1-2, pp. 189–195, 2008.

[208] L. Tan, R. E. Stoller, K. G. Field, Y. Yang, H. Nam, D. Morgan, B. Wirth, M. Gussev, and J. Busby, "Microstructural evolution of type 304 and 316 stainless steels under neutron irradiation at lwr relevant conditions," *JOM*, vol. 68, no. 2, pp. 517–529, 2016.

[209] T. Faney and B. Wirth, "Spatially dependent cluster dynamics modeling of microstructure evolution in low energy helium irradiated tungsten," *Modelling and Simulation in Materials Science and Engineering*, vol. 22, no. 6, p. 065010, 2014.

[210] C. Barouh, T. Schuler, C.-C. Fu, and T. Jourdan, "Predicting vacancy-mediated diffusion of interstitial solutes in α-fe," *Physical Review B*, vol. 92, no. 10, p. 104102, 2015.

[211] A. A. Kohnert, B. D. Wirth, and L. Capolungo, "Modeling microstructural evolution in irradiated materials with cluster dynamics methods: A review," *Computational Materials Science*, vol. 149, pp. 442–459, 2018.

[212] X.-L. Yu, B. Yi, and X.-Y. Wang, "Prediction of the glass transition temperatures for polymers with artificial neural network," *Journal of Theoretical and Computational Chemistry*, vol. 7, no. 05, pp. 953–963, 2008.

[213] P. Raccuglia, K. C. Elbert, P. D. Adler, C. Falk, M. B. Wenny, A. Mollo, M. Zeller, S. A. Friedler, J. Schrier, and A. J. Norquist, "Machine-learning-assisted materials discovery using failed experiments," *Nature*, vol. 533, no. 7601, p. 73, 2016.

[214] C. E. Mohn and W. Kob, "A genetic algorithm for the atomistic design and global optimisation of substitutionally disordered materials," *Computational Materials Science*, vol. 45, no. 1, pp. 111–117, 2009.

[215] N. Castin, M. I. Pascuet, L. Messina, C. Domain, P. Olsson, R. C. Pasianot, and L. Malerba, "Advanced atomistic models for radiation damage in fe-based alloys: Contributions and future perspectives from artificial neural networks," *Computational Materials Science*, vol. 148, pp. 116–130, 2018.

[216] J. Mathew, D. Parfitt, K. Wilford, N. Riddle, M. Alamaniotis, A. Chroneos, and M. Fitzpatrick, "Reactor pressure vessel embrittlement: Insights from neural network modelling," *Journal of Nuclear Materials*, vol. 502, pp. 311–322, 2018.

[217] N. Castin, L. Malerba, and R. Chaouadi, "Prediction of radiation induced hardening of reactor pressure vessel steels using artificial neural networks," *Journal of Nuclear Materials*, vol. 408, no. 1, pp. 30–39, 2011.

[218] G. Cottrell, R. Kemp, H. Bhadeshia, G. Odette, and T. Yamamoto, "Neural network analysis of charpy transition temperature of irradiated low-activation martensitic steels," *Journal of Nuclear Materials*, vol. 367, pp. 603–609, 2007.

[219] F. Pedregosa, G. Varoquaux, A. Gramfort, V. Michel, B. Thirion, O. Grisel, M. Blondel, P. Prettenhofer, R. Weiss, V. Dubourg, *et al.*, "Scikit-learn: Machine learning in python," *Journal of machine learning research*, vol. 12, no. Oct, pp. 2825–2830, 2011.

[220] M. Abadi, P. Barham, J. Chen, Z. Chen, A. Davis, J. Dean, M. Devin, S. Ghemawat, G. Irving, M. Isard, *et al.*, "Tensorflow: a system for large-scale machine learning.," in *OSDI*, vol. 16, pp. 265–283, 2016.

[221] J. Straalsund, R. Powell, and B. Chin, "An overview of neutron irradiation effects in lmfbr materials," *Journal of Nuclear Materials*, vol. 108, 1982.

[222] M. Makin, G. Walters, and A. Foreman, "The void swelling behaviour of electron irradiated type 316 austenitic steel," *Journal of Nuclear Materials*, vol. 95, no. 1-2, pp. 155–170, 1980.

[223] G. M. Bond, B. H. Sencer, F. A. Garner, M. L. Hamilton, T. R. Allen, and D. L. Porter, "Void swelling of annealed 304 stainless steel at âĹij 370-385 ^{o}C and pwr-relevant displacement rates," in *Ninth International Symposium on Environmental Degradation of Materials in Nuclear Power SystemsâĂŤWater Reactors*, pp. 1045–1050, 2013.

[224] T. Okita, T. Sato, N. Sekimura, F. A. Garner, L. R. Greenwood, W. Wolfer, and Y. Isobe, "Neutron-induced microstructural evolution of Fe-15Cr-16Ni alloys at 400 ^{o}C during neutron irradiation in the FFTF fast reactor," 2001.

[225] D. Mazey, J. Hudson, and R. Nelson, "The dose dependence of void swelling in AISI 316 stainless steel during 20 MeV C++ irradiation at 525 ^{o}C," *Journal of Nuclear Materials*, vol. 41, no. 3, pp. 257–273, 1971.

[226] T. Williams, D. Arkell, and B. Eyre, "The void-swelling behaviour of solution-treated FV548 stainless steel irradiated with 22 MeV C2+ and 46.5 MeV Ni6+ ions and the influence of heat-treatment," *Journal of Nuclear Materials*, vol. 68, no. 1, pp. 69–81, 1977.

[227] F. Smidt, P. Malmberg, J. Sprague, and J. Westmoreland, "Swelling behavior of commercial ferritic alloys, EM-12 and HT-9, as assessed by heavy ion bombardment," in *Irradiation Effects on the Microstructure and Properties of Metals*, ASTM International, 1976.

[228] F. Garner and D. Gelles, "Neutron-induced swelling of commercial alloys at very high exposures," in *Effects of Radiation on Materials: 14th International Symposium (Volume II)*, ASTM International, 1990.

[229] B. J. Makenas, "Swelling of 20% cold-worked type 316 stainless steel fuel pin cladding and ducts," in *Effects of Radiation on Materials: Twelfth International Symposium*, ASTM International, 1985.

[230] B. H. Sencer and F. A. Garner, "Compositional and temperature dependence of void swelling in model Fe–Cr base alloys irradiated in the EBR-II fast reactor," *Journal of Nuclear Materials*, vol. 283, pp. 164–168, 2000.

[231] M. Fujiwara, H. Uchida, S. Ohta, S. Yuhara, S. Tani, and Y. Sato, "Development of modified type 316 stainless steel for fast breeder reactor fuel cladding tubes," in *Radiation-Induced Changes in Microstructure: 13th International Symposium (Part I)*, ASTM International, 1987.

[232] N. Igata, Y. Kohno, and J.-i. Nishimura, "Dislocation behavior in the swelling process of hvem irradiated stainless steel," in *Radiation-Induced Changes in Microstructure: 13th International Symposium (Part I)*, ASTM International, 1987.

[233] F. Rotman and O. Dimitrov, "Void swelling in electron-irradiated Fe-Cr-Ni model alloys," in *Radiation-Induced Changes in Microstructure: 13th International Symposium (Part I)*, ASTM International, 1987.

[234] X. Wang, A. M. Monterrosa, F. Zhang, H. Huang, Q. Yan, Z. Jiao, G. S. Was, and L. Wang, "Void swelling in high dose ion-irradiated reduced activation ferritic–martensitic steels," *Journal of Nuclear Materials*, vol. 462, pp. 119–125, 2015.

[235] E. Getto, Z. Jiao, A. Monterrosa, K. Sun, and G. Was, "Effect of pre-implanted helium on void swelling evolution in self-ion irradiated HT9," *Journal of Nuclear Materials*, vol. 462, pp. 458–469, 2015.

[236] J. Kai and G. Kulcinski, "14 MeV nickel-ion irradiated HT-9 ferritic steel with and without helium pre-implantation," *Journal of Nuclear Materials*, vol. 175, no. 3, pp. 227–236, 1990.

[237] V. Kozlov and I. Portnykh, "Dependence of steady-state radiation swelling rate of l 0.1 C–16Cr–15Ni–2Mo–2Mn–Ti–Si austenitic steel on dpa rate and irradiation temperature," *Journal of Nuclear Materials*, vol. 386, pp. 147–151, 2009.

[238] T. Okita, N. Sekimura, and F. Garner, "Effects of dpa rate on swelling in neutron-irradiated Fe–Cr and Fe–Cr–Mo alloys," *Journal of Nuclear Materials*, vol. 417, no. 1-3, pp. 944–948, 2011.

[239] T. Okita, N. Sekimura, and F. Garner, "The conflicting roles of boron on the radiation response of precipitate-forming austenitic alloys," 2007.

[240] S. Porollo, Y. V. Konobeev, and F. Garner, "Swelling and microstructure of austenitic stainless steel ChS-68 CW after high dose neutron irradiation," *Journal of Nuclear Materials*, vol. 393, no. 1, pp. 61–66, 2009.

[241] E. Shcherbakov, A. Kozlov, P. Yagovitin, M. Evseev, E. Kinev, V. Panchenko, I. Isobe, M. Sagisaka, T. Okita, N. Sekimura, *et al.*, "Influence of damage rate on physical and mechanical properties and swelling of 18Cr–9Ni austenitic steel in the range of 3×10^{-9} to 4×10^{-8} dpa/s," *Journal of Nuclear Materials*, vol. 386, pp. 152–156, 2009.

[242] A. Kalchenko, V. Bryk, N. Lazarev, I. Neklyudov, V. Voyevodin, and F. Garner, "Prediction of swelling of 18Cr10NiTi austenitic steel over a wide range of displacement rates," *Journal of Nuclear Materials*, vol. 399, no. 1, pp. 114–121, 2010.

[243] Y. Murase, J. Nagakawa, N. Yamamoto, and H. Shiraishi, "Void swelling in Fe–15Cr–xNi ternary alloys under proton irradiation," *Journal of Nuclear Materials*, vol. 255, no. 1, pp. 34–43, 1998.

[244] B. Liu, S. Lai, J. Sun, C. Shang, and D. Xu, "Void swelling induced by 1 mev electron irradiation in Ti-and Nb-modified 316 stainless steels," *Journal of Nuclear Materials*, vol. 175, no. 1-2, pp. 129–134, 1990.

[245] M. Victoria, W. V. Green, B. N. Singh, and T. Leffers, "Nucleation, growth, and distribution of cavities in the vicinity of grain boundaries in aluminum irradiated with 600-MeV protons," in *Radiation-Induced Changes in Microstructure: 13th International Symposium (Part I)*, ASTM International, 1987.

[246] F. A. Garner and A. S. Kumar, "The influence of both major and minor element composition on void swelling in austenitic steels," in *Radiation-Induced Changes in Microstructure: 13th International Symposium (Part I)*, ASTM International, 1987.

[247] S. McDonald and A. Taylor, "Void swelling behavior of types 304 and 316 stainless steel irradiated with 4-MeV Ni+ ions," in *Effects of Radiation on Substructure and Mechanical Properties of Metals and Alloys*, ASTM International, 1973.

[248] J. Gigax, T. Chen, H. Kim, J. Wang, L. Price, E. Aydogan, S. A. Maloy, D. Schreiber, M. Toloczko, F. Garner, *et al.*, "Radiation response of alloy t91 at damage levels up to 1000 peak dpa," *Journal of Nuclear Materials*, vol. 482, pp. 257–265, 2016.

[249] E. Aydogan, T. Chen, J. Gigax, D. Chen, X. Wang, P. Dzhumaev, O. Emelyanova, M. Ganchenkova, B. Kalin, M. Leontiva-Smirnova, *et al.*, "Effect of self-ion irradiation on the microstructural changes of alloy ek-181 in annealed and severely deformed conditions," *Journal of Nuclear Materials*, vol. 487, pp. 96–104, 2017.

[250] P. Dubuisson, A. Maillard, C. Delalande, D. Gilbon, and J.-L. Seran, "The effect of phosphorus on the radiation-induced microstructure of stabilized austenitic stainless steels," in *Effects of Radiation on Materials: 15th International Symposium*, ASTM International, 1992.

[251] J. L. Seran and J. M. Dupouy, "The swelling of solution annealed 316 cladding in RAPSODIE and PHENIX," in *Effects of Radiation on Materials*, ASTM International, 1982.

[252] J. Seran, V. Levy, D. Gilbon, A. Maillard, A. Fissolo, H. Touron, R. Cauvin, A. Chalony, and E. Le Boulbin, "Behavior under neutron irradiation of the 15-15Ti and EM10 steels used as standard materials of the Phénix fuel sub-assembly," in *Effects of Radiation on Materials: 15th International Symposium*, ASTM International, 1992.

[253] F. Garner and H. Brager, "The role of phosphorus in the swelling and creep of irradiated austenitic alloys," *Journal of Nuclear Materials*, vol. 133, pp. 511–514, 1985.

[254] F. Garner, H. Brager, and R. Puigh, "Swelling behavior of titanium-modified alloys in EBR-II," *Journal of Nuclear Materials*, vol. 133, pp. 535–539, 1985.

[255] F. A. Garner and H. R. Brager, "Swelling of austenitic iron-nickel-chromium ternary alloys during fast neutron irradiation," in *Effects of Radiation on Materials: Twelfth International Symposium*, ASTM International, 1985.

[256] M. Jin, P. Cao, and M. Short, "Data repository for this manuscript, available at https://doi.org/10.5281/zenodo.2529461," 2018.

[257] T. G. Dietterich, "Ensemble methods in machine learning," in *International workshop on multiple classifier systems*, pp. 1–15, Springer, 2000.

[258] L. Breiman, "Random forests," *Machine learning*, vol. 45, no. 1, pp. 5–32, 2001.

[259] P. Geurts, D. Ernst, and L. Wehenkel, "Extremely randomized trees," *Machine learning*, vol. 63, no. 1, pp. 3–42, 2006.

[260] J. H. Friedman, "Greedy function approximation: a gradient boosting machine," *Annals of statistics*, pp. 1189–1232, 2001.

[261] C. M. Bishop *et al.*, *Neural networks for pattern recognition*. Oxford university press, 1995.

[262] F. A. Garner and H. R. Brager, "Swelling of austenitic iron-nickel-chromium ternary alloys during fast neutron irradiation," in *Effects of Radiation on Materials: Twelfth International Symposium*, ASTM International, 1985.

[263] Y. Zhang, T. T. Zuo, Z. Tang, M. C. Gao, K. A. Dahmen, P. K. Liaw, and Z. P. Lu, "Microstructures and properties of high-entropy alloys," *Progress in Materials Science*, vol. 61, pp. 1–93, 2014.

[264] G. R. Odette and D. T. Hoelzer, "Irradiation-tolerant nanostructured ferritic alloys: Transforming helium from a liability to an asset," *Jom*, vol. 62, no. 9, pp. 84–92, 2010.

[265] T. P. Schulze, "Efficient kinetic monte carlo simulation," *Journal of Computational Physics*, vol. 227, no. 4, pp. 2455–2462, 2008.

[266] N. Castin and L. Malerba, "Modeling radiation-induced segregation and precipitation: Contributions and future perspectives from artificial neural networks," *Handbook of Materials Modeling: Applications: Current and Emerging Materials*, pp. 1–22, 2018.

[267] Y. C. Yabansu, P. Steinmetz, J. Hötzer, S. R. Kalidindi, and B. Nestler, "Extraction of reduced-order process-structure linkages from phase-field simulations," *Acta Materialia*, vol. 124, pp. 182–194, 2017.

[268] G. Weatherly, "Loss of coherency of growing particles by the prismatic punching of dislocation loops," *The Philosophical Magazine: A Journal of Theoretical Experimental and Applied Physics*, vol. 17, no. 148, pp. 791–799, 1968.